



Pistone, M., Blundy, J. D., Brooker, R. A. (2016). Textural and chemical consequences of interaction between hydrous mafic and felsic magmas: an experimental study. *Contributions to Mineralogy and Petrology*, 171(1), [8]. <https://doi.org/10.1007/s00410-015-1218-4>

Peer reviewed version

Link to published version (if available):  
[10.1007/s00410-015-1218-4](https://doi.org/10.1007/s00410-015-1218-4)

[Link to publication record in Explore Bristol Research](#)  
PDF-document

This is the author accepted manuscript (AAM). The final published version (version of record) is available online via Springer at <http://link.springer.com/article/10.1007%2Fs00410-015-1218-4>

## University of Bristol - Explore Bristol Research

### General rights

This document is made available in accordance with publisher policies. Please cite only the published version using the reference above. Full terms of use are available:  
<http://www.bristol.ac.uk/red/research-policy/pure/user-guides/ebr-terms/>

1                   **TEXTURAL AND CHEMICAL CONSEQUENCES OF**  
2                   **INTERACTION BETWEEN HYDROUS MAFIC AND FELSIC**  
3                   **MAGMAS: AN EXPERIMENTAL STUDY**

4                   Mattia Pistone <sup>1,2</sup>, Jonathan D. Blundy <sup>1</sup>, Richard A. Brooker <sup>1</sup>, EIMF <sup>3</sup>

5                   1) *School of Earth Sciences, University of Bristol, Wills Memorial Building, Queen's Road, BS8 1RJ,*  
6                   *Bristol, United Kingdom.*

7                   2) *Department of Mineral Sciences, National Museum of Natural History, Smithsonian Institution,*  
8                   *10<sup>th</sup> Street & Constitution Avenue NW, Washington, DC 20560-0119, United States.*

9                   3) *Edinburgh Ion Microprobe Facility, School of Geosciences, University of Edinburgh, Grant*  
10                  *Institute, Kings Buildings, West Mains Road, EH9 3JW, Edinburgh, United Kingdom.*

11  
12                  **Abstract**

13                  Mantle-derived, hydrous mafic magmas are often invoked as a mechanism to  
14                  transfer heat, mass and volatiles to felsic plutons in Earth's crust. Field observations  
15                  suggest that mafic, water-rich magmas often intrude viscous felsic crystal-rich  
16                  mushes. This scenario can advect water from the crystallising mafic magma to the  
17                  felsic magma, leading to an increase of melt fraction in the felsic mush, and  
18                  subsequent mobilisation, at the same time as the mafic magma becomes quenched  
19                  through a combination of cooling and water loss. To investigate such a scenario we  
20                  conducted experiments on a water-undersaturated (4 wt.% H<sub>2</sub>O in the interstitial melt)  
21                  dacitic crystal mush (50-80 vol.% quartz crystals) subject to volatile supply from a  
22                  water-saturated ( $\geq 6$  wt.% H<sub>2</sub>O) andesite magma at 950 °C and 4 kbar (12 km depth).  
23                  Our experimental run products show unidirectional solidification textures (i.e. comb  
24                  layering) as crystals nucleate at the mafic-felsic interface and grow into the mafic end-  
25                  member. This process is driven by isothermal and isobaric undercooling resulting  
26                  from a change in liquidus temperature as water migrates from the mafic to the felsic

27 magma. We refer to this process as “chemical quenching” and suggest that some  
28 textures associated with natural mafic-felsic interactions are not simply cooling-driven  
29 in origin, but can be caused by exsolution of volatiles adjacent to an interface,  
30 whether a water-undersaturated felsic magma (as in our experiments) or a fracture.

31

## 32 **1. Introduction**

33 Mantle-derived, hydrous mafic magmas provide heat, mass and volatiles to  
34 felsic magma reservoirs in Earth’s crust. Inputs of mafic magma can lead to a wide  
35 range of physical and chemical interactions. Mafic dykes, sheets and inclusion  
36 swarms are commonly associated with granitoids worldwide (e.g. [Blundy and Sparks](#)  
37 [1992](#); [John and Blundy 1993](#); [Sisson et al. 1996](#); [Czuppon et al. 2012](#)). Mafic magmas  
38 have been frequently invoked as a means of contributing to crustal pluton construction  
39 (e.g. [John and Blundy 1993](#); [de Saint Blanquat et al. 2006](#); [Leuthold et al. 2012](#)),  
40 sustaining shallow magmatic bodies (e.g. [Murphy et al. 2000](#); [Ruprecht and](#)  
41 [Bachmann 2010](#); [Ruprecht et al. 2012](#)) and favouring the generation of ore deposits  
42 (e.g. [Hattori and Keith 2001](#); [Sinclair 2007](#); [Blundy et al. 2015](#)). Primary, subduction-  
43 related mafic magmas are generally crystal-poor and hydrous (H<sub>2</sub>O contents of 1-7  
44 wt.%, with 4 wt.% on average; [Sisson and Layne 1993](#); [Ulmer 2001](#); [Plank et al.](#)  
45 [2013](#); CO<sub>2</sub> contents of > 250 ppm; [Cervantes and Wallace 2003](#)), and intrude more  
46 felsic magmas resident in shallower crustal reservoirs. These felsic magmas are  
47 generally crystal-rich mushes and rheologically locked-up (solid fraction  $\geq 0.5$ ,  
48 [Bachmann and Bergantz 2004](#)), which hampers convection.

49 Broadly two main types of mafic-felsic magma interactions have been  
50 described: magma mingling, and magma mixing. Magma mingling is the physical  
51 interaction between two magmas that are unable to mix thoroughly as a result of high

viscosity ([Sparks and Marshall 1986](#); [Frost and Mahood 1987](#); [Sato and Sato 2009](#)) and density contrast ([Blake and Fink 1987](#); [Koyaguchi and Blake 1989](#); [Grasset and Albarède 1994](#)) or low degree of mechanical stirring ([D’Lemos 1987](#)). Magma mixing is the chemical interaction between two magmas that forms a new “daughter magma” with composition intermediate between the original interacting compositions. Vigorous convective stirring (e.g. [Oldenburg et al. 1989](#)) by chaotic advection (e.g. [Perugini and Poli 2004](#); [Morgavi et al. 2012](#)) and chemical diffusion (e.g. [Watson 1982](#); [Leshner 1994](#)) can lead to the complete blending (or hybridisation) of the two original compositions leaving nearly no vestige of the magmatic “protoliths” (e.g. [Humphreys et al. 2010](#)).

Magma mixing involves diffusion of heat and melt components, including volatiles, between the mafic and felsic end-member magmas. Diffusion is a relatively slow process in nature, which cannot lead to large-scale redistribution of chemical components in the absence of convection ([Bindeman and Davis 1999](#)). Diffusion in natural silicate melts is a relatively slow process for many of the melt components (except for H<sub>2</sub>O and alkalis; [Ni and Zhang 2008](#); [Morgan et al. 2008](#); [Acosta-Vigil et al. 2012](#)), and cannot lead to their large-scale redistribution in the absence of convection. Thermal diffusivities are of the order of 10<sup>-7</sup> m<sup>2</sup>/s in H<sub>2</sub>O-bearing rhyolitic melts at high temperature (> 800 °C; [Romine et al. 2012](#)). This is orders of magnitude larger than chemical diffusivities in silicate melts ([Hofmann 1980](#); [Watson 1981](#); [Sparks and Marshall 1986](#)). Volatile diffusion is about 3 orders of magnitude slower than heat diffusion: in hydrous rhyolite melt at 950 °C and 4 kbar (experimental conditions of this study) the diffusivity of H<sub>2</sub>O (the most abundant volatile) is about 10<sup>-10</sup> m<sup>2</sup>/s ([Ni and Zhang 2008](#)). At these temperature and pressure conditions, the diffusivities of major elements are 1-3 orders of magnitude lower than H<sub>2</sub>O

77 diffusivity, with the diffusivities of network-forming species ( $\text{SiO}_2$  and  $\text{Al}_2\text{O}_3 \approx 10^{-12}$   
78  $\text{m}^2/\text{s}$ ) less than those of network-modifying species ( $\text{CaO} \approx 10^{-12} \text{m}^2/\text{s}$ ;  $\text{MgO}$  and  $\text{K}_2\text{O}$   
79  $\approx 10^{-11} \text{m}^2/\text{s}$ ;  $\text{Na}_2\text{O} \approx 10^{-10} \text{m}^2/\text{s}$ ) (van der Laan and Wyllie 1993).

80 Experimental studies designed to better understand the chemistry of magma  
81 mixing have tended to focus on the interaction between two liquids of contrasted  
82 composition either under anhydrous (Watson 1982; Watson and Jurewicz 1984;  
83 Bindeman and Perchuk 1993) or hydrous conditions (Yoder 1973; Johnston and  
84 Wyllie 1988; van der Laan and Wyllie 1993). In the latter case both end-member  
85 compositions contained identical initial  $\text{H}_2\text{O}$  contents. In a few cases, magma mixing  
86 was investigated through dynamic experiments where two or more samples are forced  
87 to mix under an applied torque (i.e. mixing and mingling). In these tests the  
88 interacting samples display efficient mixing at super-liquidus conditions (Kouchi and  
89 Sunagawa 1982; 1985; Morgavi et al. 2012) or, conversely, very poor mixing when  
90 one of the two samples is crystal-bearing and, thus, the viscosity contrast between the  
91 two systems is large (Laumonier et al. 2014). To date, there are only a few high-  
92 temperature and -pressure melting experiments designed to simulate interaction  
93 between mafic and felsic magmas, as opposed to liquids. None of these studies has  
94 investigated interaction in a realistic scenario where the two samples have different  
95  $\text{H}_2\text{O}$  content and crystallinity prior to interaction, and interact at temperatures  
96 consistent with thermal convergence between a hot mafic  $\text{H}_2\text{O}$ -rich magma and a  
97 relatively cool hydrous felsic magma. This interaction scenario is the focus of the  
98 present experimental study.

99 Our principal motivation is to interpret features of felsic-mafic magma  
100 interaction observed in the field. A well-known example is the Tertiary Adamello  
101 Massif (Alps, Italy), where dominantly tonalite and subordinate granodiorite plutons

are associated with small mafic/ultramafic intrusions, syn-plutonic mafic dykes and sills, and ubiquitous mafic inclusions (Blundy 1989; Blundy and Sparks 1992; John and Blundy 1993). The mafic bodies are texturally and compositionally heterogeneous as a result of variable assimilation of tonalite leading to xenocrystic textures. For example, reactions of quartz phenocrysts from the tonalite with fine-grained dark hornblende-bearing mafic magma produce coronas of green hornblende (Figure 1A). It has also been observed that several mafic and ultramafic rocks can display comb layering at the margins with juxtaposed silicic rocks (e.g. crescumulates layers in Cornone di Blumone, Adamello Massif, Alps, Italy; Ulmer 1986; mafic and ultramafic zonations in Cortland, Duke Island, Ardara and Lac des Iles complexes; Sha 1995). In such a case, elongate grains of hornblende and feldspars are found perpendicular to the interface between felsic and mafic rocks and/or in proximity of fractures in the mingled rock structures (Figure 1B, C). The comb layers are typically asymmetric, and hence display a variety of unidirectional solidification textures (USTs). The presence of hornblende in the gabbroic rock suggests significant H<sub>2</sub>O in the original mafic melt (at least 4 wt.% H<sub>2</sub>O; e.g. Yoder and Tilley 1962; Holloway and Burnham 1972). Field relationships suggest that the tonalitic crystal mush experienced rheological remobilisation during mafic magma intrusions. Based on such field relationships (Figure 1A), Blundy and Sparks (1992) hypothesise the following scenario: (i) a felsic pluton formed in the crust (< 10 km depth) comprises a crystal mush close to its rheological lock-up point ( $\geq 0.5$  solid fraction) and at or close to H<sub>2</sub>O-saturation for the interstitial melt; (ii) this pluton is intruded by a H<sub>2</sub>O-rich mafic magma coming from greater depth (< 20 km); (iii) during the subsequent thermal and chemical interaction the two magmas act as a closed-system (i.e. no net loss of volatiles). Interaction might be expected to produce: i) advection of H<sub>2</sub>O from

the crystallising mafic magma to the felsic mush; ii) melting and remobilisation of the felsic mush; iii) thermal quenching of the mafic magma. We simulated this interaction scenario experimentally with an H<sub>2</sub>O-undersaturated (4 wt.% H<sub>2</sub>O in the interstitial melt) dacitic crystal mush (50-80 vol.% quartz crystals) subject to a volatile supply from a nearly H<sub>2</sub>O-saturated ( $\geq 6$  wt.% H<sub>2</sub>O) andesite magma at 4 kbar and 950 °C. In this contribution we will show that mafic-felsic interactions of the type shown in Figure 1A can also lead to comb layering textures such as that in Figure 1B, C.

## **Experimental and analytical methods**

### ***Experimental strategy***

#### ***Preparation and synthesis of the starting materials***

Preparation of the starting materials was carried out following the approach of Pistone et al. (2012) and Pistone (2012). The two silicate compositions (F = felsic; M = mafic) are synthetic equivalents of natural Adamello bulk compositions JM101 (dacite/tonalite) and JM102 (andesite/diorite) reported by Blundy and Sparks (1992), who used a natural powder of the latter for a series of H<sub>2</sub>O-saturated, 1 kbar experiments. However, with respect to the original recipe of JM102 composition, M composition has been modified to generate a more felsic system approaching the composition of F (= JM101). Such a compositional modification of M, which violates the original definition of “mafic composition”, represents an experimental compromise that allows constraining the influence of H<sub>2</sub>O only and, simultaneously, attenuating the diffusion of other slower melt components driven by limited chemical gradients, which otherwise could have “overwritten” the H<sub>2</sub>O signature during interaction experiments. In addition, sample M is crystal-free to maximise H<sub>2</sub>O content in the melt during synthesis; however, this differs from the original natural

scenario depicted in Figure 1A where the mafic magma is expected to carry some phenocrysts during the interaction with felsic crystal mushes. Oxides ( $\text{SiO}_2$ ,  $\text{Al}_2\text{O}_3$ ,  $\text{Na}_2\text{SiO}_3$ ) and hydroxides ( $\text{Al}(\text{OH})_3$ ,  $\text{K}_2\text{Si}_3\text{O}_7 \cdot 3\text{H}_2\text{O}$ ) were used for material preparation; hydroxides provide different amounts of structurally-bound  $\text{H}_2\text{O}$  to F (4 wt.%  $\text{H}_2\text{O}$ ) and M (6 wt.%  $\text{H}_2\text{O}$ ). The mafic (M) end-member was crystal-free. Crystal-free felsic starting material is designated F0. Aliquots of F were mixed with quartz particles to create additional starting materials of different crystallinity: F50 = 50 vol.% crystals; F60 = 60 vol.%; F70 = 70 vol.%; F80 = 80 vol.%. Quartz crystals (DORSILIT 2500:  $\text{SiO}_2$  = 98.90 wt.%;  $\text{Al}_2\text{O}_3$  = 0.41 wt.%;  $\text{Fe}_2\text{O}_3$  = 0.02 wt.%;  $\text{TiO}_2$  = 0.04 wt.%; Alberto Luisoni AG, Switzerland) were chosen as suspended particles (rough particles with aspect ratios between 1.0 and 3.5) for the preparation of the crystal mushes due to their advantageous properties at the temperature and pressure conditions of our experiments: they do not dissolve appreciably in the felsic melt (JM101 is already at quartz saturation), and inhibit further crystallisation of the residual melt (Pistone et al. 2012). The small amounts of Ti-Fe oxide impurities on the surface of the quartz grains facilitate wetting by the silicate melt during high-temperature and -pressure synthesis (Rutter et al. 2006). Crystals were fired for five hours in a one-atmosphere muffle furnace at 1000 °C to dry the surfaces and to remove any fluid inclusions. Their size was selected by sieving and checked by Malvern Laser Diffraction Grain Sizer at the Limno-Geology Laboratory of ETH-Zurich. The 3D grain size distribution shows a mean value of 68  $\mu\text{m}$  with a sorting of 2.43 and a positive skewness of 0.37 (Pistone et al. 2012). To mix the powders with the appropriate amount of quartz particles, densities of the employed glasses were estimated from the equation of Lange and Carmichael (1987) at room conditions (298 K and 1 bar).



177       Following the approach of Pistone et al. (2012) and Pistone (2012), the  
178 starting material powders were cold-pressed into cylindrical stainless steel canisters  
179 (110 mm long, 35 mm inner diameter, 3 mm wall thickness) lined with a thin (25  $\mu\text{m}$ )  
180 Mo foil to avoid chemical contamination. Filled canisters were stored at 100 °C to  
181 remove any adsorbed humidity and arc-welded shut. Tightness of the seal was  
182 checked under vacuum in a water bath and by weighing. The canisters were hot  
183 isostatically pressed (HIP) for 24 hours in a large capacity (170 mm in diameter; 500  
184 mm high), industrial, internally-heated pressure vessel (Sinter-HIP-Kompaktanlage;  
185 ABRA Fluid AG, Switzerland) at 1.8 kbar and 1200 °C at the Rock Deformation  
186 Laboratory of ETH-Zurich. The temperature was nearly constant over the entire  
187 volume of the vessel (maximum difference of 18 °C along the length of a sample). A  
188 two-step cooling was applied: a rapid decrease of temperature (60 °C/minute) down to  
189 the inferred glass transition temperature (when the viscosity is considered equivalent  
190 to  $10^{12}$  Pa·s) followed by slow cooling (0.6 °C/minute) to room temperature. The first  
191 cooling segment was designed to avoid crystallisation; the second segment produces  
192 thermally relaxed glasses (Webb and Dingwell 1990). During cooling the confining  
193 pressure decreased slightly with decreasing temperature (38 bar/minute in the first  
194 cooling stage; 1 bar/minute in the second one). A total of 6 hydrous samples were  
195 produced: M, F0, F50, F60, F70, F80. The weight of the canisters after the HIP run  
196 was compared with the initial weights and revealed no significant differences (less  
197 than 1 g over 200 g in total) suggesting that no H<sub>2</sub>O was lost during synthesis.

198

## 199 *Experiments*

200       Cylinders of 3 mm diameter and variable length (Table 1) were cored from the  
201 synthesised glasses and polished on the top and bottom surfaces to ensure a perfect

202 initial contact between the interacting samples. The sandwiched samples were inserted  
203 into Au capsules (3-4 mm diameter), which, in turn, were inserted in larger Mo-lined  
204 Au capsules (6 mm diameter) filled with  $\text{Al}_2\text{O}_3$  powder and deionised  $\text{H}_2\text{O}$  (0.1-0.2  
205 ml). Experiments were conducted under oxidised conditions ( $f\text{O}_2 = \text{NNO}+1$  to  $+2$ ; see  
206 below). In contrast, the starting materials were synthesised at reduced conditions  
207 ( $\log f\text{O}_2 = -13.08$  at  $950^\circ\text{C}$  for  $\text{MoMoO}_2$  buffer, which is close to IW buffer; [O'Neil](#)  
208 [1986](#)). The presence of Mo in the double capsule setup slowed down the oxidation of  
209 the starting materials by loss of  $\text{H}_2$  on the experimental timescale.

210 Experiments were carried out at the University of Bristol in an end-loaded  
211 [Boyd and England \(1960\)](#) type piston cylinder apparatus. Run conditions are given in  
212 Table 1. The chosen experimental temperature ( $950^\circ\text{C}$ ) approximates a mafic magma  
213 emplaced at  $1100^\circ\text{C}$  against a felsic host at  $800^\circ\text{C}$  ([Blundy and Sparks 1992](#)). Since  
214 no latent heat of crystallisation or heat transfer can be experimentally reproduced,  
215 experiments simulated that mafic-felsic magma interaction after the interacting  
216 systems experienced heat transfer and achieved thermal equilibration. Experiments  
217 were carried out in a 19 mm talc-pyrex cell (manufactured by Ceramic Substrates and  
218 Components, Isle of Wight, UK), based upon the original design of [Kushiro \(1976\)](#).  
219 This type of cell uses a tapered furnace (with  $3^\circ$  taper), which minimises the thermal  
220 gradient to  $< 10^\circ\text{C}$  at  $1000^\circ\text{C}$  over the central 10 mm of the cell ([McDade et al.](#)  
221 [2002](#)). Based on the CsCl melting reactions the friction correction was  $3.6 \pm 1.0\%$  at  
222 10 kbar and  $1000^\circ\text{C}$  ([McDade et al. 2002](#)) and  $20 \pm 1.0\%$  at 5 kbar and  $950^\circ\text{C}$ . Also,  
223 based on the  $\text{H}_2\text{O}$  solubility conditions of the  $\text{H}_2\text{O}$ -saturated sample M, the effective  
224 applied confining pressure to the run products was circa 4 kbar. Temperature was  
225 monitored by a D-type ( $\text{W}_{97}\text{Re}_3/\text{W}_{75}\text{Re}_{25}$ ) thermocouple connected to a Eurotherm  
226 800 series controller, with no correction for the pressure effect on the electromotive

force (Mao and Bell 1971). The hot piston-out technique (Johannes et al. 1971) was used in all experiments. Experiments ran for 24 hours (except for one that lasted for one week; Table 1) and were terminated by turning off the power. Recovered charges were impregnated in epoxy and polished.

Two different interaction setups were used in the experiments: i) classic two-layer Setup A with felsic overlying mafic, and ii) “intrusion-type” Setup B with mafic sandwiched between two felsic samples. The two approaches allowed us to simulate the mafic-felsic magma interaction at different mass ratios (mafic-felsic ratio of 1:1 in Setup A, and 1:2 in Setup B; Table 1), and potentially retrieve information on the volatile depletion of the mafic sample during the interaction with one or two felsic samples respectively. To better constrain the textures and chemistry generated during the interaction experiments we also performed simple equilibrium runs on felsic and mafic starting materials. Additionally, after 30 minute dwell time at 1000 °C, four isobaric (4 kbar) cooling experiments from 1000 to 950 °C, with two different cooling rates (slow cooling = 1 °C/minute, and fast cooling = 3.3 °C/second; Table 1), were conducted on crystal-free mafic samples to provide a textural comparison with the microstructures generated in the interaction experiments. A single 48-hour experiment (Table 1) was conducted in cold-seal, externally-heated vessel (with an intrinsic  $fO_2$  close to NNO+1; Rouse 2000) to simulate volatile exsolution from the mafic end-member during slow isothermal decompression at low pressure (from 2 to 1 kbar at 0.35 bar/minute) and relatively low temperature (870 °C). This test provided a comparison between conditions of volatile-saturation (cold-seal) and volatile-undersaturation (piston cylinder).

## *Analytical techniques*

## *Electron microprobe and scanning electron microscopy*

Glasses and minerals from the starting materials and experimental charges were analysed with a CAMECA SX-100 wavelength-dispersive electron probe micro-analyser (EPMA). Glasses were analysed with a 15 kV acceleration voltage, 2-5 nA beam current and 10-20  $\mu\text{m}$  diameter (defocused) beam. Minerals were analysed with a focused (1  $\mu\text{m}$ ) 10 nA beam current and an accelerating voltage of 20 kV. Natural and synthetic standards were used for calibration. Table 2 shows compositions of starting glass and minerals in representative experimental charges. Chemical profiles in the glass composition across the run products based on EPMA data are reported in Table 3.  $\text{H}_2\text{O}$  concentrations were estimated by the volatile-by-difference method (Devine et al. 1995; Humphreys et al. 2006) and by SIMS (see below).

Using the approach of Saunders et al. (2014) to analysing crystal zoning, lines of quantitative spot analyses to produce quantitative element profiles through quartz crystals and surrounding glass were conducted using a JEOL 8530F field emission gun electron probe micro-analyser (FEG-EPMA). Analyses were carried out with a 10 kV acceleration voltage, 1 nA beam current and 1  $\mu\text{m}$  beam diameter. These analytical conditions allowed us to explore potential quartz dissolution in the silicate melt at run conditions. Primary calibrations for FEG-EPMA used the same mixture of synthetic and natural standards as were used with the conventional EPMA. Supplementary material displays chemical data from the lines of quantitative spot analyses in quartz crystals and surrounding silicate glass.

Backscattered (BSE) images of the experimental charges were acquired on a Hitachi S-3500N scanning electron microscope (SEM) with 15 to 25 kV accelerating voltage and 1 nA beam current. Images were used to estimate volume fraction and size of the different phases using the Java-based software JMicro-Vision v1.2.7.

Characteristic X-ray distribution maps for Si-, Ca- and Fe-K $\alpha$ , acquired using EPMA and SEM, were used to evaluate the chemical diffusion in the interaction experiments.

### ***Secondary ion mass spectrometry***

Glassed starting materials and experimental charges were analysed by secondary ion mass spectrometry (SIMS) for dissolved H<sub>2</sub>O and a number of trace elements, using a CAMECA ims-4f ion microprobe at the University of Edinburgh. Au-coated samples were analysed with a 1.5 nA, 10.8 kV <sup>16</sup>O<sup>-</sup> beam focussed to a 10  $\mu$ m spot, with 15 keV net impact energy (i.e. 10.7 keV primary + 4.5 keV). Positive secondary ions were extracted at 4.5 keV with a 75 eV offset and a 40 eV energy window, to minimise molecular ion transmission. Prior to each analysis, a 7  $\mu$ m<sup>2</sup> raster was applied for 2 minutes at the target glass areas in the sample to remove any surface contamination around the edge of the sputter pit. NIST-610 (Hinton 1999), hydrous silica-rich (SiO<sub>2</sub> > 52 wt.%) SISS-48, SISS-51, SISS-59, SISS-60 (H<sub>2</sub>O content ranging from 2.48 to 4.91 wt.%; Sisson and Grove 1993), a natural obsidian glass from Lipari (0.72 wt.% H<sub>2</sub>O; Humphreys et al. 2006), RB-480 (0.33 wt.% H<sub>2</sub>O; Field et al. 2012), RB-497 (0.31 wt.% H<sub>2</sub>O; Richard Brooker, unpublished data), SB21, SB23 (10.5 to 10.9 wt.% H<sub>2</sub>O; Jenny Riker, unpublished data), and hydrous haplogranitic HGG0, HGG3, HGG4, HGG5 glasses (0 to 5.25 wt.% H<sub>2</sub>O; Ardia et al. 2008) were used as standards to monitor the H/Si ion yield and background consistency at the start of each day. Ten cycles were counted, corresponding to a counting time of about 10 minutes. In addition to <sup>1</sup>H and <sup>30</sup>Si, <sup>7</sup>Li, <sup>11</sup>B, <sup>26</sup>Mg, <sup>42</sup>Ca, <sup>47</sup>Ti and <sup>54</sup>Fe were measured. The heavier elements were measured to assess the consistency of the major element composition. The background H<sub>2</sub>O correction (as

302 measured on NIST-610) was equivalent to  $\leq 0.2$  wt.% H<sub>2</sub>O. To remove the effects of  
303 small variations in beam current, data are presented Si-normalised and corrected using  
304 the NIST-610 standard of the GeoReM database ([http://georem.mpch-](http://georem.mpch-mainz.gwdg.de/)  
305 [mainz.gwdg.de/](http://georem.mpch-mainz.gwdg.de/)). The analytical results are characterised by a low standard deviation  
306 (Li = 1.01 %, B = 0.45 %, Mg = 0.93 %, Ca = 1.30 %, Ti = 1.20 %, Fe = 2.25 %). C  
307 species was not measured; however, Raman spectra and CO<sub>2</sub>-intensity maps of the  
308 glasses of the run products (not presented here) did not reveal any presence of CO<sub>2</sub>.  
309 Table 4 reports the SIMS data.

310

## 311 **Results**

312 Run products are labelled with the abbreviations of the two or three separate  
313 components added (e.g. M-F0 is a couple made of andesite and crystal-free dacite; F0-  
314 M-F0 is a sandwich of andesite between two layers of crystal-free dacite, etc.). We  
315 present the microstructural and chemical results of the interaction experiments in three  
316 groups, each showing a specific sample-sample interaction:

- 317 1) andesite and crystal-free dacite (M-F0 = liquid-liquid interaction in absence of a  
318 pre-existing crystallinity in either sample)
- 319 2) andesite and crystal-bearing dacite (M-F50 to F80 = liquid-mush interaction)
- 320 3) chemically identical samples (M-M and F0-F50) for evaluating crystallisation  
321 kinetics in the absence of any difference in melt composition or H<sub>2</sub>O content.

322 Microstructural and chemical results from additional tests simulating the  
323 isobaric cooling of a crystal-free andesite, and the interaction between a crystal-free  
324 andesite and a crystal-bearing dacite during isothermal decompression (M-F50) are  
325 also provided. The microstructural and chemical results of the phase equilibrium runs  
326 involving single samples (i.e. no interaction) show limited crystallisation in the

crystal-free felsic sample (< 40 vol.% in F0; Table 1), and no crystallisation in the felsic crystal-bearing samples (see F80 in Table 1). The andesitic samples in the phase equilibrium experiments crystallise with the same phase volumetric proportions observed in the run product M-M (< 50 vol.%; Table 1).

### ***Microstructures***

Crystallisation of the crystal-free samples (F0 and M) observed in the phase equilibrium experiments (i.e. in absence of other interacting samples) is driven by a combination of H<sub>2</sub>O-undersaturation conditions (i.e. materials were originally synthesised at 2 kbar, corresponding to H<sub>2</sub>O-saturation conditions), which render the samples more undercooled, and absence of initial crystal phases (such as quartz in the crystal-bearing materials), which prevents from additional crystallisation during experiments. Thus, the textures of the crystal-free samples observed in the interaction experiments (e.g. M-F0 or M-FX, with FX as crystal mush, which does not crystallise and, thus, remains quartz-saturated at 4 kbar) are the result of two processes: phase equilibrium crystallisation, and H<sub>2</sub>O migration from high to low concentration (see below).

### ***Interaction between initially crystal-free andesite and crystal-free dacite***

Two runs were conducted to simulate interaction between initially crystal-free andesite (M) and dacite glasses (F0): F0-M and F0-M-F0 (Figure 2A-B). The main difference between the two runs is the experimental duration (24 hours versus 1 week). The longer run (F0-M-F0) generated more extensive crystallisation in both end-members, particularly in the M domain (Table 1). In both run products hornblende and plagioclase form a diktytaxitic texture (with less vesicular

groundmass than what observed in natural mafic enclaves) in M (Figures 2A-B). Hornblende crystals in F0 domain in F0-M-F0 are arranged in two ways: perpendicular to the interfaces with M, and, beyond a distance of ~0.5 mm from the interface, with a diktytaxitic arrangement (Figure 2A-B). Along the interaction interfaces of both samples crystal size reduction of hornblende in F0 (from about 200 µm length at ~0.5 mm from the interface to 2 µm at the interface) and plagioclase and hornblende in M (from 40 µm at ~0.5 mm from the interface to 1 µm at the interface) are observed (Figures 2A-B and 4A). Fe-Ti oxides (1-5 µm) are ubiquitous in all domains with a mean number density of about 40 crystals per 0.01 mm<sup>2</sup>. The largest number density is found at the interface between the two samples (Figures 2A-B and 4A). Vesicles are mainly located along the interfaces in F0-M and F0-M-F0; larger vesicles (up to 40 µm diameter) are found in F0 (Figures 2A-B).

#### ***Interaction between initially crystal-free andesite and dacitic crystal mush***

Four runs were conducted to simulate the interaction of andesite (M) and dacitic crystal mush: F50-M, F60-M-F60, F70-M, and F80-M-F80 (Figure 2C-F). All run products are characterised by the following microstructural features:

- i) Extensive crystallisation of M, which becomes more evident when Setup B is used (Table 1)
- ii) Disseminated magnetite in M, whose number density increases towards the interaction interface (Figures 2C-F, 5)
- iii) A marked decrease in plagioclase and hornblende crystals size towards the interface (from plagioclase length of 250 µm and hornblende length of 190 µm at ~0.5 mm from the interface to 2 µm plagioclase and hornblende size at the interface; Figures 2C-F, 5)



377 iv) Arrangement of plagioclase and hornblende crystals perpendicular (Figure 2C,  
 378 E), or at high angle (circa 50-60°; Figure 2D, F), to the interface with F, up to  
 379 distances of ~0.4 mm from the interaction interface  
 380 v) Perpendicular arrangement of hornblende and plagioclase crystals in M and  
 381 decrease of their size (up to a mean size of 2  $\mu\text{m}$ ) to the inner walls of the gold  
 382 capsule when Setup A is used (Figure 2C-F)  
 383 vi) Increase of the local crystal fraction in M domain by about 70% to circa 95%  
 384 (Figure 2C-F) from ~0.5 mm from the interface towards the interface  
 385 vii) Crystal-free, glass layer (30 to 60  $\mu\text{m}$  thick) in F along the interface with M  
 386 (Figure 2C-F)  
 387 viii) Hornblende-rich layer located close to quartz crystal clusters (Figure 2C-F), and  
 388 hornblende and/or magnetite crystallisation in glassy interstices between quartz  
 389 crystals in F  
 390 ix) Reaction rims on quartz crystals displaying smooth boundaries and crowns of tiny  
 391 (1 to 3  $\mu\text{m}$ ) hornblende microlites (Figure 2C-F)  
 392 x) Presence of vesicles in M and along the interface in F, particularly in the glass  
 393 and/or hornblende-rich layer (Figure 2C-F).  
 394 The crystal size reduction of plagioclase and hornblende towards the interface  
 395 observed in both samples is also evidenced by X-ray maps of Si- and Ca-K $\alpha$  (Figure  
 396 4B). X-ray map of Fe-K $\alpha$  evidences the large presence of Fe-Ti oxides in the andesite  
 397 sample, with high number densities in proximity to the interface (Figure 4B). The  
 398 reported textural features of the andesitic sample during interaction experiments are  
 399 dramatically different from those observed in the phase equilibrium experiments.  
 400 Specifically, phase equilibrium textures of M lack in: 1) more extensive crystallisation  
 401 (> 50 vol.%; Table 1), with an increase in crystallinity (from 50 to 95 vol.%) towards

the interaction interface against the felsic, and 2) perpendicular arrangement of minerals, with size reduction towards the interaction interface against the felsic sample.

#### ***Interaction between chemically identical samples***

The interaction of samples with identical chemical composition and H<sub>2</sub>O content was tested with runs F50-F0 and M-M (Figure 2G-H). Run product F50-F0 shows extensive hornblende crystallisation in F0 (Table 1), with crystals arranged perpendicular or at high angle (45° to 60°) to the interface (Figure 2G). Hornblendes decrease in size (down to 2 µm) towards the interface (Figure 2G). In F50 quartz microlites (up to 10 µm long) lie perpendicular to the interface, without any observable size reduction (Figure 3A). Hornblende and quartz microlites of 2-3 µm size are also found in isolated glass pockets within quartz crystal clusters (Figure 2G).

Run product M-M displays disseminated Fe-Ti oxides and vesicles in both sample domains (Figure 2H). The interface between the two samples is vague, but can be discerned by the presence of hornblende crystals in the lower domain. Large plagioclases (up to 100 x 10 µm wide) are found in the core of the two domains (at a distance of  $\geq 0.5$  mm from the interface). Plagioclases form a loose diktytaxitic texture and their size tends to decrease towards the interface (Figure 2H). Hornblende crystals in the lower domain also decrease in size towards the interface (Figure 2H).

#### ***Isobaric cooling of initially crystal-free andesite***

Four runs at two different cooling rates (Table 1) were conducted in order to compare textures generated solely by cooling versus those generated by interaction (Figure 3). The fast-cooled (3.3 °C/s) run products show reduction in the size of

hornblende, but not plagioclase, towards the sample periphery (Figure 3A-B). Fe-Ti oxides are absent. The slow-cooled (1 °C/min) run products show extensive crystallisation (glass fraction < 0.06; Table 1), with no clear arrangement of plagioclase and hornblende (Figure 3C-D). Plagioclases are acicular, with constant size (10-15 µm length); hornblende crystals (2-30 µm length) are dendritic. Fe-Ti oxides are diffusely distributed. Similar crystal textures were generated in 1 kbar undercooling experiments on JM102 by [Blundy and Sparks \(1992\)](#); their Fig. 9b).

### ***Interaction during isothermal decompression***

One slow-decompression run at low pressure was conducted to simulate the interaction of initially crystal-free andesite and dacitic crystal mush (F50-M [CSV], where CSV means cold seal vessel; see Supplementary Material). Abundant vesicles are observed in both sample domains (Table 1). Vesicles (average diameter 15 µm) in M are concentrated in the core of the sample; larger vesicles (up to 100 µm) are found throughout F50. Overall, there are more vesicles in M than F50, which suggest that gas released from M during crystallisation rose into F50. Gaps between F50 and the capsule walls suggest the production of excess gas during the experiment. In M plagioclase and hornblende crystals lie perpendicular to the interface and, in the lower portion, to the capsule wall. Plagioclase and hornblende crystals decrease in size towards the periphery of M; in particular, tiny (1-2 µm size) plagioclase and hornblende crystals form a thin rim (3 to 10 µm) around M. The interior texture of M is diktytaxitic. In F50 a few hornblende crystals are found in glass-rich regions characterised by a high number density of vesicles. Fe-Ti oxides are observed throughout, often localised around the periphery of F50 (see Supplementary Material).

## 452 *Chemistry*

### 453 *Interaction between andesite and crystal-free dacite*

454 EPMA and SIMS analyses of run products F0-M and F0-M-F0 provide  
455 chemical profiles of essential molar ratios (Figures 5A-B, showing  $ASI =$   
456  $Al_2O_3/[CaO+Na_2O+K_2O]$ ,  $Al/Si$ ,  $Al/Na$ ,  $Al/K$ ,  $Na/K$ ; [Acosta-Vigil et al. 2012](#)), major  
457 and trace elements (Supplementary Material) and  $H_2O$  across the sample (Figures 6A-  
458 B; Tables 3-4). The molar ratio profiles of  $Al/Si$  and  $ASI$  appear rather constant along  
459 the entire domain of both run products, and close to the original values of the starting  
460 glasses (Figure 5A-B; Table 2). Particularly, the  $Al/Si$  suggests that  $Al_2O_3$  and  $SiO_2$   
461 decrease and increase in the same proportion respectively (Supplementary Material).  
462 Conversely, the other molar ratio distributions appear variable ( $Na/K$ , and  $Al/K$ ) or  
463 decrease from the andesite to the dacite ( $Al/K$ , and  $Al/Na$ ) in run F0-M (Figure 5A).  
464 Neither in the long duration run F0-M-F0 the same molar ratios show a perfectly  
465 constant distribution in both dacite domains (Figure 5B). Overall,  $Al/K$  and  $Na/K$  are  
466 lower than the original molar ratios of the starting materials, and  $Al/Na$  is higher than  
467 the starting  $Al/Na$  in both andesite and dacite. These changes of the latter molar ratios  
468 are suggestive of an increase of  $K_2O$  and  $Al_2O_3$ , and a decrease of  $Na_2O$  in the  
469 residual glass (Supplementary Material) as a consequence of crystallisation of the  
470 initially crystal-free dacite and andesite samples. Further details on the major and  
471 trace element concentrations in the glass phase of each interacting sample are reported  
472 in the Supplementary Material.

473  $H_2O$  contents are similar in the two domains, with limited increase of  $H_2O$  in  
474 the glass from the dacite (4-5 wt.%) to the andesite (6-7 wt.%; Figure 7A), with  $H_2O$   
475 content variations of up to 2 wt.% along the interface (Figure 6A-B). Based on the  
476 glass fractions found in the interacting samples (Table 1), the  $H_2O$  content in the bulk

477 samples in run F0-M tends to increase from the dacite (2.5-3.1 wt.%) to the andesite  
478 (3.3-3.9 wt.%). However, the andesitic sample crystallises largely along the interface  
479 (up to circa 80 vol.%) whereas the dacite crystallisation along the interface reaches  
480 only about 60 vol.% (Figure 4A). There is no evident H<sub>2</sub>O gradient between the two  
481 interacting domains after the 24-hour experiment. Conversely, in the longer run F0-  
482 M-F0, the H<sub>2</sub>O content in the bulk samples clearly changes from the andesite (100  
483 vol.% crystalline; Table 1) to the dacite (~70 vol.% residual glass content in both  
484 dacitic domains; Table 1). Indeed, all the H<sub>2</sub>O is stored in the bulk dacite (2.8-3.5  
485 wt.%), suggesting H<sub>2</sub>O transfer from the andesite to the dacite. The latter is less  
486 crystalline than the equivalent domain in run F0-M (Table 1).

487

#### 488 *Interaction between andesite and dacitic crystal mush*

489 EPMA and SIMS analysis profiles of run products from interaction  
490 experiments generally show a change in chemistry from the dacite to the andesite,  
491 particularly for the major oxides such as SiO<sub>2</sub> and Al<sub>2</sub>O<sub>3</sub>, which show larger  
492 variations in the dacite sample portions where the glass is surrounded by quartz  
493 crystals (Supplementary Material), suggestive of quartz dissolution at run conditions.  
494 Similarly to the crystal-free runs (F0-M and F0-M-F0), runs involving a crystal mush  
495 show constant profiles of Al/Si and ASI along the entire run product, and close to the  
496 original values of the starting glasses, suggestive of the potential limited chemical  
497 change induced by initial crystallisation (as observed in the phase equilibrium  
498 experiments) prior to or at the onset of H<sub>2</sub>O diffusion during interaction experiments.  
499 Similarly to what observed in the crystal-free runs, the distributions of Na/K, Al/Na,  
500 and Al/K appear to decrease from the andesite to the dacite domain in all run products  
501 with crystallinities < 70 vol.% (Figures C-D). At higher crystallinity the molar ratio

Al/K displays an inverse trend, with a slight decrease from andesite to dacite (Figures 5E-F), suggesting an increase of available  $\text{Al}_2\text{O}_3$  (melt component with slow diffusion; e.g. [Acosta-Vigil et al. 2012](#)) in the residual glass during fast  $\text{H}_2\text{O}$  diffusion. Overall, the values of Na/K, Al/Na, and Al/K are lower than those reported in the starting glasses. For the same reasons reported in the interacting crystal-free samples above, the decrease of these molar ratio values are suggestive of an increase of  $\text{K}_2\text{O}$  and  $\text{Al}_2\text{O}_3$ , and a decrease of  $\text{Na}_2\text{O}$  in the residual glass (Supplementary Material) as a consequence of the  $\text{H}_2\text{O}$  diffusion-induced crystallisation of the andesite and  $\text{H}_2\text{O}$  diffusion-induced quartz dissolution in the dacite. Also, the same molar ratios of the run products with Setup B result lower by 20% than those observed in the run products with Setup A, suggestive of the different impact of the mafic-felsic mass ratio on  $\text{Al}_2\text{O}_3$  and alkalis contents in the residual glass in the mafic end-member. Further details on the major and trace element concentrations in the glass phase of each interacting sample are reported in the Supplementary Material.

$\text{H}_2\text{O}$  contents in the glass increase from the dacite (5-6 wt.%  $\text{H}_2\text{O}$ ) to the andesite (7-8 wt.%) (Figure 6C-F). In the dacite  $\text{H}_2\text{O}$  contents are higher in proximity to the interface, and lower in glass pockets within quartz crystal clusters (see SIMS analysis spots in the Supplementary Material). More interestingly,  $\text{H}_2\text{O}$  contents in the bulk samples change dramatically from the andesite to the dacite, particularly along the interface (< 1 mm distance from the interface; Figure 6C-F) where the andesite is largely crystalline (> 90 vol.%), whereas the dacite is glassy or displays limited hornblende crystallisation (< 7 vol.%; Table 1) around the quartz crystals (Figure 4B). Bulk  $\text{H}_2\text{O}$  contents in the two bulk domains varies from < 0.7-0.8 wt.% in the upper portion of the andesite (< 1 mm from the interface) to 1.1-2.9 wt.% in the dacite. The greater the crystal content in the dacitic mush, the higher the  $\text{H}_2\text{O}$  content in the glass

(Figure 6C-E) and the lower the H<sub>2</sub>O content in the bulk dacite. Run F80-M-F80 represents an exception since both H<sub>2</sub>O contents in the glass (3-4 wt.%) and in the bulk dacite (0.36-0.63 wt.%) are lower than in the other run products (Figure 6C-F), suggestive of the combination of large crystal content in the mush and dissolution of quartz during the experiment.

### ***Interaction between chemically identical samples***

As expected, SIMS analysis of run products involving interaction between chemically identical samples show no evident change in major oxides, trace elements and H<sub>2</sub>O contents in the residual glass from one sample domain to the other (Table 4; Supplementary Material). Thus the chemical features described in preceding sections result from interaction, rather than any artefact of the experimental design.

## **Discussion**

### ***The change of the liquidus temperature as a function of H<sub>2</sub>O content***

Microstructural and chemical changes that occur during interaction experiments are most readily interpreted in terms of the changes in liquidus temperature ( $T_L$ ) that arise when magmas of contrasted chemistry are juxtaposed. Because  $T_L$  is strongly reduced by the addition of H<sub>2</sub>O, up to the point of saturation, so the flux of H<sub>2</sub>O from one domain to another has the greatest influence on  $T_L$ . In our experiments the values of local  $T_L$  were computed using the model of [Makhluf et al. \(2014\)](#) using the EPMA data of residual silicic glass (Table 3), including SIMS-based H<sub>2</sub>O content (Table 4), in order to estimate the local H<sub>2</sub>O contents in the bulk rock based on the local glass volume fractions (see Supplementary Material). In our experiments there is an H<sub>2</sub>O gradient between the two interacting samples (andesite

552 melt = 6 wt.% H<sub>2</sub>O versus dacite melt = 4 wt.% H<sub>2</sub>O; Table 2). The initial  $T_L$  results  
553 different in each starting material: the andesite has  $T_L = 816 \pm 1$  °C (Figure 8), and the  
554 dacite displays a decrease of the initial  $T_L$  with increasing crystallinity in the felsic  
555 mush, ranging from  $T_L = 923 \pm 1$  °C at  $3.69 \pm 0.02$  wt.% H<sub>2</sub>O in initial crystal-free  
556 glass to  $1109 \pm 1$  °C at  $0.74 \pm 0.02$  wt.% H<sub>2</sub>O in the most crystal-rich sample (Figures  
557 6, 7). Given the chemical similarity of the interacting compositions (Table 2), the  
558 lower andesite  $T_L$  than the dacite  $T_L$  is due to the initial high H<sub>2</sub>O content in the  
559 andesite (Table 2). The change of  $T_L$  is clearly evident in both interacting domains:  $T_L$   
560 drops in the dacite, to below the experimental temperature at some locations, and  
561 increases markedly in the crystallising andesite (Figure 7). Such changes in  $T_L$   
562 become more pronounced with increasing crystallinity in the felsic mush and with  
563 decreasing the mafic/felsic mass ratio (Figure 7).

564 One of the primary consequences of melt dehydration is isothermal  
565 crystallisation, first recognised by Tuttle and Bowen (1958) and invoked as a cause of  
566 crystallisation in hydrous magma by Blundy and Cashman (2001). This behaviour  
567 arises because, compared to other compositional parameters, H<sub>2</sub>O has a  
568 disproportionate effect on the  $T_L$  of a magma (Yoder et al. 1957; Burnham and Jahns  
569 1962; Merrill and Wyllie 1975). Thus, H<sub>2</sub>O loss from any hydrous magma, whether  
570 by degassing or diffusion, will drive large increase in  $T_L$  leading to effective  
571 undercooling and consequent crystallisation.

572 During interaction of mafic and felsic magmas a number of simultaneous  
573 chemical and physical changes occur. These may drive crystallisation or melting,  
574 depending on the relationship between the interaction temperature and the  $T_L$  of each  
575 domain. We will express the change in  $T_L$  as normalised temperature:  $T_{\text{experimental}} / T_L$ ,  
576 both of which are known from our experiments (Figure 8A). In the case of



577 undercooling, crystallisation will result, but the extent to which nucleation, giving rise  
578 to many small crystals, is favoured over growth, giving rise to large crystals, depends  
579 on the magnitude of the undercooling. In general, larger values of undercooling  
580 favour crystal nucleation, while small values of undercooling favour crystal growth  
581 (Figure 8A). Crystallisation serves to reduce  $T_L$  and hence reduce undercooling,  
582 eventually reaching zero at the point of chemical equilibrium. Where the interaction  
583 temperature is greater than  $T_L$ , melting will result (Figure 8A). We can better  
584 understand this complex interplay of diffusion of heat, diffusion of mass, and  
585 crystallisation kinetics in terms of three end-member scenarios.

586 First, consider juxtaposition of two crystal-free, anhydrous melts of different  
587 composition at two different temperatures. In this example only heat crosses the  
588 interface between the two domains (Figure 8B). The contact temperature at the  
589 interface ( $T_{interface}$ ) will lie between the  $T_L$  of the felsic ( $T_{L(felsic)}$ ) and mafic ( $T_{L(mafic)}$ )  
590 domains. The initial undercooling that occurs in the mafic domain is  $\Delta T = T_{interface} -$   
591  $T_{L(mafic)}$  and will be greatest (i.e. most negative) at the interface. Thus, crystal  
592 nucleation is favoured close to the interface and a so-called “chilled margin” results.  
593 A crystallisation front propagates away from the interface into the mafic domain, with  
594 progressively smaller  $\Delta T$  and consequently larger, but fewer crystals. In the felsic  
595 domain  $\Delta T = T_{interface} - T_{L(felsic)}$  may be positive at the interface. In that case a fully  
596 molten layer may result. Elsewhere in the felsic domain some evidence of partial  
597 melting will be apparent, although temperatures are unlikely to be sufficient to cause  
598 complete melting (Figure 8B).

599 Next, consider the case where two melts at different temperature are brought  
600 into contact but the mafic magma is H<sub>2</sub>O-saturated and the felsic magma is  
601 anhydrous. In this case both heat and H<sub>2</sub>O will pass from the mafic to the felsic

domain, complicating the textural consequences of interaction (Figure 8C). As before, thermal undercooling of the mafic domain at the interface will lead to crystallisation. However the loss of H<sub>2</sub>O from the mafic domain to the felsic domain will drive up  $T_{L(mafic)}$ , further increasing  $\Delta T$  and leading to more pronounced nucleation. We call this “chemical undercooling”. The chemical and thermal undercooling fronts will propagate away from the interface at rates controlled by the relative diffusivities of H<sub>2</sub>O and heat. The relative rates of migration will determine the extent to which nucleation is favoured over growth and vice versa. Although heat diffuses three orders of magnitude faster than H<sub>2</sub>O, the effect of reducing the temperature on  $\Delta T$  is much less than the effect of dehydration on  $T_L$ . An inverse consequence can be expected in the felsic domain, where both heat and H<sub>2</sub>O are being supplied. Both of these will serve to reduce (or eliminate) the amount of undercooling, and increase the likelihood of a crystal-free melt layer forming at the interface (Figure 8C).

        Last, consider the case of isothermal interaction between an H<sub>2</sub>O-saturated mafic magma and a dry (or H<sub>2</sub>O-undersaturated) felsic magma, such as that simulated by our experiments. In this case only H<sub>2</sub>O passes from mafic to felsic domains and any undercooling is entirely chemical in origin (Figure 8D). As H<sub>2</sub>O is lost to the felsic domain, a front of increasing  $T_L$  will propagate into the mafic domain. Crystallisation will tend to follow this front. Depending on the evolution of  $\Delta T$  with time, i.e. the relative rates of H<sub>2</sub>O loss (increasing  $\Delta T$ ) and crystallisation (reducing  $\Delta T$ ), the migration of the crystallisation front may be dominated either by nucleation or growth (Figure 8D).

        The above discussion makes a distinction between thermal undercooling, due to heat loss, and chemical undercooling due to the loss of H<sub>2</sub>O (or any other component that has a profound effect on  $T_L$ ). Our experiments were designed to look

627 at both chemical undercooling (interaction experiments) and thermal undercooling  
628 (cooling-rate experiments) and to compare the results.

629 In our experiments diffusion of chemical components other than H<sub>2</sub>O plays a  
630 minor role since the interacting compositions are chemically relatively similar  
631 (compare F and M composition reported in Table 2). In contrast to previous  
632 experiments on magma mixing between hydrous compositions ([Johnston and Wyllie](#)  
633 [1988](#); [van der Laan and Wyllie 1993](#)), no “uphill diffusion” of alkalis is noticed in our  
634 tests (Figure 5C-F), likely because of a lack of large K and Na gradients between F  
635 and M (Table 3). Additionally, since H<sub>2</sub>O diffusivity between interacting silicic melts  
636 is much greater than the diffusivities of major elements ([van der Laan and Wyllie](#)  
637 [1993](#)), at identical temperature and pressure conditions the flux of H<sub>2</sub>O from andesite  
638 to dacite strongly affects the diffusivities of the major chemical elements, including  
639 the “fast” alkalis ([Acosta-Vigil et al. 2005](#)). As already observed by [van der Laan and](#)  
640 [Wyllie \(1993\)](#), both K<sub>2</sub>O and Na<sub>2</sub>O are uniformly distributed through the entire length  
641 of the capsule within 44 hours, suggesting transient two-liquid equilibrium  
642 partitioning when large H<sub>2</sub>O contents (5 wt.%) are present. In our experiments the  
643 presence of > 5 wt.% H<sub>2</sub>O in the silicic melt (Figure 6C-F) should allow a faster  
644 uniform distribution of alkalis within 24 hours (Table 1); however, the molar ratio  
645 profiles (i.e. Al/K, Al/Na, and Na/K; Figure 5) do not show perfectly constant  
646 distribution profiles of alkalis throughout the glass phase (i.e. no field diffusion of  
647 alkalis; [Acosta-Vigil et al. 2002](#); [2006](#); [2012](#)). This could mean that alkalis, in  
648 presence of limited chemical gradients ( $\Delta\text{Na}_2\text{O}_{\text{mafic-felsic}} < 0.25 \text{ wt.}\%$  and  $\Delta\text{K}_2\text{O}_{\text{mafic-}}$   
649  $\text{felsic} < 0.04 \text{ wt.}\%$ ; Table 2) except for H<sub>2</sub>O (> 2 wt.%, including that the H<sub>2</sub>O gradient  
650 could be higher if the initial crystallisation of the mafic sample at equilibrium  
651 conditions is considered; Table 1), are characterised by a relatively “slow” diffusion

with respect to H<sub>2</sub>O within the timescale of our experiments (24 hours). Only after sufficient long timescale (1 week; see run product F0-M-F0 in Figure 5B) during which H<sub>2</sub>O was uniformly distributed in both interacting samples (Figure 6B), alkalis appear constantly distributed throughout the glass of the run products. In conclusion, we are confident that the microstructural features generated in our experiments received negligible contribution from diffusion of species other than H<sub>2</sub>O, which migrated from the mafic to the felsic end-member and the consequent change in  $T_L$  of the interacting magmas (Figures 6C-F, 7C-F).

#### ***Unidirectional solidification textures driven by chemical undercooling***

The microstructural and chemical results of our experiments display a number of interesting features that can be related to the changes in  $T_L$  that result from the flux of H<sub>2</sub>O from initially crystal-free mafic domain into the felsic mush. These include:

- i) Reduction of crystal size in the mafic end-member towards to the interface of the two samples (Figure 2C-F)
- ii) Hornblende and plagioclase layering in the mafic end-member in which crystals grow from the interface towards the interior of the mafic melt (Figure 2C-F)
- iii) Formation of a melt-rich “hybrid front” with hornblende-rich coronas around quartz crystals (Figure 2C-F)

As noted above, the “chilled margins” generated in the andesite during the isothermal experiments are not a consequence of thermal quenching, but they rather represent a chemical quenching due to H<sub>2</sub>O migration from the mafic to the felsic end-member at constant temperature and pressure. The linear arrangement of plagioclase and hornblende crystals in the andesite and their size reduction towards the interaction interface between dacite and andesite (Figures 2C-F, 4) is reminiscent of a number of

677 natural textures including “Willow Lake-type” layering (Poldervaart and Taubenek  
 678 1959), combed texture (Loomis 1963), comb layering (Moore and Lockwood 1973;  
 679 Lofgren and Donaldson 1975; Donaldson 1977; Lowenstern and Sinclair 1996;  
 680 Sinclair 2007), Stockscheider texture (Jackson and Power 1995; Breiter et al. 2005),  
 681 line rock texture (Webber et al. 1997; Nabelek et al. 2010) or, more generally,  
 682 unidirectional solidification texture (UST; Kormilitsyn and Manuilova 1957; Shannon  
 683 et al. 1982; Balashov et al. 2000; Breiter 2002; Hönig et al. 2010). USTs often involve  
 684 an alternation of coarse and fine crystals, leading some workers to invoke processes of  
 685 crystal growth and dissolution to operate in tandem. For example, comb layering  
 686 textures studied in pegmatitic systems (e.g. aplite-pegmatite transition; Webber et al.  
 687 1999; Baker and Freda 1999; 2001; London 2005; 2009) and orbicular rocks (Leveson  
 688 1966; Moore and Lockwood 1973; Ort 1992; Sylvester 2011), were explained as a  
 689 consequence of an Ostwald ripening process, where smaller crystals become unstable  
 690 relative to larger crystals of the same mineral composition (e.g. Boudreau and  
 691 McBirney 1997).

692 Our experiments suggest, alternatively, that USTs can be generated  
 693 isothermally simply due to volatile loss and the consequent change in  $\Delta T$ , which  
 694 drives melts locally towards nucleation-dominated and growth-dominated regimes  
 695 (Figures 8A). In our experiments the loss of H<sub>2</sub>O is a result of the H<sub>2</sub>O-saturated  
 696 nature of the mafic melt and the H<sub>2</sub>O-undersaturated nature of the felsic melt at run  
 697 conditions. The loss of H<sub>2</sub>O from mafic to felsic domains drives undercooling in the  
 698 former, promoting crystal growth. The tendency of crystals to grow perpendicular to  
 699 the interface between the two domains suggests that following initial nucleation close  
 700 to the interface, the migration of the undercooling front away from the interface  
 701 serves to maintain  $\Delta T$  at an optimum value for growth (Figure 8A). Although our

702 experiments are isothermal and isobaric, they simulate many situations in nature  
703 where magmatic H<sub>2</sub>O loss occurs. This could be, for example, when hydrous magma  
704 is exposed to fractures whereupon the pressure drops driving fluids outwards. Such  
705 features have been widely invoked in ore-forming or pegmatitic systems and may  
706 occur repeatedly if the magma keeps undergoing failure and pressure drop. In a  
707 magma the development of fractures requires a relatively high crystal content and/or a  
708 high strain-rate. More generally, we would anticipate that any process that leads to  
709 pressure drops that are transient on the same timescales as H<sub>2</sub>O diffusion in silicate  
710 melts would be capable of generating USTs. Magma mixing between H<sub>2</sub>O-rich and  
711 H<sub>2</sub>O-poor magmas, as simulated in our experiments, is just one such scenario. Our  
712 proposal is consistent with explanations of rhythmic comb-quartz and/or comb-  
713 feldspar layers developed in aplite granite groundmass attributed to abrupt adiabatic  
714 drop in pressure (due to fracturing; [Shannon et al. 1982](#)) promoting gas escape  
715 (“swinging eutectic” of [Balashov et al. 2000](#)). Thus, cooling is not a pre-requisite to  
716 UST formation. Rather it is undercooling resulting from H<sub>2</sub>O exsolution from a  
717 crystallising melt. In general, USTs are generated at supersaturated boundaries and  
718 during rapid and repeated undercooling of the magmatic system ([Fenn 1977](#); [Webber](#)  
719 [et al. 1997](#); [Nabelek et al. 2010](#)) induced by fluid release ([London 1992](#)).

720       Interaction experiments involving dacitic crystal mush show that the presence  
721 of quartz crystals also plays an important role in driving textural evolution. As the  
722 felsic sample equilibrates at the experimental conditions, the quartz crystals begin to  
723 dissolve supplying SiO<sub>2</sub> to the surrounding melt (see Supplementary Material). The  
724 consequent SiO<sub>2</sub> content increase in the residual melt increases the local volatile  
725 solubility ([Johannes and Holtz 1996](#)) and, thus, attracts more H<sub>2</sub>O from the adjacent  
726 andesite. This might explain the formation of hornblende in proximity to quartz

clusters or around single quartz crystals (Figures 2C-F, 5B) where the silicate melt contains up to 6 wt.% H<sub>2</sub>O (see H<sub>2</sub>O profiles in Figure 6C-F; see analysis spot locations in Supplementary Material). H<sub>2</sub>O destabilises plagioclase and leads to hornblende crystallisation (Yoder and Tilley 1962; Holloway and Burnham 1972; Anderson 1980). At even larger H<sub>2</sub>O in the residual dacite melt all crystallisation is suppressed and glassy rims or interstices result (see H<sub>2</sub>O profiles in Figure 6C-F; see analysis spot locations in Supplementary Material).

## Conclusions

The results of our experiments designed to explore magma mixing in nature show a number of interesting microstructural features. The “quench textures” or “chilled margins” found in our run products arise for enhanced crystal nucleation rates driven by chemical diffusion (H<sub>2</sub>O), rather than rapid cooling, showing that mafic-felsic interactions found in the field may not be simply thermal in origin. The interface, across which chemical diffusion occurs, may play a key role in textural and chemical development. Specifically, we have generated unidirectional solidification textures (USTs), or comb layering, in which crystals nucleate at the mafic-felsic interface and grow into the mafic end-member. Comb layering is not a common microstructural feature of mafic enclaves. However, it can be considered as a specific category of “chemical chilling” where crystals do not decrease only in size towards an interaction interface (against another magma composition and or a wall rock, as observed in numerous field studies; e.g. Frost and Mahood 1987; Gourgaud and Villemant 1992), but they are also arranged perpendicularly to the interface. Our experimental results indicate that USTs can be used as a textural criterion to indicate the direction of volatile transfer. This has been observed in several mafic and

ultramafic rocks displaying comb layering at the margins with juxtaposed silicic rocks (Sha 1995). Mafic rocks in contact with felsic rocks show a decrease in the volumetric proportion of hydrous minerals such as hornblende, biotite as well as apatite and titanite towards the centres of the mafic complexes. Furthermore, in the dehydration zones of mafic rocks, acicular apatite crystals are typically abundant, indicative of strong undercooling (e.g. Wyllie et al. 1962). Our experiments demonstrate the ability of chemical quenching driven by H<sub>2</sub>O-loss to generate a diversity of textures found in hydrous magmatic systems, including those associated with ore deposits.

## Acknowledgments

SNSF Grant EPM-PBEZP2\_14922 and ERC Advanced Grant CRITMAG supported this research. We acknowledge: K. Stuart and B. Buse for supporting during the EPMA, FEG-EPMA, and SEM analyses (University of Bristol); R. Hinton for assisting during the SIMS analyses (EIMF, University of Edinburgh); C. Clapham and D. Hawley for technical support (University of Bristol); J. Riker for providing high H<sub>2</sub>O content silicate glasses as standards for SIMS analysis; Alberto Luisoni AG (Switzerland), Nabaltec AG (Germany), and B. Tripoli (ETH-Zurich) for supplying quartz crystals, APYRAL 60CD, and wollastonite used in the starting materials; O. Müntener, A. Acosta-Vigil, and an anonymous reviewer for their helpful comments on an earlier version of the manuscript.

## References

- Acosta-Vigil A, London D, Dewers TA, Morgan GB VI (2002) Dissolution of corundum and andalusite in H<sub>2</sub>O-saturated haplogranitic melts at 800 °C and 200 MPa: constraints on diffusivities and the generation of peraluminous melts. *J Petrol* 43:1885-1908
- Acosta-Vigil A, London D, Morgan GB VI (2005) Contrasting interactions of sodium and potassium



778 with H<sub>2</sub>O in haplogranitic liquids and glasses at 200 MPa from hydration–diffusion experiments.  
 779 Contrib Mineral Petrol 149:276-287

780 Acosta-Vigil A, London D, Morgan GB VI, Dewers TA (2006) Dissolution of quartz, albite and  
 781 orthoclase in H<sub>2</sub>O-saturated haplogranitic melts at 800 °C and 200 MPa: diffusive transport properties  
 782 of granitic melts at crustal anatectic conditions. J Petrol 43:1885-1908

783 Acosta-Vigil A, London D, Morgan GB VI (2012) Chemical diffusion of major components in granitic  
 784 liquids: implications for the rates of homogenization of crustal melts. Lithos 153:308-323

785 Anderson JL (1980) Mineral equilibria and crystallization conditions in the late Precambrian Wolf  
 786 River rapakivi massif, Wisconsin. Am J Sci 280:289-332

787 Ardia P, Giordano D, Schmidt MW (2008) A model for the viscosity of rhyolite as a function of H<sub>2</sub>O-  
 788 content and pressure: a calibration based on centrifuge piston cylinder experiments. Geochim  
 789 Cosmochim Acta 72:6013-6123

790 Bachmann O, Bergantz GW (2004) On the origin of crystal-poor rhyolites: extracted from batholithic  
 791 crystal mushes. J Petrol 45:1565-1582

792 Balashov VN, Zraisky GP, Seltmann R (2000) Fluid-magmatic interaction and oscillation phenomena  
 793 during granite melt crystallization with water-fluoride fluid gain-loss. Petrologiya 8:563–585

794 Baker DR, Freda C (1999) Ising models of undercooled binary system crystallization: comparison with  
 795 experimental and pegmatite textures. Am Mineral 84:725-732

796 Baker DR, Freda C (2001) Eutectic crystallization in the undercooled orthoclase-quartz-H<sub>2</sub>O system:  
 797 experiments and simulations. Eur J Mineral 13:453–466

798 Bindeman IN, Perchuk LL (1993) Experimental studies of magma mixing at high pressures. Int Geol  
 799 Rev 35:721-733

800 Bindeman IN, Davis AM (1999) Convection and redistribution of alkalis and trace elements during the  
 801 mingling of basaltic and rhyolitic melts. Petrol 7:91-101

802 Blake S, Fink JH (1987) The dynamics of magma withdrawal from a density stratified dyke Earth  
 803 Planet. Sci Lett 85:516-524

804 Blundy JD (1989) The geology of the southern Adamello Massif, Italy. Dissertation, University of  
 805 Cambridge

806 Blundy JD, Sparks RSJ (1992) Petrogenesis of mafic inclusions in granitoids of the Adamello Massif,  
 807 Italy. J Petrol 33:1039-1104

808 Blundy JD, Cashman K (2001) Magma ascent and crystallization at Mount St. Helens, 1980-1986.  
809 *Contrib Mineral Petrol* 140:631-650

810 Blundy JD, Mavrogenes J, Tattitch B, Sparks RSJ, Gilmer A (2015) Generation of porphyry copper  
811 deposits by gas–brine reaction in volcanic arcs. *Nature Geosci.* 8:235-240

812 Boudreau AE, McBirney AR (1997) The Skaergaard Layered Series. Part III. Non-dynamic Layering. *J*  
813 *Petrol* 38:1003-1020

814 Boyd FR, England JL (1960) Apparatus for phase equilibrium measurements at pressures of up to 50  
815 kbars and temperatures to 1750°C. *J Geophys Res* 65:741-748

816 Breiter K (2002) From explosive breccia to unidirectional solidification textures: magmatic evolution  
817 of a phosphorus- and fluorine-rich granite system (Podlesí, Krušné hory Mts., Czech Republic). *Bull*  
818 *Czech Geol Survey* 77:67–92

819 Breiter K., Mqller A, Leichmann J, Gabas'ova' A (2005) Textural and chemical evolution of a  
820 fractionated granitic system: the Podlesí' stock, Czech Republic. *Lithos* 80:323-345

821 Bunsen R. (1851) Ueber die prozesse der vulkanischen Gesteinsbildungen Islands. *Annalen der Physik*  
822 (Leipzig) 83:197–272

823 Burnham CW, Jahns RH (1962) A method for determining the solubility of water in silicate melts. *Am*  
824 *J Sci* 260:721-745

825 Cervantes P, Wallace P (2003) Role of H<sub>2</sub>O in subduction-zone magmatism: newinsights from melt  
826 inclusions in high-Mg basalts from central Mexico. *Geology* 31:235-238

827 Czuppon G, Lukacs R, Harangi S, Mason PRD, Ntaflos T (2012) Mixing of crystal mushes and melts  
828 in the genesis of the Bogacs ignimbrite suite, northern Hungary; an integrated geochemical  
829 investigation of mineral phases and glasses. *Lithos Oslo* 148:71-85.

830 D'Lemos RS (1987) Relationships between the Cobo Granite and the Bordeaux Diorite Complex,  
831 Guernsey. PhD Dissertation, University of Bristol

832 de Saint Blanquait M, Habert G, Horsman E, Morgan SS, Tikoff B, Launeau P, Gleizes G (2006)  
833 Mechanisms and duration of non-tectonically assisted magma emplacement in the upper crust: the  
834 Black Mesa pluton, Henry Mountains, Utah. *Tectonophys* 428:1-31

835 Devine JD, Gardner JE, Brack HP, Layne GD, Rutherford MJ (1995) Comparison of microanalytical  
836 methods for estimating H<sub>2</sub>O contents of silicic volcanic glasses. *Am Mineral* 80:319-328

837 Donaldson CH (1977) Laboratory duplication of comb layering in the Rhum pluton. *Mineral. Magaz.*

838 41:323-336

839 Fedkin A, Seltnann R, Bezmen N, Zraisky G (2002) Experimental testing of line rocks in Li-F  
840 granites: evidence from superliquidus experiments with F and P added. Bull Czech Geol Survey  
841 77:113-125

842 Fenn PM (1977) The nucleation and growth of alkali feldspars from hydrous melts. Can Mineral  
843 15:135-161.

844 Field L, Blundy JD, Brooker RA, Wright T, Yirgu G (2012) Magma storage conditions beneath  
845 Dabbahu Volcano (Ethiopia) constrained by petrology, seismicity and satellite geodesy. Bull Volcanol  
846 74:981-1004

847 Frost TP, Mahood GA (1987) Field, chemical, and physical constraints on mafic-felsic magma  
848 interaction in the Lamarck Granodiorite, Sierra Nevada, California. Geol Soc of Am Bull 99:272-291

849 Gourgau A, Villemant B (1992) Evolution of magma mixing in an alkaline suite: the Grande Cascade  
850 sequence (Monts-Dore, French Massif Central). Geochemical modeling. J Volcanol Geotherm Res  
851 52:255-275

852 Grasset O, Albarade F, Hybridization of mingling magmas with different densities. Earth Planet Sci  
853 Lett 121:327-332

854 Hattori KH, Keith JD (2001) Contribution of mafic melt to porphyry copper mineralization: evidence from  
855 Mount Pinatubo, Philippines, and Bingham deposit, Utah. Mineral. Deposita 36:799-806

856 Hinton RW (1990) Ion microprobe trace-element analysis of silicates.measurement of multi-element  
857 glasses. Chem Geol 83:11-25

858 Hofmann AW (1980) Diffusion in natural silicate melts: A critical review. In: Hargraves RB (ed),  
859 Physics of magmatic processes. Princeton University Press, pp 385-417

860 Holloway J.R., Burnham CW (1972) Melting relations of basalt with equilibrium water pressure less  
861 than total pressure. J Petrol 13:1-29

862 Hönig S, Leichmann J, Novak M (2010) Unidirectional solidification textures and garnet layering in Y-  
863 enriched garnet-bearing aplite–pegmatites in the Cadomian Brno Batholith, Czech Republic. J Geosci  
864 55:113-129

865 Hort M (1998) Abrupt change in magma liquidus temperature because of volatile loss or magma  
866 mixing: effects on nucleation, crystal growth and thermal history of the magma. J Petrol 39:1063-1076

867 Humphreys MCS, Kearns SL, Blundy JD (2006), SIMS investigation of electron-beam damage to

868 hydrous, rhyolitic glasses: implications for melt inclusion analysis. *Am Mineral* 91:667-679

869 Humphreys MCS, Edmonds M, Christopher T, Hards V (2010) Magma hybridisation and diffusive  
870 exchange recorded in heterogeneous glasses from Soufrière Hills Volcano, Montserrat. *Geophys Res*  
871 *Lett* 37:L00E06

872 Jackson G.E.A., Power G.M. (1995) Columnar, branching and curved feldspar growth in the St  
873 Michael's Mount Granite, Cornwall. *Proc. Ussher Soc* 8:363-367

874 Johannes WJ, Bell PM, Mao HK, Boettcher AL, Chipman DW, Hays JF, Newton RC, Seifert F (1971)  
875 An interlaboratory comparison of piston-cylinder pressure calibration using the albite breakdown  
876 reaction. *Contrib Mineral Petrol* 32:24-38

877 Johannes WJ, Holtz F (1996) *Petrogenesis and Experimental Petrology of Granitic Rocks*. Springer, pp.  
878 335

879 John BE, Blundy JD (1993) Emplacement-related deformation of granitoidmagmas, southern Adamello  
880 Massif, Italy. *Geol Soc Am Bull* 105:1517-1541

881 Johnston AD, Wyllie PJ (1988) Interaction of granitic and basic magmas: experimental observations on  
882 contamination processes at 10 kbar with H<sub>2</sub>O. *Contrib Mineral Petrol* 98:352-362

883 Kormilitsyn VS, Manuilova MM (1957) Rhythmic banded quartz porphyry, Bugdai Mountain,  
884 southeast Transbaykal region. *Zapiski Vsesoyouz Mineral Obsch* 86:355-364.

885 Kouchi A, Sunagawa I (1982) Experimental study of mixing of basaltic and dacitic magmas, *Sci Rep*  
886 *Tohoku University* 15:163-175

887 Kouchi A, Sunagawa I (1985) A model for mixing basaltic and dacitic magmas as deduced from  
888 experimental data. *Contrib Mineral Petrol* 89:17-23

889 Koyaguchi T, Blake S (1989) The dynamics of magma mixing in a rising magma batch. *Bull Volcanol*  
890 52:127-137

891 Lange RA, Carmichael ISE (1987) Densities of Na<sub>2</sub>O-K<sub>2</sub>O-CaO-MgO-FeO-Fe<sub>2</sub>O<sub>3</sub>-Al<sub>2</sub>O<sub>3</sub>-TiO<sub>2</sub>-SiO<sub>2</sub>  
892 liquids: new measurements and derived partial molar properties. *Geochim Cosmochim Acta* 51:2931-  
893 2946

894 Laumonier M, Scaillet B., Arbaret L., Champallier R (2014) Experimental simulation of magma  
895 mixing at high pressure. *Lithos* 196:281-300

896 Leshner CE (1994) Kinetics of Sr and Nd exchange in silicate liquids: Theory, experiments, and  
897 applications to uphill diffusion, isotopic equilibration, and irreversible mixing of magmas. *J Geophys*

898 Res 99:9585-9604

899 Leuthold J, Müntener O, Baumgartner LP, Putlitz B, Ovtcharova M, Schaltegger U (2012) Time  
 900 resolved construction of a bimodal laccolith (Torres del Paine, Patagonia). *Earth Planet Sci Lett* 325-  
 901 326:85-92

902 Leveson DJ (1966) Orbicular rocks: a review. *Geol Soc Am Bull* 77:409-426

903 Lofgren GE, Donaldson CH (1975) Curved branching crystals and differentiation in comb-layered  
 904 rocks. *Contrib Mineral Petrol* 49:309-319

905 London D (1992) The application of experimental petrology to the genesis and crystallization of  
 906 granitic pegmatites. *Can Mineral* 30:499-540

907 London D (2005) Granitic pegmatites: an assessment of current concepts and directions for the future.  
 908 *Lithos* 80:271-303

909 London D (2008) Pegmatites. *Can Mineral Sp Publ* 10, pp. 347

910 Loomis AA (1963) Noritic anorthositic bodies in the Sierra Nevada Batholith. *Mineral Soc Am Spec*  
 911 *Paper* 1:62-68

912 Lowenstern JB, Sinclair WD (1996) Exsolved magmatic fluid and its role in the formation of comb-  
 913 layered quartz at the Cretaceous Logtong W-Mo deposit, Yukon Territory, Canada. *Trans Royal Soc*  
 914 *Edinburgh: Earth Sciences* 87:291-303

915 Makhlof AR, Newton RC, Manning CE, Experimental determination of liquidus H<sub>2</sub>O contents of  
 916 simple granites at deep crustal conditions. <http://adsabs.harvard.edu/abs/2014AGUFM.V51C4778M>

917 Mao HK, Bell PM (1971) Behavior of thermo-couples in the single-stage piston-cylinder apparatus.  
 918 *Carnegie Inst Wash Year Book* 691:207-216

919 McDade P, Wood BJ, van Westrenen W, Brooker RA, Gudmudsson G, Soulard H, Najorka J, Blundy  
 920 JD (2002) Pressure corrections for a selection of piston-cylinder cell assemblies, *Mineral Magaz*  
 921 66:1021–1028

922 Merrill RB, Wyllie PJ (1975) Kaersutite and kaersutite eclogite from Kakanui, New Zealand: water  
 923 excess and water deficient melting to 30 kilobars. *Geol Soc Am Bull* 86:555-570

924 Moore JG, Lockwood JP (1973) Origin of comb layering and orbicular structure, Sierra Nevada  
 925 Batholith, California. *Geol Soc Am Bull* 84:1-20

926 Morgan GB VI, Acosta-Vigil A, London D (2008) Diffusive equilibration between hydrous  
 927 metaluminous-peraluminous haplogranite liquid couples at 200 MPa (H<sub>2</sub>O) and alkali transport in

928 granitic liquids. *Contrib Mineral Petrol* 155:257-269

929 Morgavi D, et al. (2012) Interactions between rhyolitic and basaltic melts unraveled by chaotic mixing  
 930 experiments. *Chem Geol* doi:10.1016/j.chemgeo.2012.10.003

931 Murphy MD, Sparks RSJ, Barclay J, Carroll MR, Brewer TS (2000) Remobilization of andesite magma  
 932 by intrusion of mafic magma at the Soufriere Hills Volcano, Montserrat, West Indies. *J Petrol* 41:21-42

933 Nabelek PI, Whittington AG, Sirbescu M-LC (2010) The role of H<sub>2</sub>O in rapid emplacement and  
 934 crystallization of granite pegmatites: resolving the paradox of large crystals in highly undercooled  
 935 melts. *Contrib Mineral Petrol* 160:313-325

936 Ni H, Zhang Y (2008) H<sub>2</sub>O diffusion models in rhyolitic melt with new high pressure data. *Chem Geol*  
 937 250:68-78

938 Oldenburg CM, Spera FJ, Yuen DA, Sewell G (1989) Dynamic mixing in magma bodies: theory,  
 939 simulations and implications. *J Geophys Res* 94:9215-9236

940 O'Neil HSC (1986) Mo-MoO<sub>2</sub> (MOM) oxygen buffer and the free energy of formation of MoO<sub>2</sub>. *Am*  
 941 *Mineral* 71:1007-1010

942 Ort MH (1992) Orbicular volcanic rocks of Cerro Panizos: their origin and implications for orb  
 943 formation. *Geol Soc Am Bull* 84:1-20

944 Perugini D, Poli G (2004) Analysis and numerical simulation of chaotic advection and chemical  
 945 diffusion during magma mixing: petrological implications. *Lithos* 78:43-66

946 Plank T, Kelley KA, Zimmer MM, Hauri EH, Wallace PJ (2013) Why do mafic arc magmas contain  
 947 ~4 wt% water on average? *Earth Planet Sci Lett* 364:168-179

948 Pistone M (2012) Physical properties of crystal- and bubble-bearing magmas. Dissertation, ETH-  
 949 Zurich

950 Pistone M, Caricchi L, Ulmer P, Burlini L, Ardia P, Reusser E, Marone F, Arbaret L (2012)  
 951 Deformation experiments of bubble- and crystal-bearing magmas: rheological and microstructural  
 952 analysis. *J Geophys Res* 117:doi:10.1029/2011JB008986

953 Pistone M, Caricchi L, Ulmer P, Reusser E, Ardia P (2013) Rheology of volatile-bearing crystal  
 954 mushes: mobilization vs. viscous death. *Chem Geol* 345:16-39

955 Poldervaart A, Taubeneck WH (1959) Layered intrusions of the Willow Lake type. *Geol Soc Am Bull*  
 956 70:1395-1398

957 Romine WL, Whittington AG, Nabelek PI, Hofmeister AM (2012) Thermal diffusivity of rhyolitic

958 glasses and melts: effects of temperature, crystals and dissolved water. *Bull Volcanol* 74:2273-2287

959 Rouse P (2000) Experimental phase equilibria of sodic phonolites from Montaña Blanca, Tenerife.  
 960 Dissertation, University of Bristol

961 Ruprecht P, Bachmann O (2010) Pre-eruptive reheating during magma mixing at Quizapu volcano and  
 962 the implications for the explosiveness of silicic arc volcanoes. *Geology* 38:919-922

963 Ruprecht P, Bergantz GW, Cooper KM, Hildreth W (2012) The crustal magma storage system of  
 964 Volcán Quizapu, Chile, and the effects of magma mixing on magma diversity. *J Petrol* 53:801-840

965 Rutter EH, Brodie KH, Irving DH (2006) Flow of synthetic, wet, partially molten “granite” under  
 966 undrained conditions: an experimental study. *J Geophys Res* 111:doi.org/10.1029/2005JB004257

967 Sinclair WD (2007) Porphyry deposits, In Goodfellow WD (ed), *Mineral Deposits of Canada: A*  
 968 *Synthesis of Major Deposit-Types, District Metallogeny, the Evolution of Geological Provinces, and*  
 969 *Exploration Methods*. *Geol Ass Can - Mineral Deposits Div - Spec Pub* 5:223-243

970 Sato E, Sato H (2009) Study of effect of magma pocket on mixing of two magmas with different  
 971 viscosities and densities by analogue experiments, *J Volcanol Geotherm Res* 181:115-123

972 Saunders KE, Buse B, Kilburn M, Kearns S, Blundy JD (2014) Nanoscale characterisation of crystal  
 973 zoning. *Chem Geol* 364:20-32

974 Sha L-K (1995) Genesis of zoned hydrous ultramafic/mafic-silicic intrusive complexes: an MHFC  
 975 hypothesis, *Earth Sci Rev* 39:59-90

976 Shannon JR, Walker BM, Carten RB, Geraghty EP (1982) Unidirectional solidification textures and  
 977 their significance in determining relative ages of intrusions at the Henderson Mine, Colorado. *Geology*  
 978 10:293-297

979 Sisson TW, Layne GD (1993) H<sub>2</sub>O in basalt and basaltic andesite glass inclusions from four  
 980 subduction-related volcanoes. *Earth Planet Sci Lett* 117:619-635

981 Sisson TW, Grove TL (1993) Temperatures and H<sub>2</sub>O contents of low MgO high-alumina basalts.  
 982 *Contrib Mineral Petrol* 113:167-184

983 Sisson TW, Grove TL, Coleman DS (1996) Hornblende gabbro sill complex at Onion Valley,  
 984 California, and a mixing origin for the Sierra Nevada batholith. *Contrib Mineral Petrol* 126:81-108

985 Sparks RSJ, Marshall LA (1986) Thermal and mechanical constraints on mixing between mafic and  
 986 silicic magmas. *J Volcanol Geotherm Res* 29:99-124

987 Sylvester AG (2011) The nature and polygenetic origin of orbicular granodiorite in the Lower Castle  
 988 Creek pluton, northern Sierra Nevada batholith, California. *Geosphere* 7:1-9  
 989 Ulmer P (1986) Basische und ultrabasische Gesteine des Adamello (Provinzen Brescia und Trento,  
 990 Norditalien). Dissertation, ETH-Zürich  
 991 Ulmer P (2001) Partial melting in the mantle wedge: the role of H<sub>2</sub>O in the genesis of mantle-derived  
 992 “arc-related” magmas. *Phys Earth Planet Inter* 127:215-232  
 993 Tuttle OF, Bowen NL (1958) Origin of granite in the light of experimental studies in the system  
 994 NaAlSi<sub>3</sub>O<sub>8</sub>-KAlSi<sub>3</sub>O<sub>8</sub>-SiO<sub>2</sub>-H<sub>2</sub>O. *Geol Soc Am Mem* 74, pp. 153  
 995 van der Laan SR, Wyllie PJ (1993) Experimental interaction of granitic and basaltic magmas and  
 996 implications for mafic enclaves. *J Petrol* 34:491-517  
 997 Watson EB (1981) Diffusion in magmas at depth in the earth: the effects of pressure and dissolved  
 998 H<sub>2</sub>O. *Earth Planet Sci Lett* 52:291-301  
 999 Watson EB (1982) Basaltic contamination by continental crust: some experiments and models. *Contrib*  
 1000 *Mineral Petrol* 80:73-87  
 1001 Watson EB, Jurewicz SR (1984) Behaviour of alkalis during diffusive interaction of granitic xenoliths  
 1002 with basic magmas. *J Geol* 92:121-131  
 1003 Webb SL, Dingwell DB (1990) The onset of non-Newtonian rheology of silicate melts: a fiber  
 1004 elongation study. *Phys Chem Miner* 17:125-132  
 1005 Webber KL, Falster AU, Simmons W, Foord EE (1997) The role of diffusion-controlled oscillatory  
 1006 nucleation in the formation of line rock in pegmatite-aplite dikes. *J Petrol* 38:1777-1791  
 1007 Webber KL, Simmons WB, Falster AU, Foord EE (1999) Cooling rates and crystallization dynamics of  
 1008 shallow level pegmatite-aplite dikes, San Diego County, California. *Am Mineral* 84:708-717  
 1009 Wyllie PJ, Cox KG, Biggar GM (1962) The habit of apatite in synthetic systems and igneous rocks. *J*  
 1010 *Petrol* 3:238-243  
 1011 Yoder HSJr, Stewart DB, Smith JR (1957) Ternary feldspars. Carnegie Institution of Washington, Year  
 1012 book 55:206-214  
 1013 Yoder HSJr, Tilley C.E. (1962) Origin of basalt magmas: An experimental study of natural and  
 1014 synthetic rock systems. *J Petrol* 3:342-532  
 1015 Yoder HSJr (1973) Contemporaneous basaltic and rhyolitic magmas. *Am Mineral* 58:153-171  
 1016



## FIGURE CAPTIONS

**Figure 1:** Examples of textures produced by hydrous mafic magmas from the Tertiary Adamello Batholith, (Alps, Italy). **A)** Polished section from the Val Fredda Complex (Blundy and Sparks 1992) showing interaction between hornblende-rich gabbro (lower dark portion) and tonalite host (upper lighter portion). The interaction between the two rocks is marked by a fine-grained “chilled margin” to the gabbro. Wisps of solidified mafic magma can be seen rising from the interface and permeating the tonalite, which is rendered anomalously darker as a consequence. Rounded, grey quartz phenocrysts in the tonalite have developed hornblende-bearing coronas as a consequence of interaction with mafic magma. **B)** Example of comb layering (a variant of unidirectional solidification texture - UST) from the north-west flanks of Cornone di Blumone (John and Blundy 1993). Black hornblendes grow upwards from the curved interface in the centre of the photograph. A second comb layer lies above the main layer, separated from the first by banded, fine-grained rock. The comb layers cut equigranular gabbro host rock. **C)** Another example of comb layering from the same locality as (B). In this case the comb texture is defined by elongate white plagioclase crystals growing perpendicular to an interface (near coin). Mafic rock below the interface is uniformly fine-grained and banded. A second comb layer lies beneath the fine-grained layer. In the main comb layered region plagioclase grain size increases upwards away from the interface, while the number density of plagioclase grains decreases. The comb layer is asymmetric and abuts medium-grained host diorite at the top of the photograph.

**Figure 2:** BSE images of key textural features associated with interfaces in the different run products: **A)** F0-M, **B)** F0-M-F0, **C)** F50-M, **D)** F60-M-F60, **E)** F70-M, **F)** F80-M-F80, **G)** F50-M, **H)** M-M. Run details given in Table 1. The phases present: vesicles (black circles), hornblende (very light grey objects in M and light grey objects in F0), plagioclase (light grey objects), oxides (white objects), quartz (very dark grey objects), and silicic glass (dark grey matrix). The black and white scale bars are: 500 µm in **A**, 200 µm in **C-F, H**, and 100 µm in **G**.

**Figure 3:** BSE images of textures of cooling experiments on starting material M: **A-B)** fast cooling (1000 to 950 °C; 3.3 °C/second; 4 kbar), and **C-D)** slow cooling (1000 to 950 °C; 1 °C/minute; 4 kbar). The phases present have the same grey-scale characteristics as Figure 2. Images are arranged with the

sample periphery on the right hand side and sample core on the left hand side. The black scale bar is 300  $\mu\text{m}$  in **A-B** and 100  $\mu\text{m}$  in **C-D**.

**Figure 4:** **A)** Representative EPMA-based characteristic X-ray distribution maps of run product F0-M. **B)** Representative SEM-based false-colour characteristic X-ray distribution maps of run product F70-M. Both grey (**A**) and colour scales (**B**) of the X-ray distribution maps are expressed in wt.%.

**Figure 5:** EPMA- and SIMS-based molar ratio ( $\text{ASI} = \text{Al}_2\text{O}_3/[\text{CaO}+\text{Na}_2\text{O}+\text{K}_2\text{O}]$ , Al/Si, Al/Na, Al/K, and Na/K) profiles across the interaction interface in different run products. EPMA- and SIMS-based concentration profiles of major oxides and trace elements are reported in the Supplementary Material. Data are displayed according to the distance of the analysis spots from the interface(s) (see Supplementary Material).

**Figure 6:** SIMS- and EPMA-based  $\text{H}_2\text{O}$  contents along the different run products (except run products F50-F0 and M-M, which are reported in the Supplementary Material). Data are displayed according to the distance of the analysis spots from the interface(s) (see Supplementary Material).

**Figure 7:** Calculated local liquidus temperatures ( $T_L$ , computed using the model of [Makhluף et al. 2014](#), based on EPMA and SIMS data; standard error of  $\pm 4^\circ\text{C}$ ) across the different run products. A few computed values of  $T_L$  in the dacite of run products F50-M, F60-M-F60, and F70-M are  $< 800^\circ\text{C}$ , and therefore not displayed.

**Figure 8:** **A)** Normalised temperature ( $T' = T_{\text{experimental}} / T_L$ ) versus dimensionless crystal nucleation and growth rate (after [Hort 1998](#)). The grey line (at  $T' = 1$ ) separates the field of supercooling ( $T' > 1$ ) from that of undercooling ( $T' < 1$ ). Black and brown lines indicate the Gaussian trends of crystal growth and nucleation rate respectively. Red and blue areas indicate the nucleation and growth of crystals in the dacite and andesite respectively. The orange area indicates common conditions of nucleation and growth of crystals in the two interacting domains. Two inset schematics indicate the  $\text{H}_2\text{O}$  content conditions under which crystal nucleation rate is favoured (low  $\text{H}_2\text{O}$  content) or crystal growth rate is supported (high  $\text{H}_2\text{O}$  content). **B-D)** Conceptual diagrams showing the effect of

undercooling (i.e. temperature difference,  $\Delta T$ , between the contact temperature at the interface,  $T_{interface}$ , and the liquidus temperature of the felsic (blue),  $T_{L(felsic)}$ , or the liquidus temperature of the mafic magma (red),  $T_{L(mafic)}$ ) in three end-member scenarios: **B)** heat diffusion from anhydrous mafic to anhydrous felsic magma, which generates chilled margins at the interface of the mafic domain and limited partial melting of the felsic domain; **C)** both heat and H<sub>2</sub>O diffusion from H<sub>2</sub>O-saturated mafic to anhydrous felsic magma, which causes dramatic crystallisation of the mafic domain, including the formation of chilled margins at the interface, and diffuse partial melting of the felsic domain; **D)** isothermal (i.e.  $T_{interface}$  = actual temperature of the interacting magmas,  $T_{actual}$ ) H<sub>2</sub>O diffusion from H<sub>2</sub>O-saturated mafic to anhydrous (or H<sub>2</sub>O-undersaturated) felsic magma, which promotes the generation of comb layering in the mafic domain and super-liquidus melt at the interface in the felsic domain. The H<sub>2</sub>O diffusion promotes a drop of the  $T_{L(felsic)}$ , with enrichment of H<sub>2</sub>O in the residual melt. Conversely, H<sub>2</sub>O release from the mafic melt favours an increase of the  $T_{L(mafic)}$  with an inward crystallisation (from the mafic-felsic interface to the mafic core), which is initially nucleation-driven (evidenced by the presence of microlites at the interface; Figures 1A-B), then growth-driven (characterised by elongate crystals arranged in a comb layering structure towards the mafic-felsic interface; Figures 1B-C). The diagram shows the schematics of textures generated during the experiments. Different crystals are: quartz (red hexagons) with orange SiO<sub>2</sub>-dissolution rims, hornblende (black rectangles), plagioclase (light brown rectangles) and Fe-Ti oxides (yellow squares).

## TABLE CAPTIONS

**Table 1:** Summary of the high-temperature and high-pressure experiments from this study. Abbreviations:  $\phi$  = sample diameter;  $l$  = sample length;  $V$  = sample volume;  $m$  = sample mass;  $\rho$  = sample density at room conditions;  $V_{felsic} / V_{mafic}$  = total volume ratio between felsic and mafic sample;  $m_{felsic} / m_{mafic}$  = total mass ratio between felsic and mafic sample;  $\rho_{felsic} / \rho_{mafic}$  = total density ratio between felsic and mafic sample;  $T$  = temperature;  $P$  = pressure; **Glass** = residual silicic glass; **Hbl** = hornblende; **Plag** = plagioclase; **Ox** = Fe-Ti oxide; **Qz** = quartz; **Bubble** = gas bubble. The values of volumetric proportions of the different phases within the single samples in the run products are reported in vol.%. Runs M\_cooling\_01 and M\_cooling\_02 were conducted with cooling rates of 3.3 °C/second (fast cooling); runs M\_cooling\_03 and M\_cooling\_04 were conducted with cooling rates of

1 °C/minute (slow cooling). Underlined = experiment conducted by using a cold seal vessel; (\*) = experiment performed with Pt capsule.

**Table 2:** Representative EPMA analyses of the bulk matrix glass from starting materials and mineral compositions from selected experimental charges from this study. Chemical analyses are volatile-free basis. H<sub>2</sub>O contents here reported are from SIMS analyses (\*); H<sub>2</sub>O contents are also calculated using the by-difference method (see Figure 6). Uncertainties based on counting statistics of the reported concentrations are in the range of 0.5-1.5% for SiO<sub>2</sub>, Al<sub>2</sub>O<sub>3</sub> and CaO, 1-7% for Na<sub>2</sub>O and K<sub>2</sub>O, 3-22% for TiO<sub>2</sub>, FeO<sub>T</sub>, MgO and MnO. The maximum uncertainties for reported molar ratios, calculated via error propagation, are: 31% for ASI (Al<sub>2</sub>O<sub>3</sub>/[CaO+Na<sub>2</sub>O+K<sub>2</sub>O]), 3% for Na/K, 1% for Al/K, 2% for Al/Na, and 10% for Al/Si. In italics = selected hornblende mineral located at a distance of ~50 µm far from the closest quartz crystal; the analysis of the other hornblendes display higher SiO<sub>2</sub> content (~50-55 wt.%) due to larger SiO<sub>2</sub> content in the glass surrounding quartz crystals, as evidenced by FEG-probe analyses (Supplementary Material).

**Table 3:** EPMA-based chemical profiles within the glass phase in the experimental charges simulating sample-sample interaction from this study (see also Figure 5). Chemical analyses are volatile-free basis; H<sub>2</sub>O contents are calculated using the by-difference method. Locations of the EPMA and H<sub>2</sub>O-SIMS analysis spots are displayed in the Supplementary Material.

**Table 4:** SIMS analyses of the silicic glass in the run products simulating sample-sample interaction (see also Figure 6). All data are Si-normalised and corrected following the Geological and Environmental Reference Materials (GeoReM) database. Locations of the analysis spots are displayed in the Supplementary Material.

## SUPPLEMENTARY MATERIAL

**Figure SM1: A-D)** SEM-based BSE images detailing the sample-sample interaction interface of the run products: **A)** F0-M; **B)** F0-M-F0; **C)** F50-M; **D)** F60-M-F60; **E)** F70-M; **F)** F80-M-F80; **G)** F50-F0; **H)** M-M; **I)** F50-M (CSV). The phases present: vesicles (black circles), hornblende (very light grey objects in M and light grey objects in F0), plagioclase (light grey objects), oxides (white objects),

quartz (very dark grey objects), and silicic glass (dark grey matrix). Red and brown dots indicate EPMA analysis spots; blue and purple dots indicate SIMS analysis spots in the felsic and mafic domain respectively (and, felsic mush and felsic crystal-free sample of the run product F50-F0 respectively); yellow and orange dots indicate SIMS analysis spots in the upper mafic and lower mafic domain respectively. Black arrows indicate the location of the interfaces between samples. The black scale bar is 1 mm in all images.

**Figure SM2:** BSE image showing representative FEG-EPMA-based analysis spots reporting the SiO<sub>2</sub> content across quartz crystal and surrounding silicic glass in the run product F70-M. Black circles of Profile 1 (**A**) and Profile 2 (**B**) (see analysis spots data reported in Table SM1).

**Figure SM3:** EPMA- and SIMS-based concentration profiles of major elements across the interaction interface in different run products. Data are displayed according to the distance of the analysis spots from the interface(s) (see Figure SM1).

**Figure SM4:** SIMS-based concentration profiles of trace elements and SIMS- and EPMA-based H<sub>2</sub>O contents along the different run products (including F50-F0 and M-M). Data are displayed according to the distance of the analysis spots from the interface(s) (see Figure SM1).

**Table SM1:** Representative FEG-EPMA data from analysis spots of the quartz crystals and surrounding silicic glass in the experimental charge F70-M. All presented data are affected by 1 to 5% standard error. Locations of the analysis spots are displayed in Figure SM2.



Figure 1

A

*Qz-Tonalite*

*Hbl-Gabbro*

B

70 mm

C



Figure 2

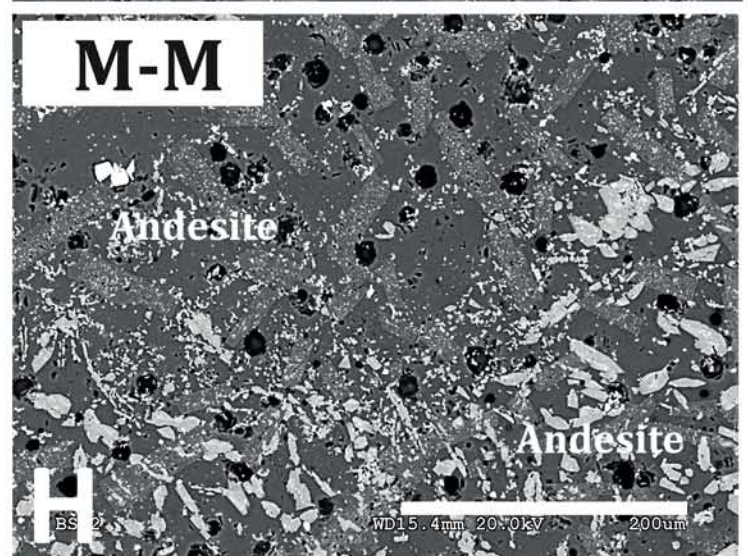
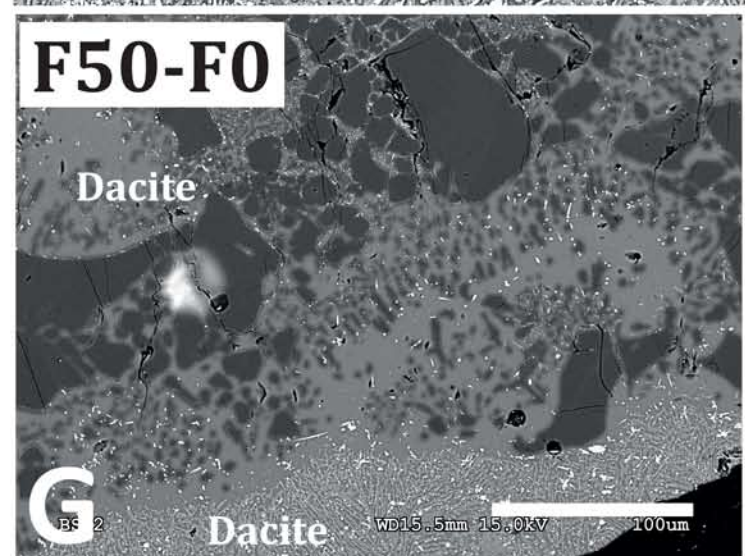
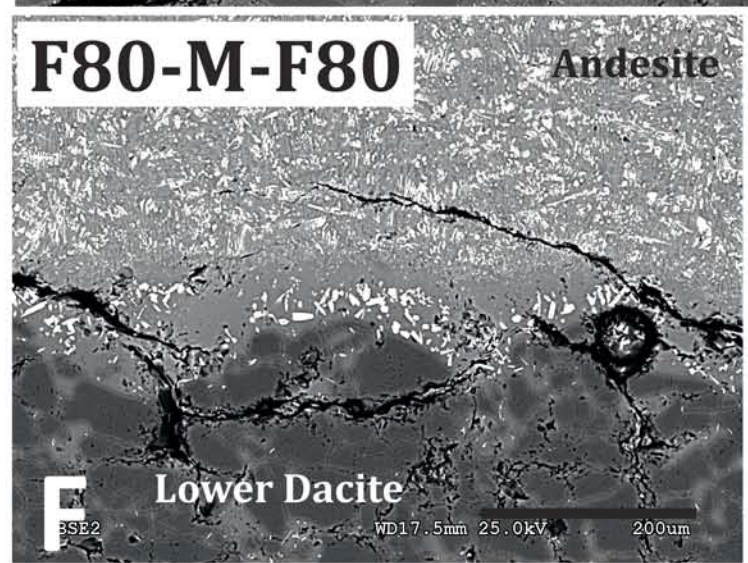
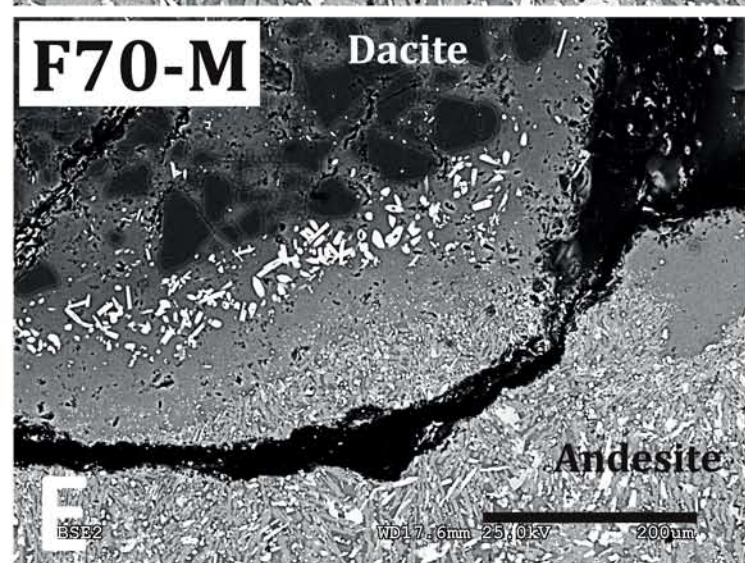
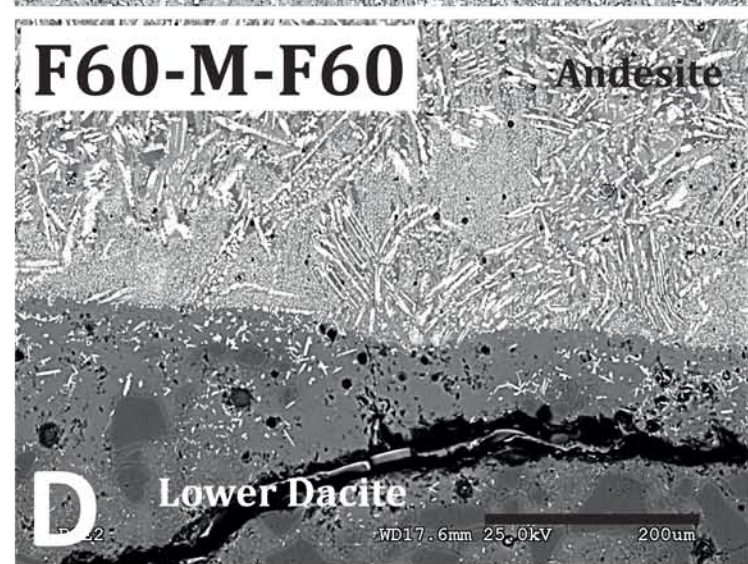
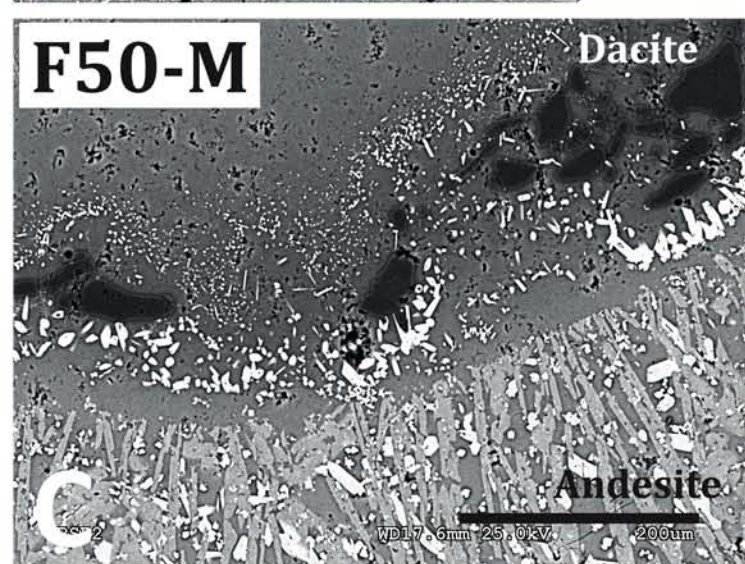
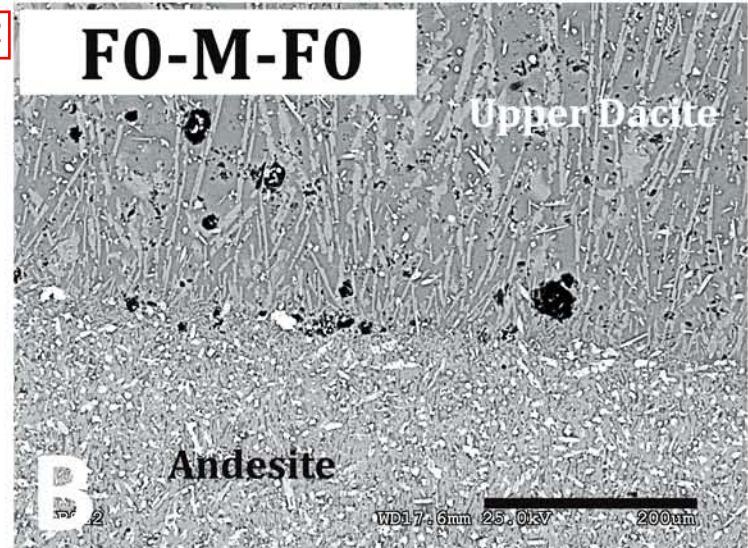
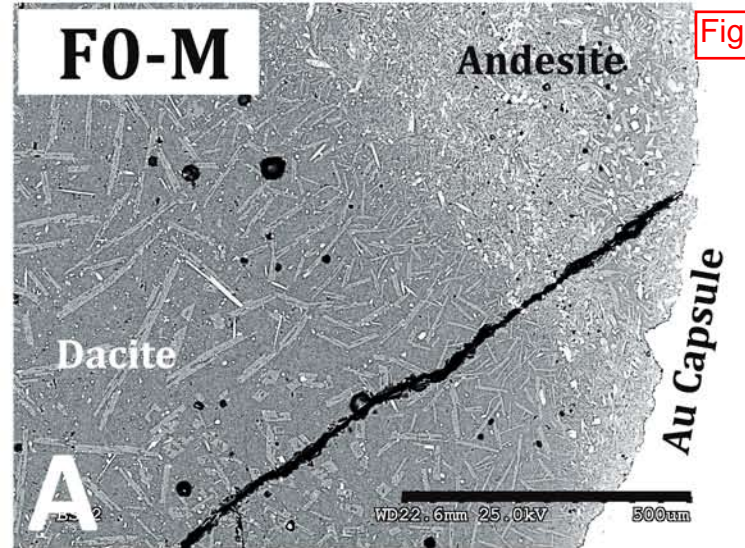
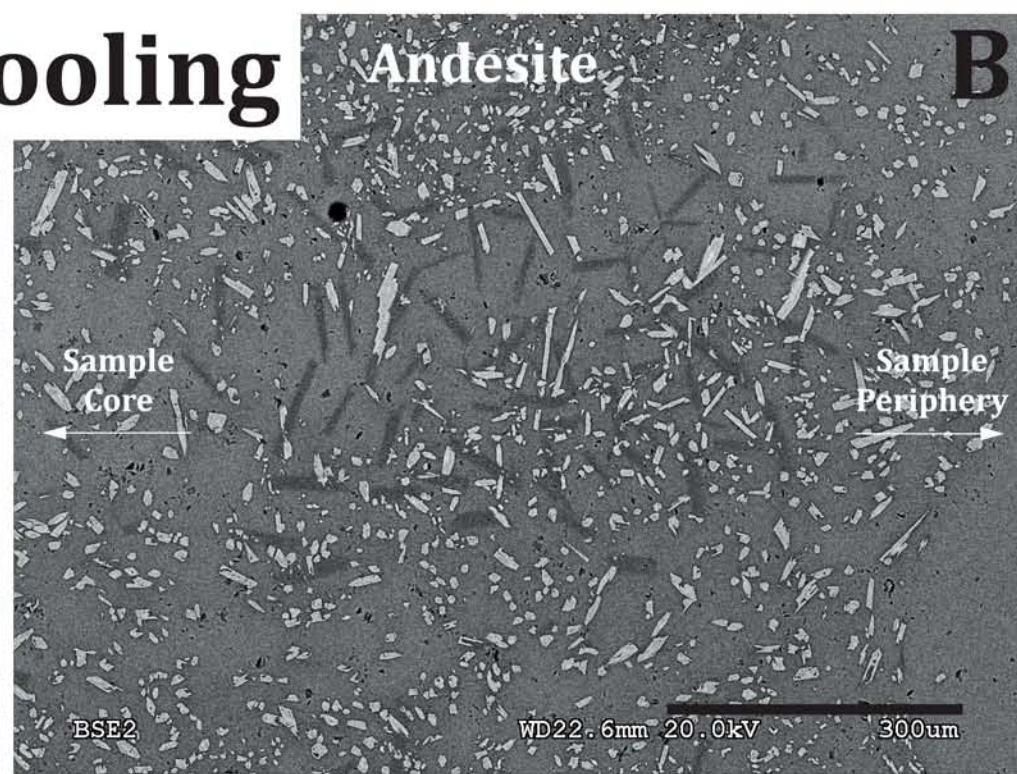
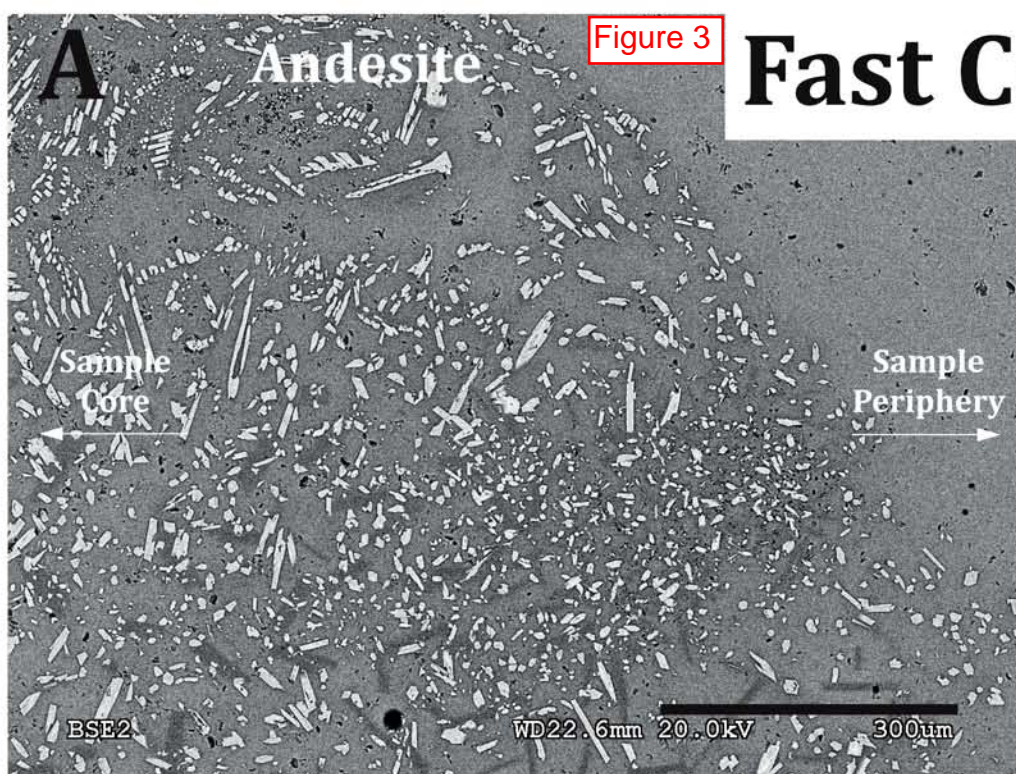




Figure 3

# Fast Cooling



# Slow Cooling

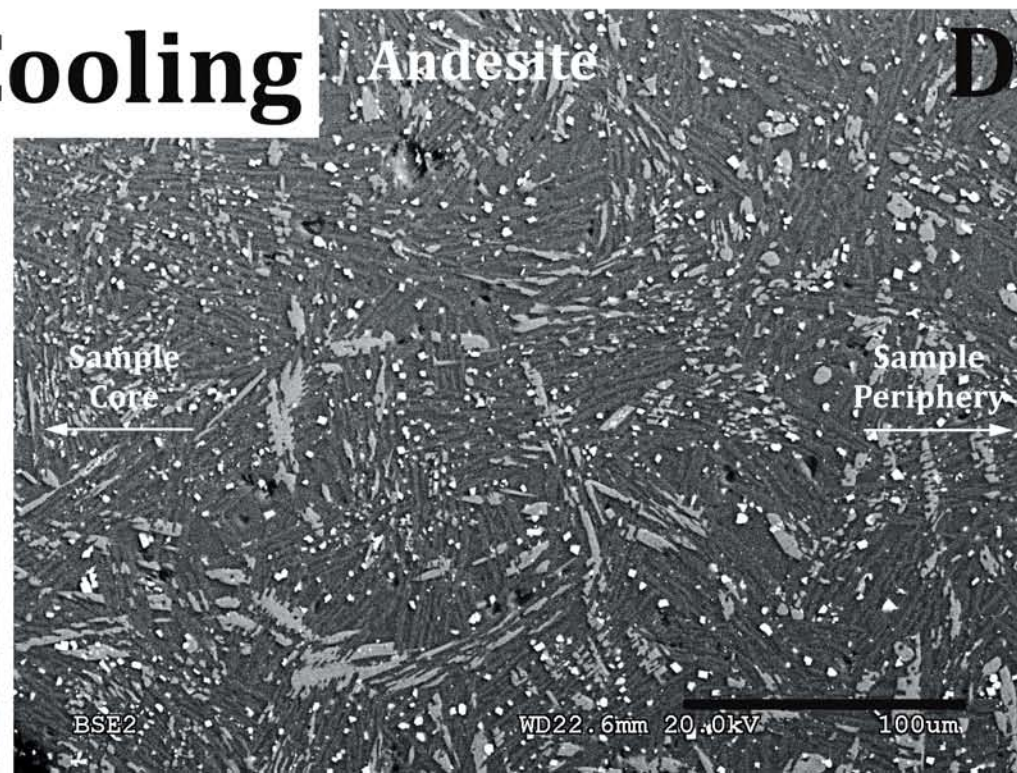
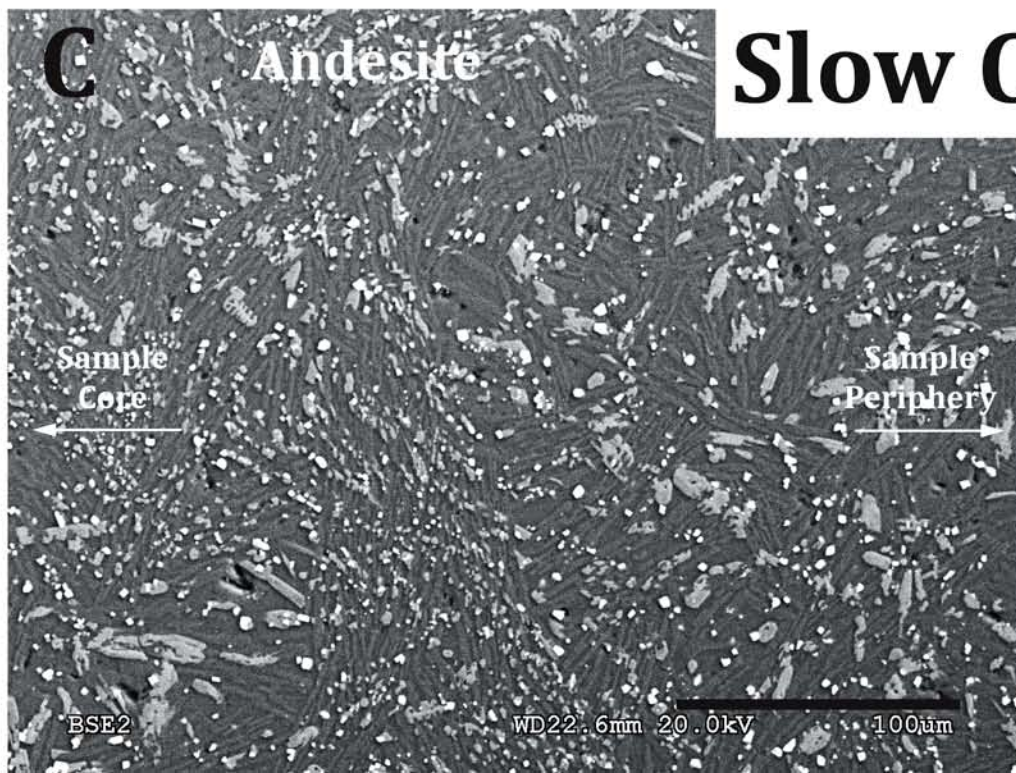
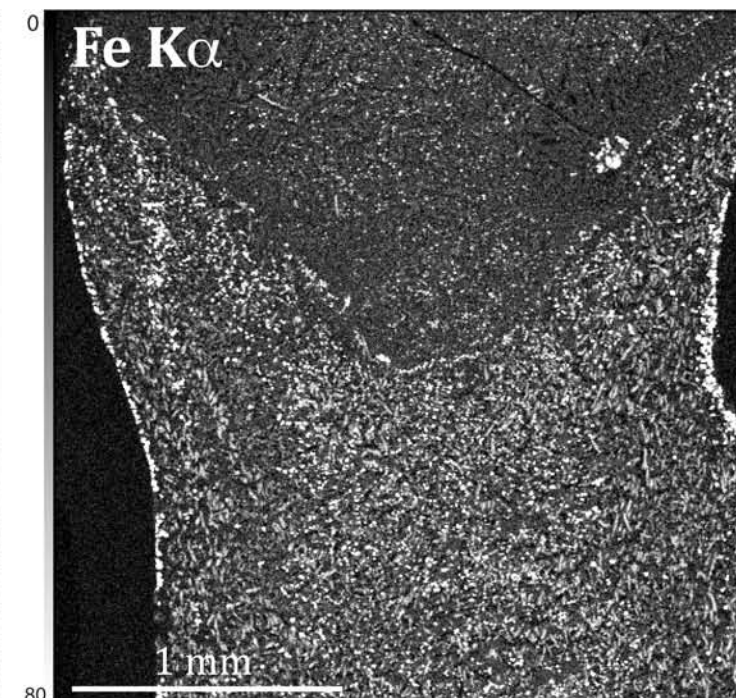
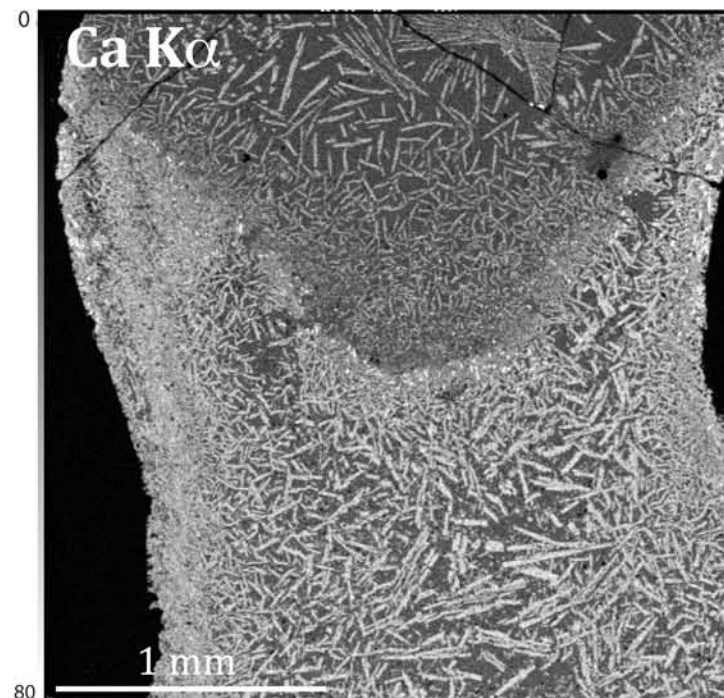
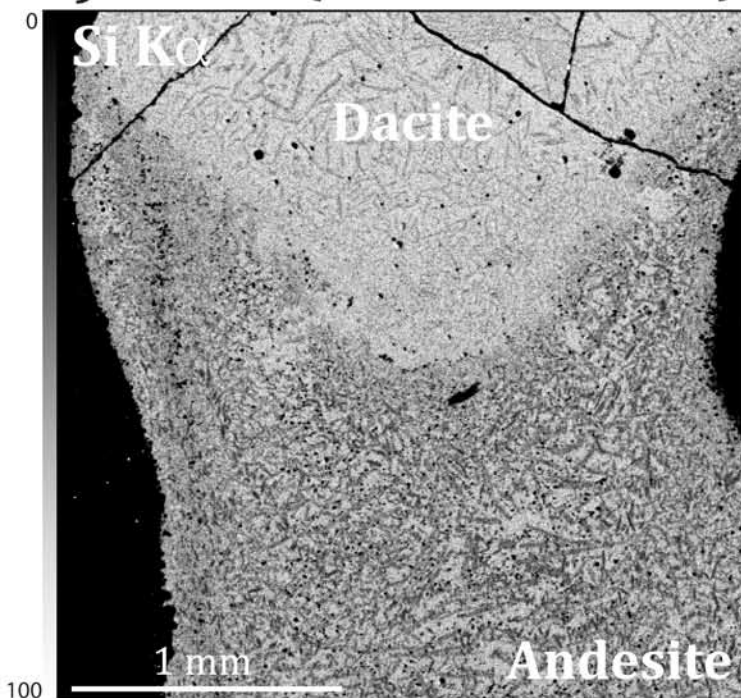


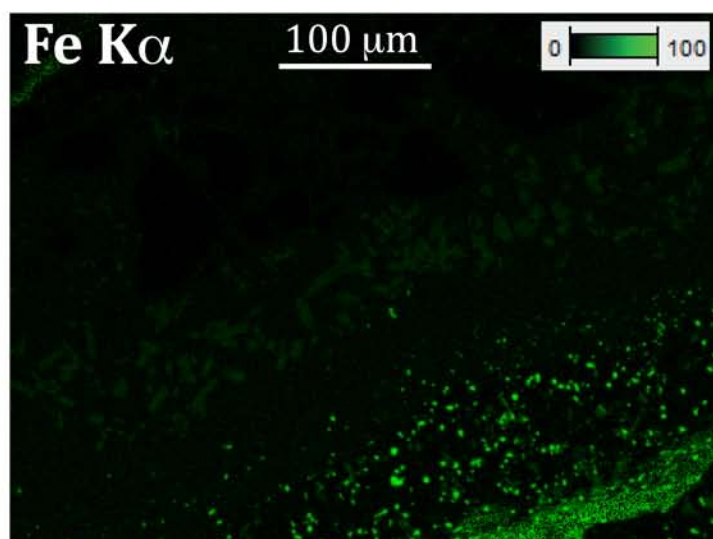
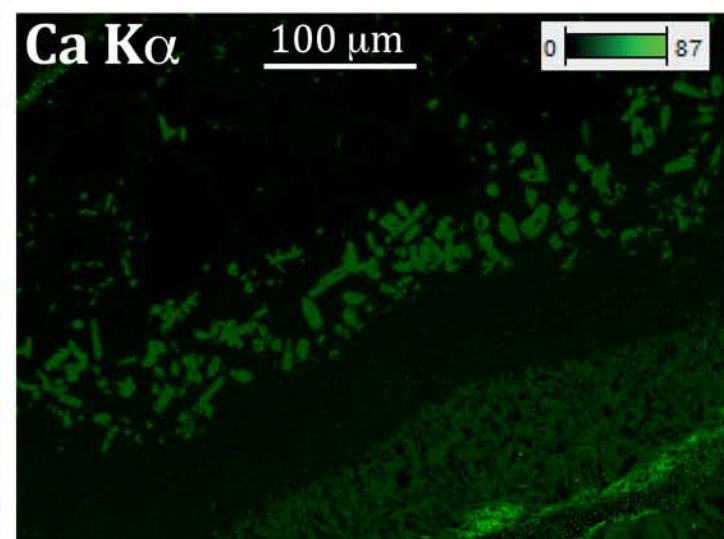
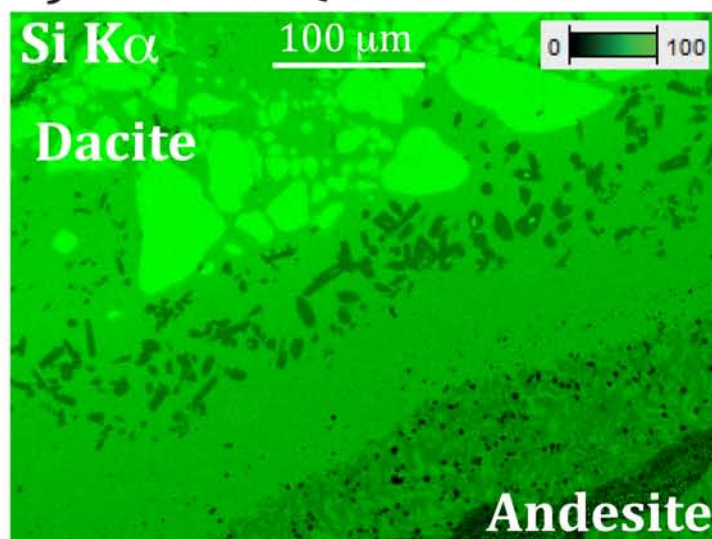


Figure 4

**A) F0-M (EPMA; 20 kV; 2 nA)**



**B) F70-M (SEM; 25 kV; 10 nA)**





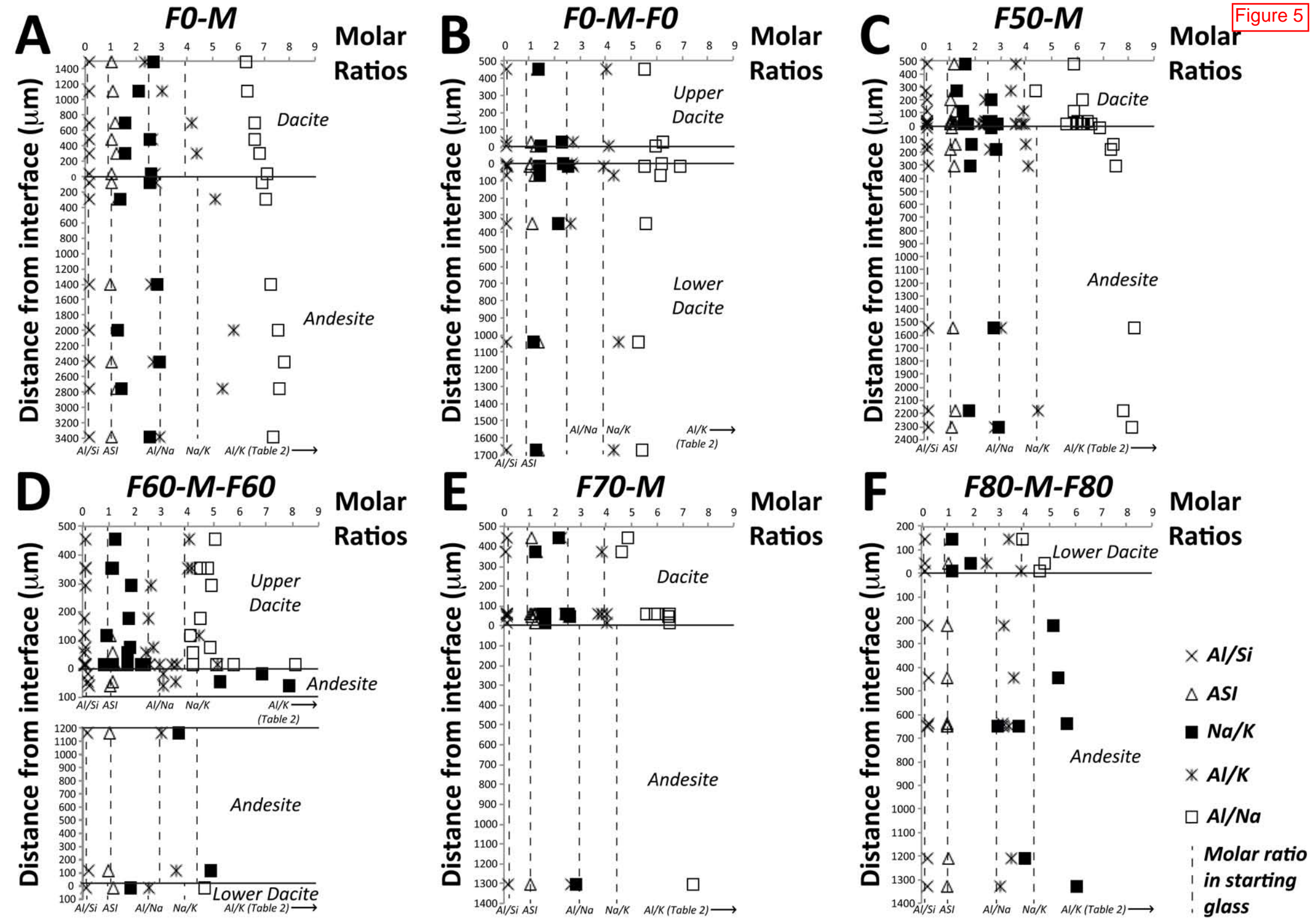


Figure 6

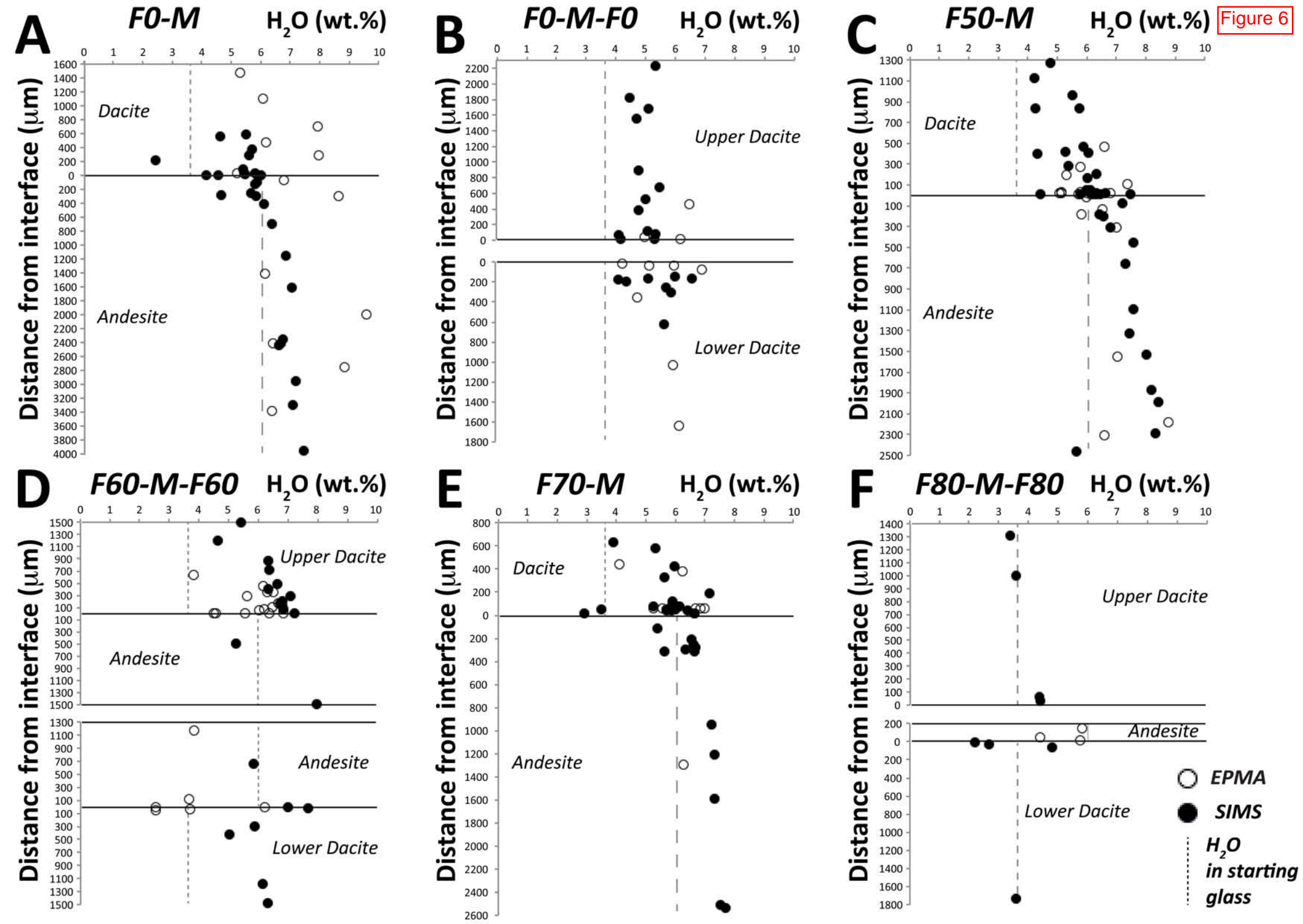
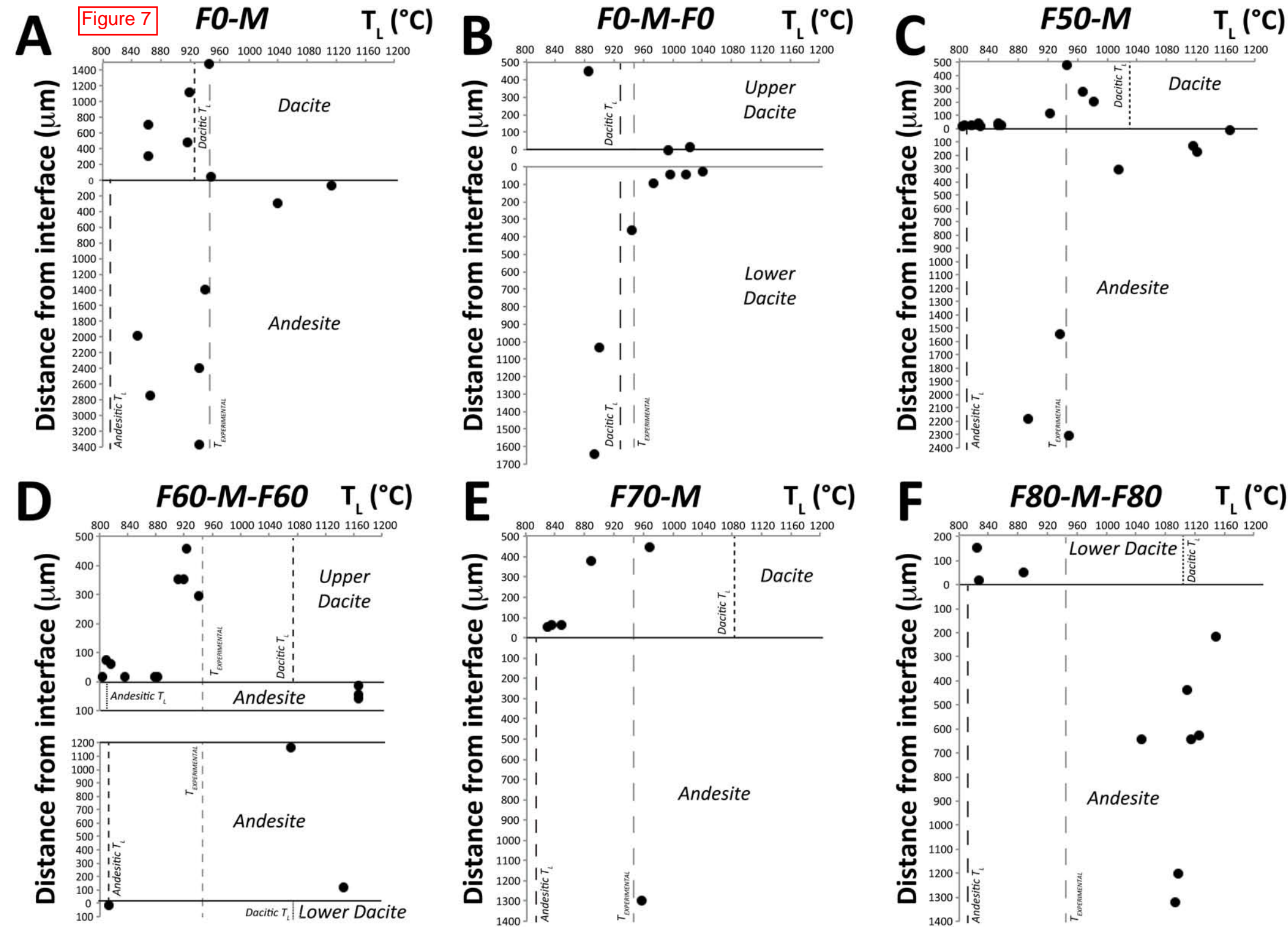


Figure 7





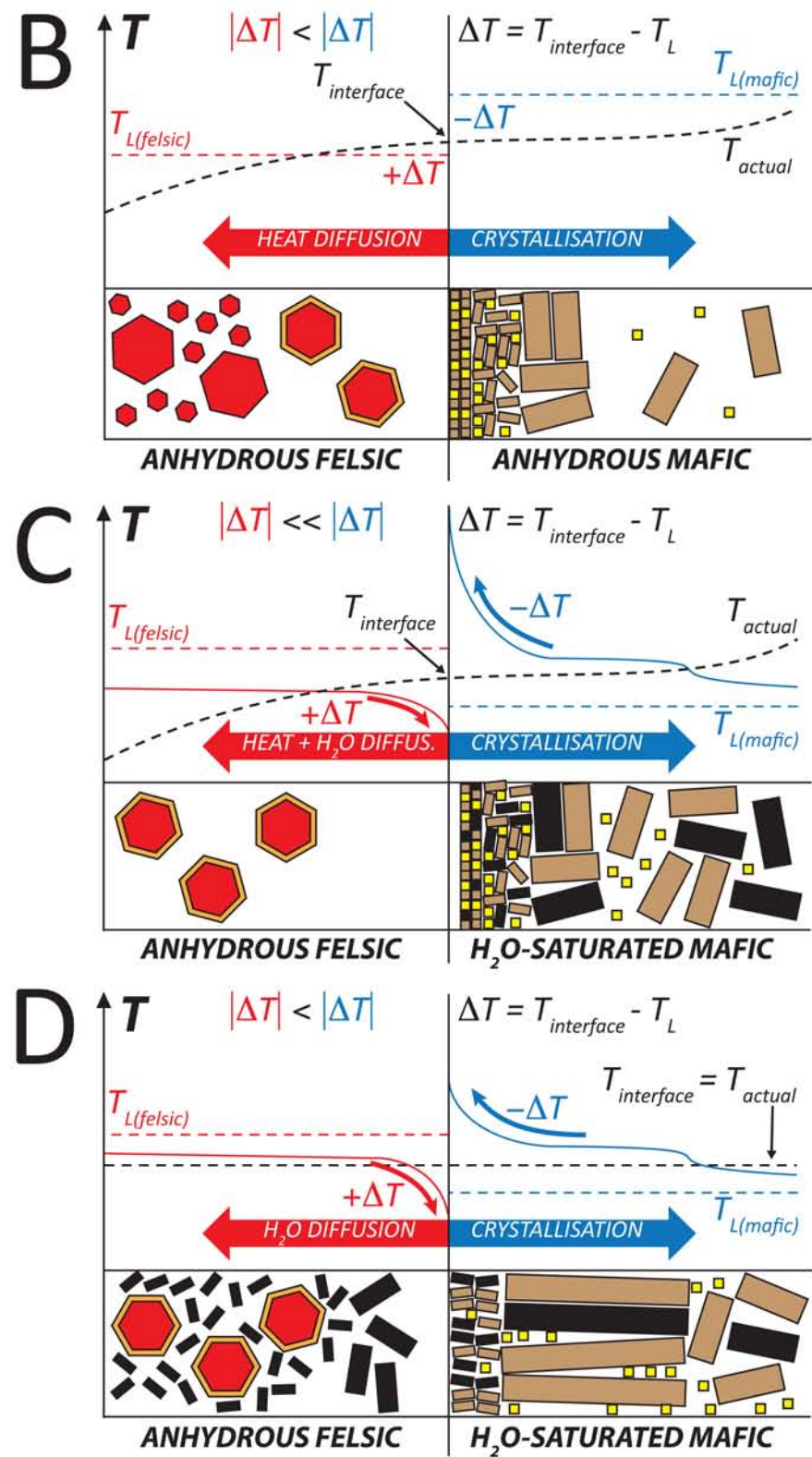
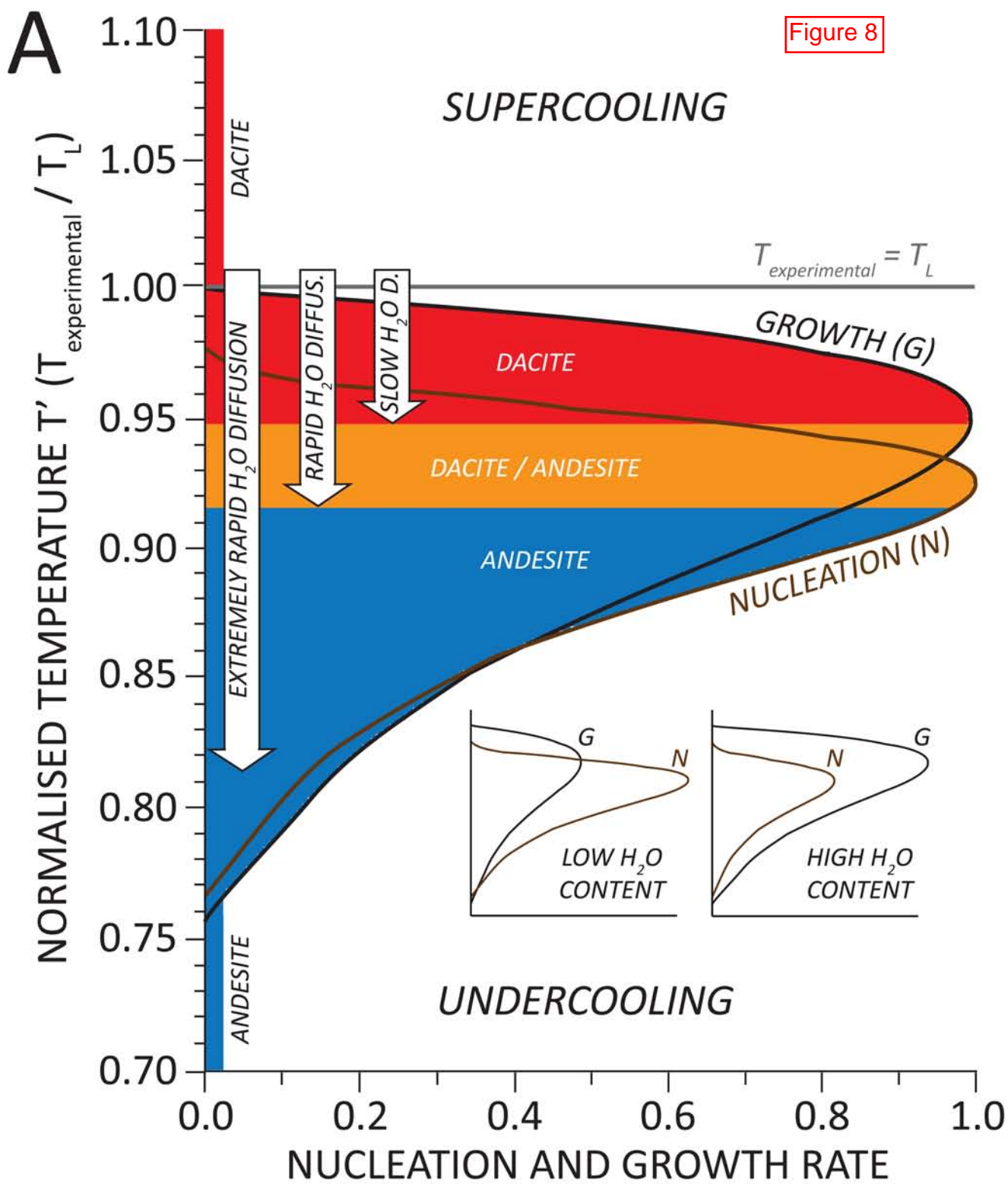


Table 1

<i>Experiment</i>	<i>Sample</i>	<i>a (mm)</i>	<i>l (mm)</i>	<i>V (mm<sup>3</sup>)</i>	<i>m (g)</i>	<i>ρ (kg/m<sup>3</sup>)</i>	<i>V<sub>felsic</sub> / V<sub>mafic</sub></i>	<i>m<sub>felsic</sub> / m<sub>mafic</sub></i>	<i>ρ<sub>felsic</sub> / ρ<sub>mafic</sub></i>	<i>T (°C)</i>	<i>P (kbar)</i>	<i>Duration (hours)</i>	<i>Glass</i>	<i>Hbl</i>	<i>Plag</i>	<i>Ox</i>	<i>Qz</i>	<i>Bubbles</i>
<i>F0_01(*)</i>	<i>F0</i>	2.99	2.48	17.41	0.0416	2389	-	-	-	950	4	1	-	-	-	-	-	-
<i>F0_02</i>	<i>F0</i>	-	-	-	0.0226	-	-	-	-	950	4	24	60	38	0	2	0	0
<i>F0_03</i>	<i>F0</i>	-	-	-	0.0190	-	-	-	-	950	4	24	68	31	0	1	0	0
<i>F80_01</i>	<i>F80</i>	-	-	-	0.0231	-	-	-	-	950	4	24	20	0	0	0	80	0
<i>F80_02</i>	<i>F80</i>	-	-	-	0.0116	-	-	-	-	950	4	24	20	0	0	0	80	0
<i>M_01(*)</i>	<i>M</i>	2.95	1.95	13.33	0.0391	2934	-	-	-	950	4	24	-	-	-	-	-	-
<i>M_02</i>	<i>M</i>	-	-	-	0.0122	-	-	-	-	950	4	24	50	19	30	1	0	0
<i>M_03</i>	<i>M</i>	-	-	-	0.0144	-	-	-	-	950	4	24	55	10	34	1	0	0
<i>M_cooling_01</i>	<i>M</i>	2.91	6.16	40.97	0.1053	2570	-	-	-	1000 to 950	4	0.004	70	18	10	1	0	1
<i>M_cooling_02</i>	<i>M</i>	2.92	3.68	24.64	0.0517	2098	-	-	-	1000 to 950	4	0.004	70	17	11	1	0	1
<i>M_cooling_03</i>	<i>M</i>	2.94	5.20	35.30	0.0858	2431	-	-	-	1000 to 950	4	0.83	5	20	70	4	0	1
<i>M_cooling_04</i>	<i>M</i>	2.95	5.80	39.64	0.0954	2407	-	-	-	1000 to 950	4	0.83	6	24	65	4	0	1
<i>F0-M</i>	<i>F0</i>	3.01	2.05	14.59	0.0348	2386	0.68	0.63	0.93	950	4	24	62	34	0	3	0	1
	<i>M</i>	2.94	3.18	21.59	0.0553	2562							55	14	26	4	0	1
<i>M-F0</i>	<i>M</i>	2.90	3.10	20.48	0.0530	2588	1.45	1.38	0.95	650	4	0.5	0	35	50	5	0	10
	<i>F0</i>	2.99	4.22	29.63	0.0732	2470							90	3	0	2	0	5
<i>F50-M</i>	<i>F50</i>	2.99	1.20	8.43	0.0187	2219	0.38	0.32	0.85	950	4	24	41	5	0	3	50	1
	<i>M</i>	2.92	3.34	22.37	0.0587	2624							49	20	27	2	0	2
<i>F60-M-F60</i>	<i>F60</i>	2.94	2.09	14.19	0.0333	2347	1.22	1.11	0.91	950	4	24	27	3	0	3	65	2
	<i>M</i>	2.93	3.43	23.13	0.0595	2573							36	23	35	3	0	3
	<i>F60</i>	2.92	2.10	14.06	0.0326	2318							29	3	0	3	63	2
<i>F70-M</i>	<i>F70</i>	2.97	2.06	14.27	0.0342	2396	0.58	0.54	0.93	950	4	24	20	7	0	2	70	1
	<i>M</i>	2.94	3.60	24.44	0.0629	2574							49	17	30	2	0	2
<i>F80-M-F80</i>	<i>F80</i>	3.00	2.22	15.69	0.0385	2453	1.33	1.25	0.94	950	4	24	9	7	0	3	80	1
	<i>M</i>	2.95	3.61	24.67	0.0646	2618							40	19	37	3	0	1
	<i>F80</i>	3.00	2.43	17.18	0.0425	2474							9	7	0	3	80	1
<i>F0-M-F0</i>	<i>F0</i>	3.00	2.52	17.81	0.0435	2442	2.29	2.14	0.93	950	4	168	69	27	0	3	0	1
	<i>M</i>	2.91	2.38	15.83	0.0415	2622							0	37	50	12	0	1
	<i>F0</i>	3.00	2.61	18.45	0.0452	2450							67	29	0	3	0	1
<i>F50-F0</i>	<i>F50</i>	4.20	2.92	40.45	-	-	1.14	-	-	950	4	22	41	2	0	1	55	1
	<i>F0</i>	3.88	2.99	35.35	0.0864	2444							55	38	0	6	0	1
<i>M-M</i>	<i>M</i>	4.03	3.01	38.39	0.0956	2490	1.01	1.00	0.99	950	4	25	55	10	18	10	0	7
	<i>M</i>	4.01	3.02	38.14	0.0958	2512							43	10	35	4	0	8
<i>F50-M</i>	<i>F50</i>	2.95	1.74	11.89	0.0276	2321	1.21	1.09	0.90	827	2 to 1	48	27	0	0	3	50	20
	<i>M</i>	2.92	1.47	9.84	0.0253	2570							8	20	46	4	0	22

Table 2

Sample Type	Sample Name	SiO <sub>2</sub>	TiO <sub>2</sub>	Al <sub>2</sub> O <sub>3</sub>	FeO <sub>TOT</sub>	MnO	MgO	CaO	Na <sub>2</sub> O	K <sub>2</sub> O	H <sub>2</sub> O	ASI	Na/K	Al/K	Al/Na	Al/Si
<i>Starting Materials</i>	<i>M</i>	60.96 (0.92)	0.84 (0.12)	22.11 (0.17)	2.94 (0.59)	0.22 (0.04)	0.18 (0.07)	6.59 (0.14)	4.54 (0.27)	1.62 (0.11)	6.03 (0.02)*	1.04 [0.32]	4.26 [0.09]	12.61 [0.07]	2.96 [0.06]	0.21 [0.02]
	<i>F0</i>	64.54 (0.33)	0.50 (0.04)	18.12 (0.20)	3.79 (0.12)	0.26 (0.02)	1.56 (0.08)	5.28 (0.08)	4.29 (0.06)	1.66 (0.04)	3.69 (0.02)*	0.98 [0.11]	3.93 [0.03]	10.08 [0.03]	2.57 [0.02]	0.17 [0.01]
<i>F0 / M</i>	<i>Plag in M</i>	52.17 (0.16)	-	28.90 (0.35)	0.82 (0.25)	-	0.13 (0.04)	13.75 (0.07)	4.00 (0.15)	0.25 (0.01)	-	-	-	-	-	-
	<i>Hbl in M</i>	43.14 (0.10)	2.37 (0.16)	12.92 (0.62)	12.43 (0.51)	0.60 (0.51)	14.28 (0.71)	11.48 (0.07)	2.29 (0.11)	0.49 (0.03)	2.86 (0.07)	-	-	-	-	-
	<i>Oxide in M</i>	-	3.21 (0.57)	4.91 (0.02)	85.23 (0.79)	1.60 (0.04)	5.05 (0.71)	-	-	-	-	-	-	-	-	-
<i>F50 / M</i>	<i>Plag in M</i>	53.43 (1.08)	0.18 (0.09)	28.49 (0.45)	1.65 (0.31)	0.04 (0.02)	0.23 (0.06)	11.54 (0.14)	4.12 (0.22)	0.27 (0.01)	-	-	-	-	-	-
	<i>Hbl in M</i>	43.00 (0.08)	2.15 (0.20)	13.79 (0.65)	13.14 (0.33)	0.60 (0.45)	13.27 (0.94)	11.38 (0.18)	2.12 (0.23)	0.55 (0.14)	2.76 (0.19)	-	-	-	-	-
	<i>Oxide in M</i>	-	5.21 (0.21)	1.81 (0.02)	87.46 (0.88)	1.45 (0.04)	4.07 (0.45)	-	-	-	-	-	-	-	-	-
	<i>Quartz in F50</i>	99.87 (0.01)	-	0.04 (0.01)	0.09 (0.01)	-	-	-	-	-	-	-	-	-	-	-
	<i>Hbl in F50</i>	46.55 (0.51)	2.51 (0.02)	11.46 (0.08)	10.36 (0.04)	0.77 (0.08)	10.22 (0.78)	13.48 (0.63)	3.87 (0.47)	0.78 (0.04)	2.74 (0.24)	-	-	-	-	-

Table 3

F0-M	F0												M		
Analysis Spot	1	2	3	4	5	6	7	8	9	10	11	12	13		
SiO <sub>2</sub>	68.44	68.53	68.64	67.67	68.32	67.32	66.98	67.78	66.60	66.53	65.64	66.50	66.13		
TiO <sub>2</sub>	0.54	0.52	0.53	0.57	0.56	0.55	0.63	0.68	0.67	0.65	0.60	0.63	0.61		
Al <sub>2</sub> O <sub>3</sub>	16.30	16.48	16.94	16.60	17.24	17.01	17.04	17.52	16.93	18.00	17.41	18.08	17.37		
FeO	2.90	3.21	3.09	3.12	3.18	3.13	3.30	3.25	3.16	3.56	3.38	3.50	3.32		
MnO	0.17	0.24	0.26	0.22	0.24	0.23	0.27	0.27	0.31	0.36	0.36	0.36	0.33		
MgO	1.35	1.50	1.58	1.64	1.55	1.58	1.63	1.66	1.73	1.92	1.91	1.89	1.73		
CaO	3.60	3.82	4.12	4.02	4.16	4.18	4.15	4.42	4.42	4.89	4.64	4.80	4.70		
Na <sub>2</sub> O	4.25	3.31	2.47	3.85	2.40	3.77	3.74	2.09	4.01	1.87	3.98	2.04	3.64		
K <sub>2</sub> O	2.39	2.39	2.36	2.32	2.34	2.21	2.27	2.30	2.16	2.20	2.06	2.19	2.18		
H <sub>2</sub> O	5.29	6.08	7.93	6.18	7.96	5.22	6.78	8.65	6.15	9.58	6.40	8.83	6.40		
ASI	1.01	1.10	1.20	1.03	1.23	1.05	1.06	1.26	1.00	1.25	1.01	1.25	1.03		
Na/K	2.70	2.10	1.59	2.52	1.56	2.59	2.51	1.38	2.82	1.30	2.93	1.41	2.54		
Al/K	6.29	6.36	6.62	6.62	6.81	7.10	6.94	7.05	6.57	7.57	7.79	7.61	7.36		
Al/Na	2.33	3.03	4.18	2.62	4.36	2.74	2.77	5.10	2.57	5.84	2.66	5.38	2.90		
Al/Si	0.14	0.14	0.15	0.14	0.15	0.15	0.15	0.15	0.15	0.16	0.16	0.16	0.15		
Distance (µm)	1482	1111	704	482	296	37	74	296	1407	2000	2407	2759	3389		

F0-M-F0	F0 <sub>bottom</sub>						F0 <sub>top</sub>			
Analysis Spot	1	2	3	4	5	6	7	8	9	10
SiO <sub>2</sub>	72.98	73.12	71.28	71.62	68.44	71.38	70.34	71.37	69.19	72.30
TiO <sub>2</sub>	0.52	0.57	0.60	0.51	0.49	0.50	0.27	0.47	0.54	0.56
Al <sub>2</sub> O <sub>3</sub>	15.67	15.47	15.60	15.00	17.25	15.30	16.46	16.35	16.23	15.67
FeO <sub>T</sub>	2.15	2.16	2.12	2.23	2.12	3.46	2.06	2.25	3.17	2.24
MnO	0.15	0.14	0.20	0.19	0.18	0.23	0.18	0.17	0.19	0.20
MgO	0.95	1.05	1.10	1.16	1.06	1.13	1.01	1.11	1.25	1.17
CaO	2.70	2.70	2.90	3.61	4.29	3.06	3.41	3.28	3.40	2.85
Na <sub>2</sub> O	2.20	2.08	3.61	2.25	3.85	2.37	3.76	2.41	3.61	2.37
K <sub>2</sub> O	2.66	2.71	2.58	2.41	2.31	2.55	2.46	2.53	2.40	2.63
H <sub>2</sub> O	6.19	5.99	4.78	6.96	5.17	6.02	4.28	6.14	4.95	6.44
ASI	1.37	1.37	1.11	1.24	1.25	1.10	1.20	1.10	1.31	1.31
Na/K	1.26	1.16	2.13	1.42	2.53	1.41	2.32	1.45	2.29	1.37
Al/K	5.45	5.27	5.58	6.14	6.91	5.54	6.19	5.97	6.26	5.50
Al/Na	4.33	4.53	2.62	4.33	2.73	3.92	2.67	4.12	2.73	4.02
Al/Si	0.13	0.12	0.13	0.13	0.15	0.13	0.14	0.13	0.14	0.13
Distance (µm)	1645	1032	355	81	32	32	15	15	32	452

F50-M	F50							
Analysis Spot	1	2	3	4	5	6	7	8
SiO <sub>2</sub>	74.27	72.29	73.98	72.81	72.62	73.40	74.15	72.17
TiO <sub>2</sub>	0.41	0.43	0.42	0.50	0.52	0.51	0.52	0.56
Al <sub>2</sub> O <sub>3</sub>	14.08	14.71	14.44	14.31	14.92	13.93	14.17	14.69
FeO <sub>T</sub>	2.54	2.59	2.56	2.64	2.31	2.59	2.44	2.35
MnO	0.13	0.15	0.17	0.17	0.21	0.17	0.18	0.19
MgO	0.84	0.85	0.81	0.95	1.05	0.88	0.92	1.07
CaO	3.08	3.01	3.07	2.95	3.37	2.82	3.02	3.00
Na <sub>2</sub> O	2.39	3.77	2.25	3.60	2.36	3.55	2.38	2.73
K <sub>2</sub> O	2.22	2.19	2.27	2.07	2.11	2.14	2.20	2.16
H <sub>2</sub> O	6.57	5.30	7.37	5.15	6.28	5.77	6.01	5.06
ASI	1.18	1.05	1.23	1.06	1.21	1.05	1.20	1.05
Na/K	1.64	2.62	1.50	2.64	1.70	2.52	1.65	2.66
Al/K	5.86	6.22	5.87	6.39	6.52	6.03	5.96	6.27
Al/Na	3.58	2.38	3.91	2.42	3.84	2.39	3.62	2.35
Al/Si	0.11	0.12	0.12	0.12	0.12	0.11	0.11	0.12
Distance (µm)	473	200	109	36	18	36	18	

F50-M-F50	F50 <sub>top</sub>												M
Analysis Spot	1	2	3	4	5	6	7	8	9	10	11	12	
SiO <sub>2</sub>	80.91	72.18	72.49	72.13	74.87	71.30	67.53	68.96	69.01	65.97	67.19	65.91	
TiO <sub>2</sub>	0.31	0.53	0.57	0.48	0.46	0.56	0.99	0.85	0.91	0.56	0.68	0.67	
Al <sub>2</sub> O <sub>3</sub>	10.09	14.63	14.57	14.44	13.91	15.17	15.76	15.99	16.41	17.90	17.79	17.88	
FeO <sub>T</sub>	2.03	2.38	2.64	2.77	2.42	2.80	6.01	3.09	3.28	3.47	3.19	3.09	
MnO	0.09	0.20	0.23	0.17	0.16	0.21	0.26	0.22	0.28	0.38	0.37	0.38	
MgO	0.69	1.11	1.41	0.98	0.87	1.02	1.22	1.32	1.45	1.82	1.81	1.83	
CaO	1.88	3.05	2.66	2.71	2.64	3.38	3.85	3.76	4.19	4.26	4.45	4.26	
Na <sub>2</sub> O	1.80	3.73	2.26	4.06	2.34	3.51	2.40	3.77	2.43	3.62	2.42	3.93	
K <sub>2</sub> O	2.14	2.19	2.15	2.16	2.30	2.04	1.96	2.02	2.02	2.01	2.11	2.03	
H <sub>2</sub> O	5.78	5.73	6.33	5.15	6.78	5.98	6.52	5.81	7.01	7.02	8.75	6.59	
ASI	1.16	1.04	1.15	1.04	1.25	1.07	1.21	1.05	1.19	1.13	1.24	1.09	
Na/K	1.28	2.59	1.60	2.86	1.55	2.61	1.86	2.84	1.83	2.73	1.75	2.94	
Al/K	4.35	6.17	6.27	6.18	5.59	6.87	7.42	7.33	7.49	8.22	7.81	8.13	
Al/Na	3.40	2.39	3.93	2.16	3.61	2.63	3.99	2.58	4.10	3.01	4.47	2.77	
Al/Si	0.07	0.12	0.12	0.12	0.11	0.13	0.14	0.14	0.14	0.16	0.16	0.16	
Distance (µm)	273	15	15	18	18	15	136	182	309	1546	2182	2309	

F60-M-F60	F60 <sub>top</sub>										M
Analysis Spot	1	2	3	4	5	6	7	8	9	10	11
SiO <sub>2</sub>	72.40	76.07	74.69	76.78	77.81	77.87	75.24	81.85	72.32	70.00	61.24
TiO <sub>2</sub>	0.40	0.46	0.37	0.44	0.28	0.26	0.38	0.29	0.42	0.32	0.19
Al <sub>2</sub> O <sub>3</sub>	14.84	12.87	13.05	12.90	12.16	11.91	13.11	10.02	13.72	16.47	22.92
FeO <sub>T</sub>	2.77	2.52	2.32	2.02	2.22	1.71	2.06	1.47	2.28	1.99	1.78
MnO	0.10	0.12	0.13	0.12	0.10	0.09	0.15	0.11	0.22	0.15	0.10
MgO	0.60	0.66	0.85	0.58	0.70	0.63	0.83	0.50	1.21	0.86	0.32
CaO	3.61	3.01	2.85	2.55	2.55	2.21	2.72	1.84	4.11	4.90	8.38
Na <sub>2</sub> O	3.22	1.92	3.03	1.89	1.84	2.86	1.97	1.69	3.25	2.93	4.50
K <sub>2</sub> O	2.04	2.35	2.46	2.50	2.51	2.45	2.50	2.21	2.21	1.88	1.00
H <sub>2</sub> O	3.81	6.15	5.61	6.27	6.50	6.67	6.19	5.54	6.83	4.49	2.54
ASI	1.06	1.15	1.02	1.23	1.17	1.05	1.05	1.18	0.90	1.04	0.97
Na/K	2.40	1.24	1.87	1.15	1.12	1.77	1.81	1.16	2.24	2.37	6.86
Al/K	6.73	5.06	4.90	4.77	4.48	4.49	4.85	4.20	5.75	8.11	21.21
Al/Na	2.80	4.08	2.62	4.14	4.02	2.53	2.68	3.60	2.57	3.42	3.09
Al/Si	0.12	0.10	0.10	0.10	0.09	0.09	0.10	0.07	0.11	0.14	0.22
Distance (µm)	647	456	294	353	353	177	74	15	15	15	15

F60-M-F60	F60 <sub>bottom</sub>										M
Analysis Spot	1	2	3	4	5	6	7	8	9	10	
SiO <sub>2</sub>	78.24	77.85	79.24	73.16	61.61	59.78	63.17	56.61	75.91		
TiO <sub>2</sub>	0.27	0.28	0.30	0.31	0.34	0.23	0.46	0.73	0.33		
Al <sub>2</sub> O <sub>3</sub>	10.75	10.73	11.10	11.71	22.47	24.07	19.93	13.73	13.57		
FeO <sub>T</sub>	2.42	2.21	2.05	3.50	2.15	1.65	2.60	6.85	1.70		
MnO	0.15	0.15	0.15	0.35	0.10	0.07	0.22	0.29	0.13		
MgO	1.31	1.25	1.21	2.49	0.40	0.24	1.75	2.66	0.47		
CaO	2.86	2.51	3.91	7.93	2.11	6.91	4.04	1.95	3.26		
Na <sub>2</sub> O	1.47	2.68	1.31	2.43	3.86	4.78	4.00	3.43	3.26		
K <sub>2</sub> O	2.42	2.36	2.44	2.13	1.11	0.92	1.65	1.06	2.68		
H <sub>2</sub> O	6.47	6.03	6.35	4.58	3.67	2.54	3.83	3.65	6.17		
ASI	1.03	0.93	1.20	1.01	1.02	1.01	1.02	1.15	1.1		



Table 4

F0-M		M																											
Analysis Spot		1	2	3	4	5	6	7	8	9	10	11	12	13	14	15	16	17	18	19	20	21	22	23	24	25	26	27	
FeO	0.29	0.30	0.30	0.30	0.17	0.31	0.35	0.38	0.31	0.30	0.29	0.25	0.60	0.39	0.35	0.36	0.37	0.35	0.37	0.34	0.35	0.33	0.34	0.35	0.32	0.32	0.32		
FeO <sub>2</sub>	1.61	2.33	1.67	1.73	1.17	1.64	1.58	1.56	1.83	2.32	1.75	1.40	4.61	1.70	1.71	1.73	1.75	1.74	1.93	2.02	1.95	1.81	1.95	2.04	1.66	1.62	1.58		
MgO	0.74	1.82	0.80	0.83	0.41	0.79	0.83	0.85	1.03	1.06	0.96	0.81	2.81	0.94	0.93	0.94	0.94	0.92	1.05	1.14	1.12	1.09	1.12	1.06	1.05	1.06	1.02		
CaO	2.64	4.32	2.58	2.63	1.55	2.61	2.58	2.61	3.05	4.75	3.44	4.23	4.86	2.81	2.79	2.84	2.86	2.79	3.08	3.22	3.24	3.22	3.31	3.21	3.18	3.27	2.99		
H <sub>2</sub> O	5.51	4.45	5.71	5.62	2.44	5.44	5.45	5.62	6.01	4.57	5.41	4.18	5.69	5.87	5.82	5.85	6.10	5.69	6.39	6.88	7.07	7.21	6.70	6.76	6.63	7.10	7.45		
Li	2.43	2.23	2.50	2.50	1.38	2.42	2.14	2.36	1.91	2.19	2.51	1.49	2.50	2.52	2.53	2.62	2.68	2.63	2.85	2.85	2.87	2.97	2.98	3.07	3.27	3.27			
B	11.48	11.48	12.43	12.43	6.80	16.27	21.00	24.53	15.10	12.74	14.13	12.95	27.39	28.21	19.45	20.85	22.21	18.79	29.08	36.89	39.36	40.56	38.77	39.05	39.23	38.23	38.43		
FeO <sub>2</sub> MgO	2.17	2.28	2.00	2.10	2.84	2.07	1.10	1.84	1.77	1.40	1.62	2.29	1.64	1.62	1.83	1.85	1.85	1.90	1.84	1.79	1.74	1.66	1.74	1.63	1.66	1.63	1.65		
Distance (μm)	593	568	370	296	222	37	19	37	15	10	61	65	113	52	494	172	230	194	161	307	161	145	629	2407	2355	2444	2296	2603	

F0-M-F0		M																										
Analysis Spot		1	2	3	4	5	6	7	8	9	10	11	12	13	14	15	16	17	18	19	20	21	22	23	24	25	26	27
FeO	0.23	0.26	0.19	0.14	0.22	0.27	0.31	0.11	0.13	0.22	0.30	0.21	0.26	0.22	0.19	0.22	0.32	0.23	0.22	0.32	0.30	0.24	0.31	0.31	0.30	0.36	0.33	
FeO <sub>2</sub>	1.14	1.33	1.08	1.08	1.11	1.13	1.20	1.03	1.10	1.09	1.24	1.16	1.43	1.50	2.32	1.18	1.43	1.22	1.32	1.32	1.20	1.09	1.11	1.11	1.11	1.11		
MgO	0.64	0.64	0.65	0.59	0.57	0.53	0.53	0.50	0.59	0.50	0.64	0.51	1.29	1.04	2.88	0.63	0.62	0.46	0.95	0.72	0.81	0.69	0.58	0.58	0.58	0.58		
CaO	1.95	1.92	2.97	1.88	2.49	1.90	1.96	2.83	1.88	3.77	2.05	3.53	2.13	4.46	5.50	3.94	1.97	3.69	3.43	1.92	1.97	1.87	1.88	1.88	1.88	1.88		
H <sub>2</sub> O	5.31	5.10	4.46	4.70	4.74	5.46	4.59	4.75	5.30	4.15	5.31	4.07	5.07	4.52	3.05	4.13	5.75	4.38	5.13	5.82	6.61	6.04	5.68	5.68	5.68	5.68		
Li	5.30	5.12	4.68	5.21	4.93	5.15	4.96	4.47	5.05	4.07	5.05	4.17	4.60	3.76	3.00	3.73	4.77	3.80	4.06	4.93	4.75	4.70	4.78	4.78	4.78	4.78		
B	15.03	22.73	12.15	14.52	13.00	16.24	16.15	12.71	25.44	22.36	25.37	20.85	26.49	41.33	26.19	25.02	32.68	19.15	22.32	29.58	34.47	25.84	19.81	24.07	24.07	24.07		
FeO <sub>2</sub> MgO	1.77	2.07	1.96	1.82	1.94	1.79	1.90	2.05	1.86	2.18	1.94	2.29	1.12	1.83	0.80	2.72	2.30	2.64	1.40	1.84	1.97	1.86	1.92	1.92	1.92	1.92		
Distance (μm)	2226	1677	1623	1548	887	677	516	387	15	10	81	65	113	52	484	177	258	194	161	307	161	145	629	2407	2355	2444	2296	2603

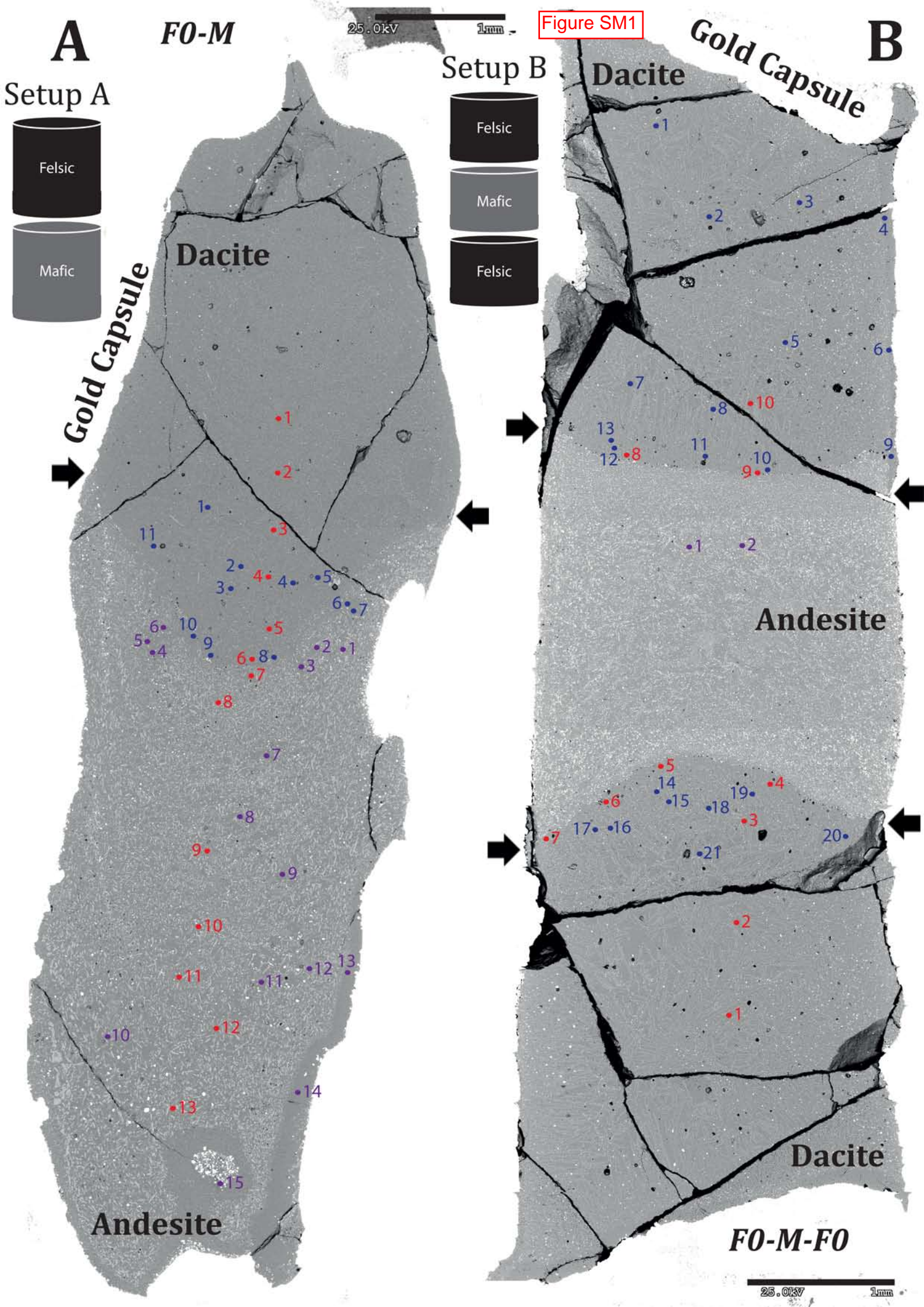
F0-M		M																																		
Analysis Spot		1	2	3	4	5	6	7	8	9	10	11	12	13	14	15	16	17	18	19	20	21	22	23	24	25	26	27	28	29	30	31	32	33	34	35
FeO	0.12	0.10	0.13	0.11	0.13	0.16	0.19	0.36	0.21	0.22	0.22	0.21	0.12	0.26	0.25	0.26	0.24	0.27	0.28	0.27	0.21	0.29	0.21	0.21	0.21	0.21	0.21	0.21	0.21	0.21	0.21	0.21	0.21	0.21	0.21	
FeO <sub>2</sub>	1.16	0.94	1.21	1.08	1.16	1.36	1.28	1.80	1.33	1.27	1.32	1.34	1.11	1.31	1.41	1.59	0.90	1.56	1.57	1.44	1.16	1.42	1.50	1.93	4.31	10.71	2.52	2.06	22.38	2.13	1.92	1.83	1.89	1.73	4.98	
MgO	0.52	0.30	0.41	0.35	0.60	0.38	0.43	0.84	0.47	0.49	0.46	0.48	0.22	0.55	0.51	0.59	0.47	0.67	0.64	0.58	0.33	0.59	0.57	0.57	0.97	1.15	0.94	0.98	2.44	1.29	1.05	1.18	1.13	1.05	4.89	
CaO	1.75	1.32	1.72	1.30	1.67	1.84	1.93	4.29	2.91	2.65	2.00	1.93	2.05	1.92	2.01	2.36	1.81	2.16	2.87	2.06	2.02	4.66	2.22	2.84	2.86	2.67	2.86	2.82	7.89	3.20	3.09	3.10	3.09	3.04	5.88	
H <sub>2</sub> O	4.78	4.24	4.22	5.50	5.74	5.29	5.87	4.32	3.37	6.30	6.01	6.06	5.77	6.46	6.16	6.99	7.48	6.26	6.62	6.31	6.12	4.41	7.19	6.42	6.79	6.96	7.56	7.29	7.96	7.44	8.01	8.16	8.22	8.31	5.65	
Li	1.80	2.78	2.08	2.21	2.38	3.38	3.64	3.07	3.38	3.72	3.56	3.65	2.58	3.76	3.71	4.00	3.46	3.65	3.73	3.77	2.65	4.16	4.16	4.16	4.61	4.42	4.41	4.73	4.66	4.66	4.66	4.62	4.78	4.79	4.75	
B	5.69	4.41	6.91	5.73	5.77	8.70	8.57	8.44	8.25	9.94	8.90	9.30	8.48	13.06	14.37	16.72	12.94	13.75	14.62	14.91	11.76	13.18	14.70	36.99	45.13	39.15	45.71	41.94	42.02	43.89	43.30	41.22	41.94	31.44		
FeO <sub>2</sub> MgO	2.11	3.12	2.85	3.04	1.92	3.62	2.97	2.27	2.83	2.60	2.88	3.00	4.99	2.38	2.76	2.69	0.90	2.31	2.46	2.58	3.46	1.80	2.86	2.22	4.45	9.28	2.15	2.10	6.17	1.65	1.62	1.65	1.67	1.65	1.02	
Distance (μm)	1273	1127	836	964	836	418	473	400	282	209	164	409	10	10	10	55	10	10	18	18	55	10	73	182	309	200	455	655	1091	1327	1527	1873	1982	2290	2464	

F0-M-F0		M																																		
Analysis Spot		1	2	3	4	5	6	7	8	9	10	11	12	13	14	15	16	17	18	19	20	21	22	23	24	25	26	27	28	29	30	31	32	33	34	35
FeO	0.16	0.14	0.17	0.15	0.14	0.19	0.17	0.14	0.14	0.15	0.14	0.14	0.67	0.21	0.77	0.15	0.15	0.13	0.25	0.10	0.11	0.11	0.11	0.11	0.11	0.11	0.11	0.11	0.11	0.11	0.11	0.11	0.11	0.11	0.11	
FeO <sub>2</sub>	1.77	1.35	1.11	1.11	1.04	1.52	0.92	0.99	1.15	0.90	1.00	1.28	5.40	0.94	7.75	0.71	0.71	0.76	1.42	1.01	0.81	0.81	0.81	0.81	0.81	0.81	0.81	0.81	0.81	0.81	0.81	0.81	0.81	0.81	0.81	
MgO	0.61	0.58	0.51	0.55	0.45	0.31	0.23	0.40	0.54	0.35	0.37	0.62	0.38	0.41	6.38	0.23	0.23	0.32	0.59	0.60	0.24	0.24	0.24	0.24	0.24	0.24	0.24	0.24	0.24	0.24	0.24	0.24	0.24	0.24	0.24	
CaO	1.75	1.32	1.72	1.30	1.67	1.84	1.93	4.29	2.91	2.65	2.00	1.93	2.05	1.92	2.01	2.36	1.81	2.16	2.87	2.06	2.02	4.66	2.22	2.84	2.86	2.67	2.86	2.82	7.89	3.20	3.09	3.10	3.09	3.04	5.88	
H <sub>2</sub> O	4.78	4.24	4.22	5.50	5.74	5.29	5.87	4.32	3.37	6.30	6.01	6.06	5.77	6.46	6.16	6.99	7.48	6.26	6.62	6.31	6.12	4.41	7.19	6.42	6.79	6.96	7.56	7.29	7.96	7.44	8.01	8.16	8.22	8.31	5.65	
Li	1.80	2.78	2.08	2.21	2.38	3.38	3.64	3.07	3.38	3.72	3.56	3.65	2.58	3.76	3.71	4.00	3.46	3.65	3.73	3.77	2.65	4.16	4.16	4.16	4.61	4.42	4.41	4.73	4.66	4.66	4.66	4.62	4.78	4.79	4.75	
B	5.69	4.41	6.91	5.73	5.77	8.70	8.57	8.44	8.25	9.94	8.90	9.30	8.48	13.06	14.37	16.72	12.94	13.75	14.62	14.91	11.76	13.18	14.70	36.99	45.13	39.15	45.71	41.94	42.02	43.89	43.30	41.22	41.94	31.44		
FeO <sub>2</sub> MgO	2.11	3.12	2.85	3.04	1.92	3.62	2.97	2.27	2.83	2.60	2.88	3.00	4.99	2.38	2.76	2.69	0.90	2.31	2.46	2.58	3.46	1.80	2.86	2.22	4.45	9.28	2.15	2.10	6.17	1.65	1.62	1.65	1.67	1.65	1.02	
Distance (μm)	1500	1206	882	721	412	600	294	260	132	10	177	74	485	1485	662	10	29	309	407	1191	1485															

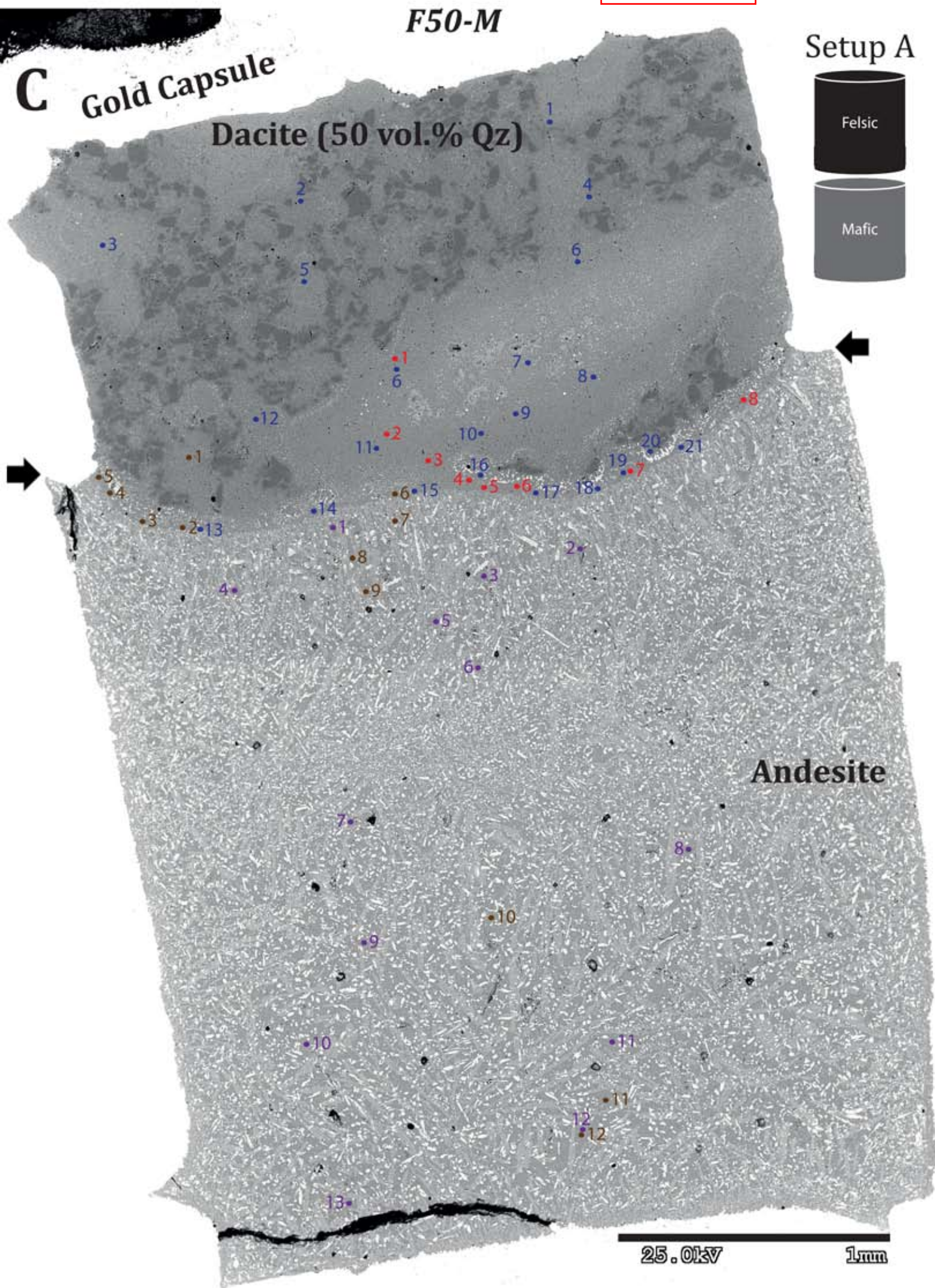
F0-M		M																																		
Analysis Spot		1	2	3	4	5	6	7	8	9	10	11	12	13	14	15	16	17	18	19	20	21	22	23	24	25	26	27	28	29	30	31	32	33	34	35
FeO	0.18	0.16	0.17	0.16	0.16	0.18	0.20	0.22	0.21	0.20	0.20	0.20	0.83	0.31	0.32	0.32	0.30	0.33	0.32	0.25	0.21	0.21	0.21	0.21	0.21	0.21	0.21	0.21	0.21	0.21	0.21	0.21	0.21	0.21	0.21	
FeO <sub>2</sub>	1.10	0.95	0.95	0.96	1.02	1.13	1.38	0.86	1.85	2.00	1.36	1.23	3.00	1.77	1.34	1.25	1.29	1.19	1.24	1.72	1.74	1.70	1.64													

Table SM 1

Element Profile 1				Element Profile 2			
Analysis Spot	SiO <sub>2</sub>	Al <sub>2</sub> O <sub>3</sub>	CaO	Analysis Spot	SiO <sub>2</sub>	Al <sub>2</sub> O <sub>3</sub>	CaO
1	89.85	3.65	0.55	1	75.82	9.07	1.52
2	98.14	0.20	0.13	2	76.05	9.77	1.41
3	98.14	0.20	0.13	3	73.93	10.81	1.20
4	80.15	8.03	1.18	4	76.73	10.05	1.42
5	79.96	7.84	1.33	5	77.44	9.21	1.41
6	98.14	0.20	0.13	6	77.28	9.79	1.25
7	98.14	0.20	0.13	7	76.31	9.53	1.40
8	80.47	9.07	1.49	8	76.79	9.93	1.19
9	77.32	9.65	1.12	9	76.26	10.07	1.42
10	78.64	8.37	1.25	10	74.99	9.48	1.29
11	79.03	8.24	1.46	11	75.40	8.88	1.20
12	85.80	5.32	1.04	12	75.77	9.67	1.68
13	89.49	4.89	0.89	13	76.11	8.79	1.49
14	97.08	0.32	0.11	14	75.81	10.47	1.22
15	76.19	9.45	1.36	15	75.42	8.45	1.32
16	72.99	9.43	1.35	16	74.75	10.13	1.44
17	76.37	7.62	1.29	17	78.20	8.00	1.33
18	73.24	9.40	1.28	18	78.22	9.62	1.55
19	77.58	9.78	1.15	19	79.13	9.85	1.45
20	75.42	9.88	1.20	20	78.04	9.29	1.25
21	76.74	8.94	1.23	21	74.89	9.31	1.39
22	83.07	6.88	0.96	22	78.47	9.91	1.46
23	98.65	0.36	0.04	23	76.14	8.94	1.48
24	98.14	0.20	0.13	24	74.08	8.90	1.42
25	75.53	9.75	1.31	25	78.15	9.30	1.28
26	77.47	8.57	1.29	26	77.38	8.72	1.67
27	77.15	9.64	1.34	27	78.32	9.74	1.36
28	79.32	9.80	1.43	28	75.70	9.76	1.44
29	75.85	8.63	1.48	29	78.14	10.22	1.48
30	76.01	8.56	1.11	30	77.84	10.19	1.32
31	79.71	8.92	1.16	31	73.76	9.03	1.40
32	77.10	9.98	1.25	32	76.04	9.51	1.47
33	80.62	7.61	1.35	33	76.92	10.33	1.31
34	96.94	1.03	0.34	34	75.55	10.94	1.35
35	98.14	0.20	0.13	35	73.30	8.61	1.65
36	76.36	9.62	1.13	36	74.61	9.45	1.51
37	74.33	9.91	1.33	37	74.80	9.23	1.46
38	76.64	9.58	1.39	38	78.07	9.46	1.52
39	75.27	10.62	1.10	39	74.96	9.06	1.44
40	76.90	10.40	1.40	40	75.80	9.68	1.31
41	75.84	9.04	1.38	41	76.25	8.97	1.20
42	76.40	8.44	1.18	42	76.61	8.89	1.25
43	78.34	9.02	1.36	43	73.99	9.32	1.30
44	74.26	9.23	1.11	44	75.65	8.85	1.40
45	76.18	9.33	1.26	45	79.22	10.48	1.29
46	77.13	9.37	1.24	46	74.23	9.15	1.21
47	79.43	7.25	1.06	47	78.22	8.82	1.31
48	73.69	9.01	1.50	48	76.45	9.10	1.32
49	76.85	9.81	1.42	49	78.71	9.26	1.23
50	77.38	10.13	1.47	50	76.71	9.03	1.21
51	74.34	10.17	1.29	51	75.67	10.29	1.50
52	75.44	8.78	1.25	52	77.18	9.55	1.25
53	75.30	9.52	1.43	53	75.05	9.68	1.39
54	77.58	9.46	1.24	54	77.28	8.91	1.32
55	77.39	9.69	1.16	55	78.17	9.71	1.50
56	79.14	9.32	1.43	56	75.61	9.61	1.53
57	77.14	9.85	1.27	57	75.69	9.18	1.59
58	77.27	7.98	1.34	58	76.08	10.06	1.14
59	75.75	10.28	1.34	59	78.44	9.68	1.25
60	75.02	8.72	1.72	60	79.14	8.44	1.31
61	75.49	9.88	1.62	61	76.88	10.02	1.30
62	75.63	8.50	1.59	62	76.90	11.13	1.27
63	74.98	9.64	1.35	63	77.99	9.37	1.18
64	75.10	8.91	1.52	64	77.29	8.60	1.28
65	75.03	9.68	1.27	65	78.01	10.34	1.10
66	77.62	9.31	1.24	66	75.64	9.71	1.19
67	75.25	8.67	1.44	67	76.69	9.62	1.35
68	79.35	8.80	1.44	68	78.76	9.23	1.47
69	74.64	9.35	1.41	69	77.09	8.35	0.96
70	74.39	10.59	1.38	70	77.30	9.23	1.47
71	75.72	9.95	1.42	71	75.34	9.23	1.34
72	76.64	8.81	1.29	72	77.92	9.56	1.44
73	75.48	10.33	1.38	73	77.22	9.27	1.19
74	76.76	9.88	1.42	74	75.75	9.65	1.34
75	74.20	9.24	1.38	75	76.72	9.46	1.24
76	80.24	8.65	1.45	76	77.43	8.07	1.45
77	76.80	9.81	1.32	77	78.15	9.31	1.51
78	76.56	8.13	1.48	78	75.27	9.47	1.17
79	75.45	8.56	1.43	79	74.71	10.30	1.32
80	75.32	10.42	1.12	80	76.21	9.70	1.22
81	73.24	8.60	1.64	81	74.94	9.50	1.38
82	74.70	10.08	1.30	82	75.14	9.46	1.44
83	76.76	9.75	1.49	83	77.06	9.34	1.20
84	74.75	9.60	1.47	84	76.70	7.34	1.40
85	74.39	8.92	1.37	85	75.42	8.67	1.29
86	77.44	9.47	1.02	86	77.06	9.32	1.45
87	73.33	9.41	1.38	87	76.25	9.88	1.34
88	76.69	9.56	1.62	88	76.30	8.20	1.10
89	74.12	10.30	1.29	89	77.75	8.46	1.03
90	75.76	10.63	1.38	90	94.07	3.30	0.62
91	76.36	8.80	1.37	91	98.14	0.20	0.13
92	79.96	10.35	1.42	92	98.14	0.20	0.13
93	77.01	10.23	1.32	93	98.14	0.20	0.13
94	76.47	9.80	1.38	94	90.41	4.92	0.52
				95	77.66	7.67	1.16
				96	79.94	9.79	1.37
				97	78.42	9.02	1.20
				98	77.91	10.79	1.57
				99	75.37	9.28	1.15
				100	77.60	9.53	1.10
				101	75.90	8.92	1.39
				102	75.16	8.38	1.80
				103	78.77	10.12	1.09
				104	78.21	8.05	0.93
				105	76.23	9.35	1.26
				106	75.28	7.85	1.10
				107	76.84	8.92	1.25
				108	89.44	3.79	0.80
				109	98.14	0.20	0.13
				110	98.14	0.20	0.13
				111	98.14	0.20	0.13
				112	98.14	0.20	0.13
				113	98.14	0.20	0.13
				114	98.14	0.20	0.13
				115	95.39	2.83	0.29
				116	74.49	9.07	1.15
				117	75.26	8.48	1.32
				118	76.42	9.59	1.39
				119	76.47	8.29	1.31
				120	98.14	0.20	0.13
				121	98.14	0.20	0.13
				122	99.97	0.06	0.07
				123	98.14	0.20	0.13
				124	98.14	0.20	0.13
				125	98.14	0.20	0.13





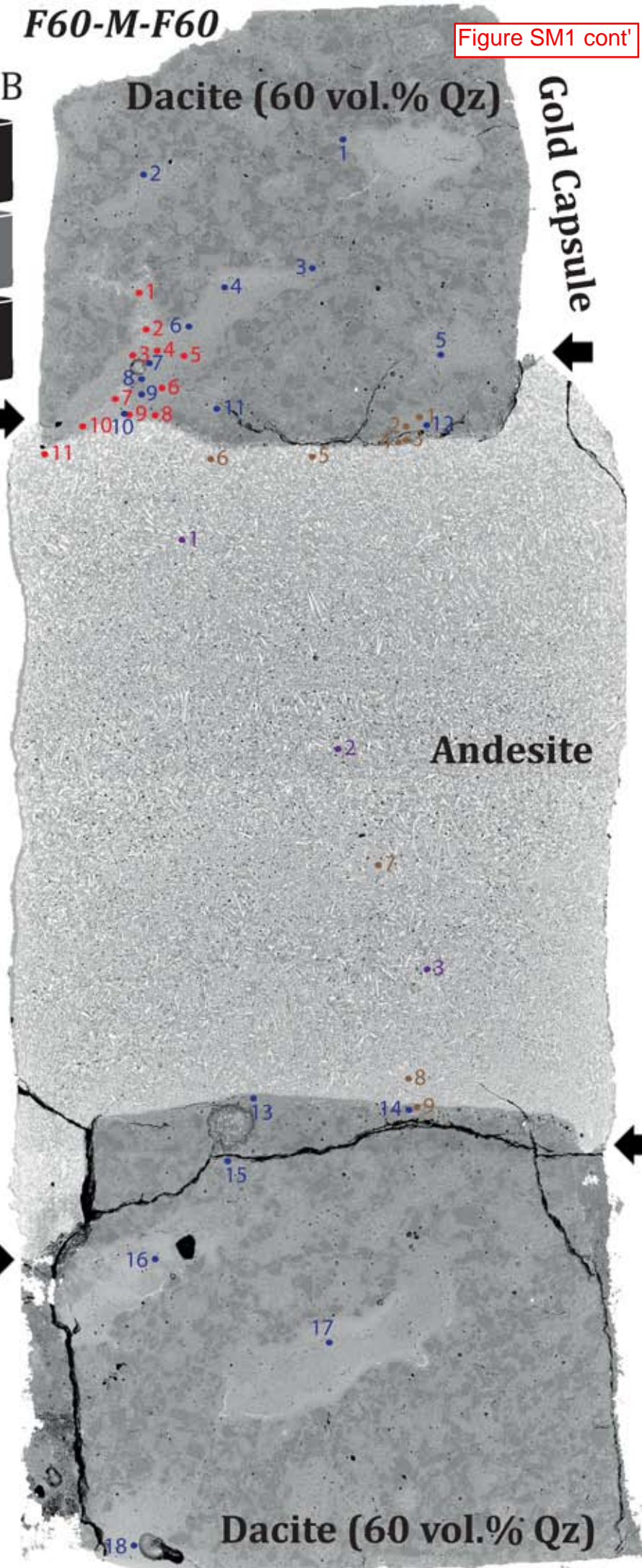




**D****F60-M-F60**

Figure SM1 cont'

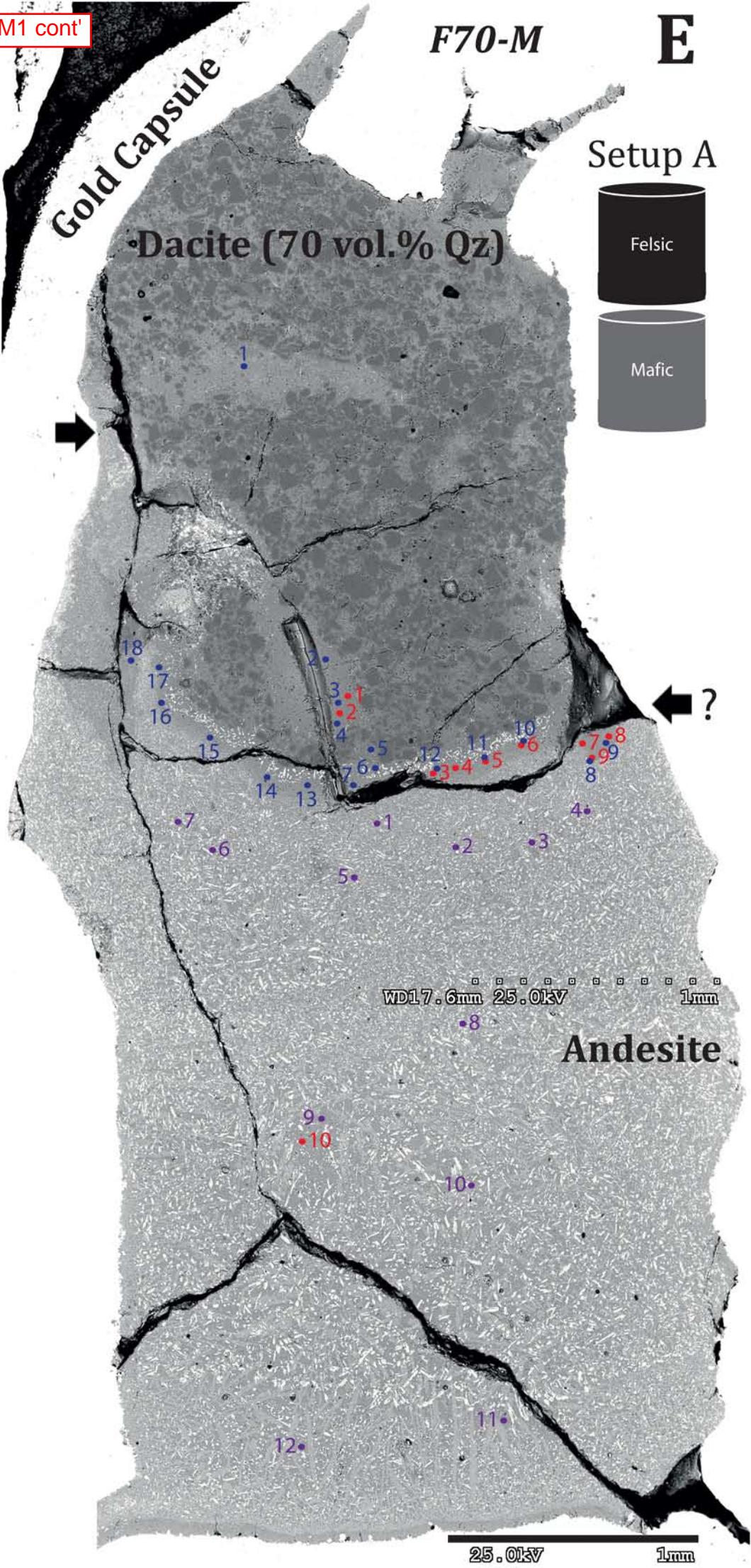
Setup B

**Gold Capsule**



F70-M

E

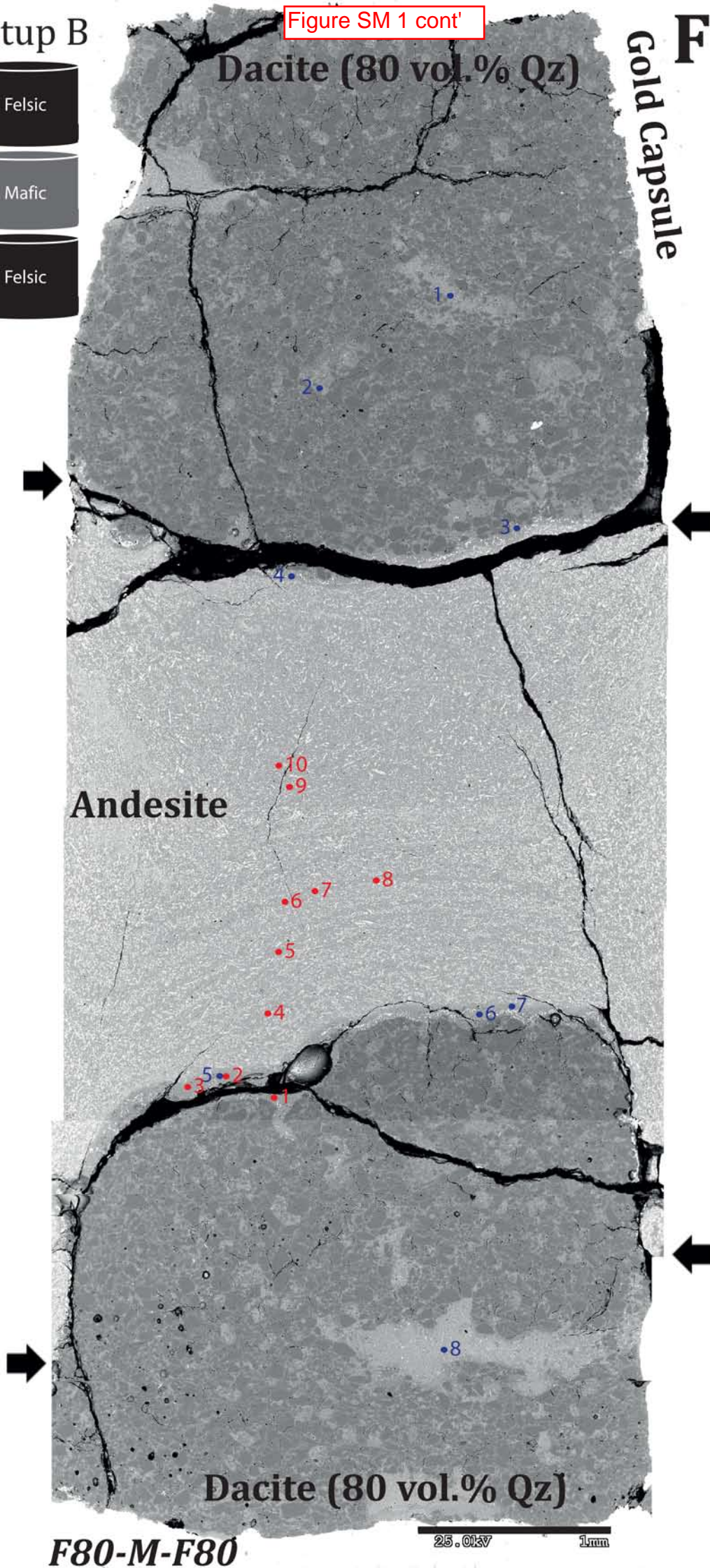




Setup B

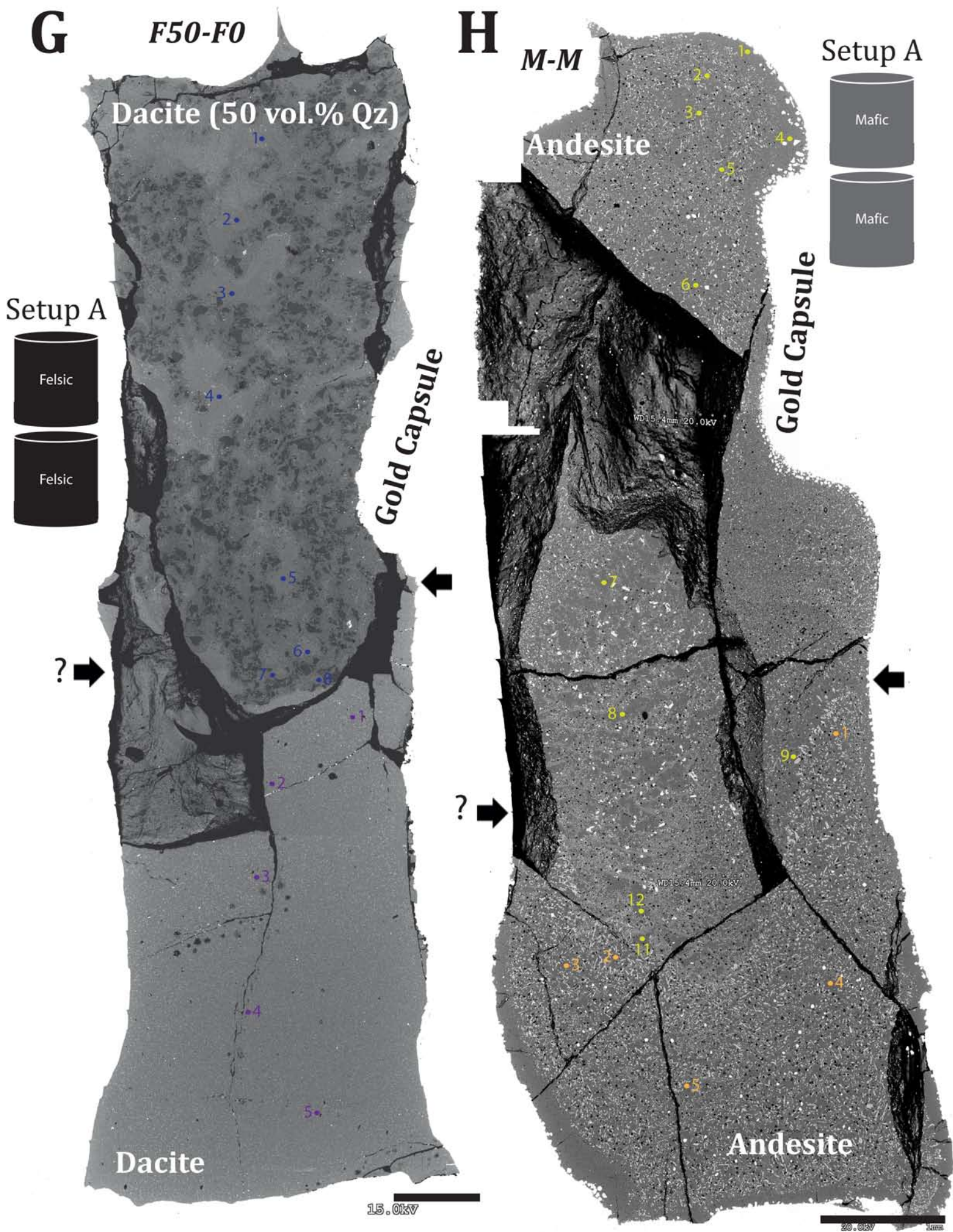


**F**  
Gold Capsule



**F80-M-F80**

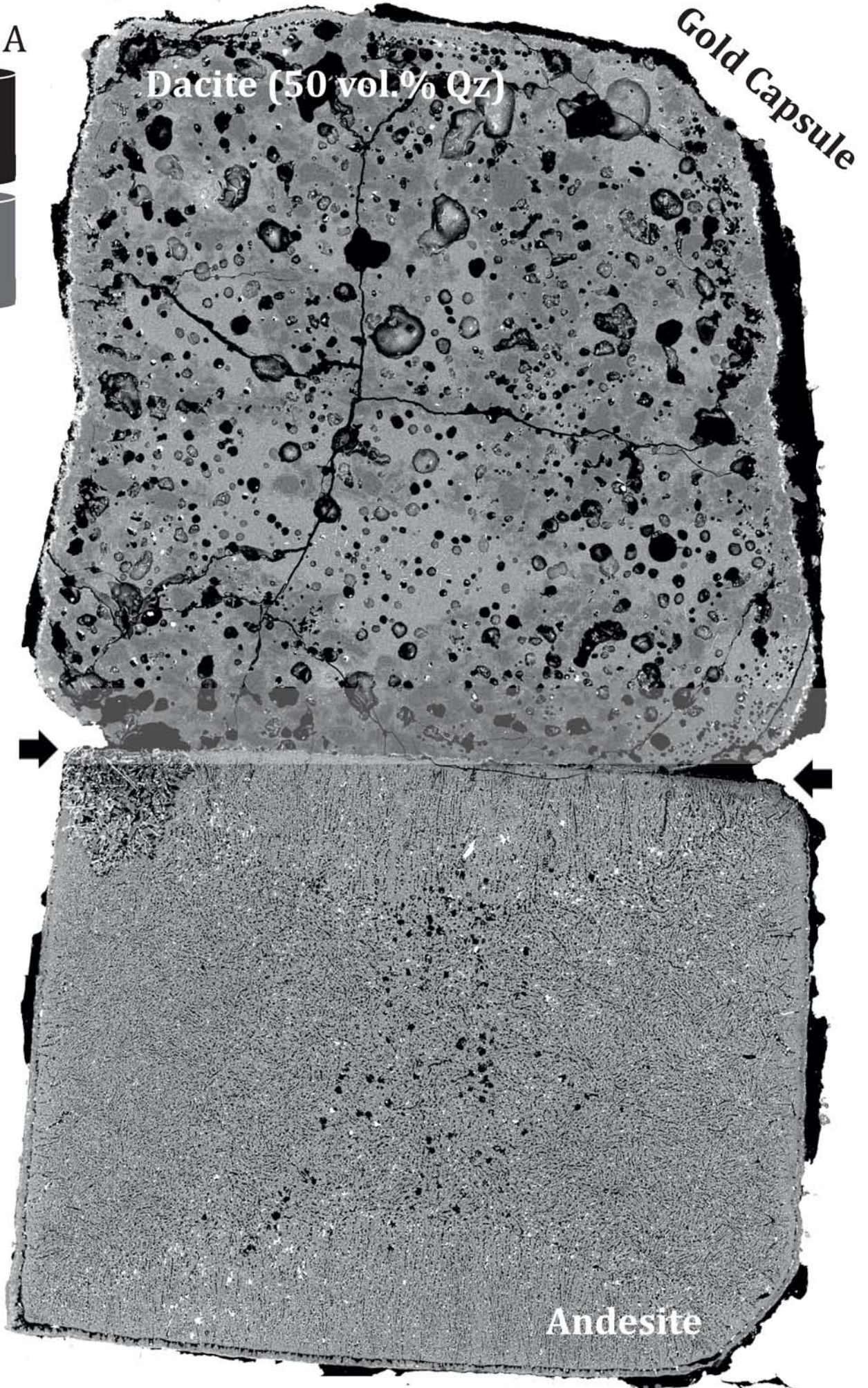






*F50-M*

Setup A

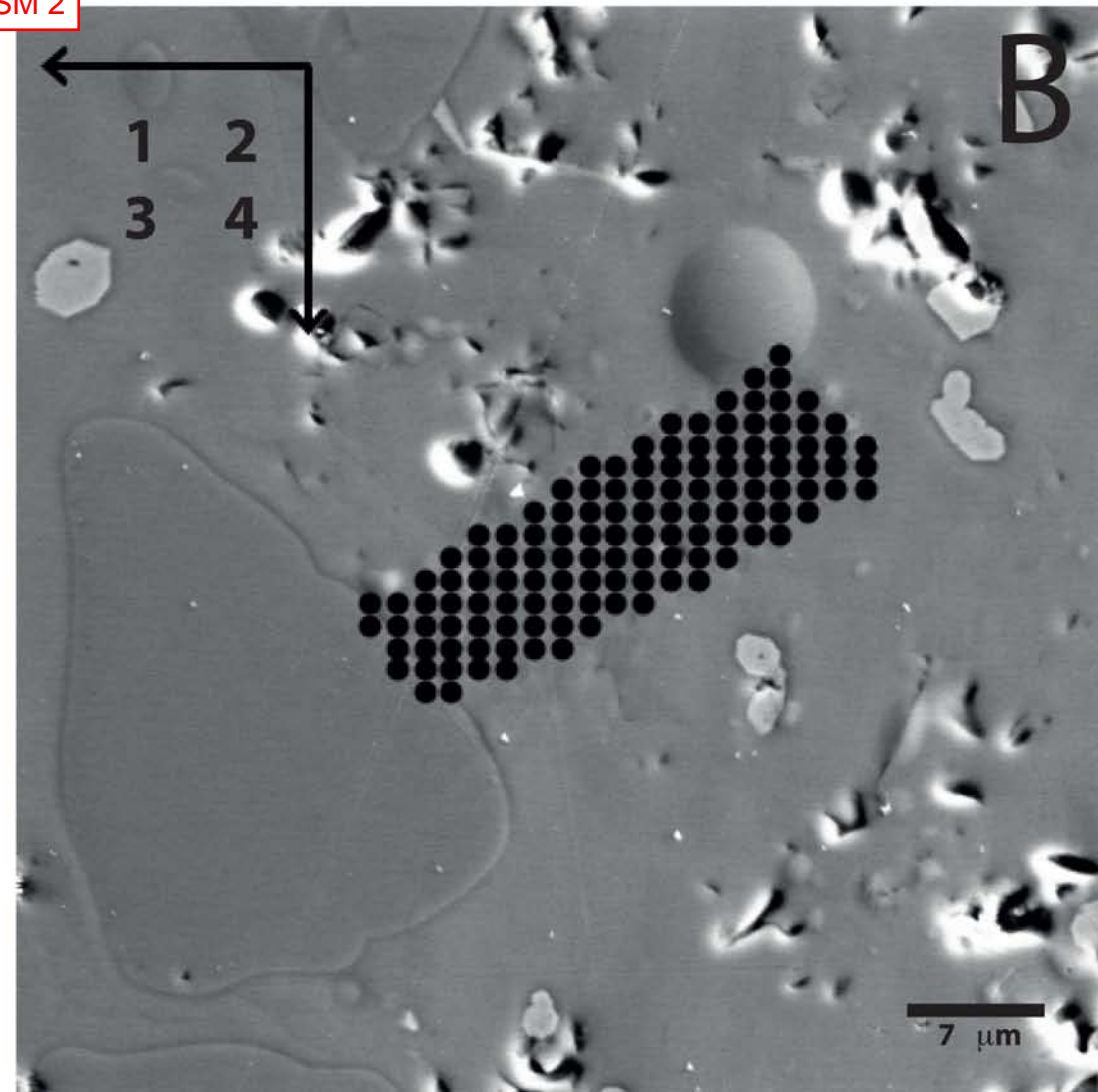
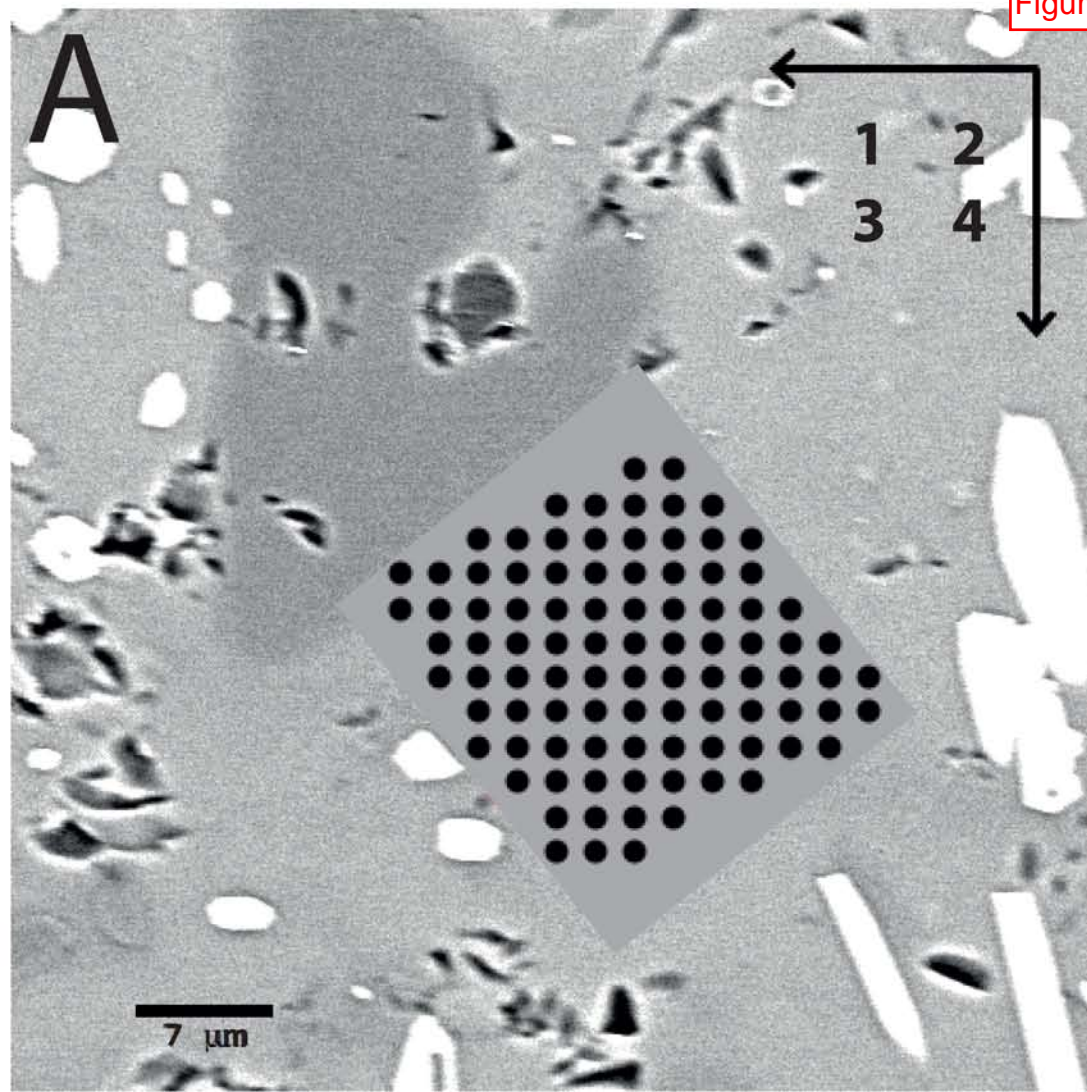


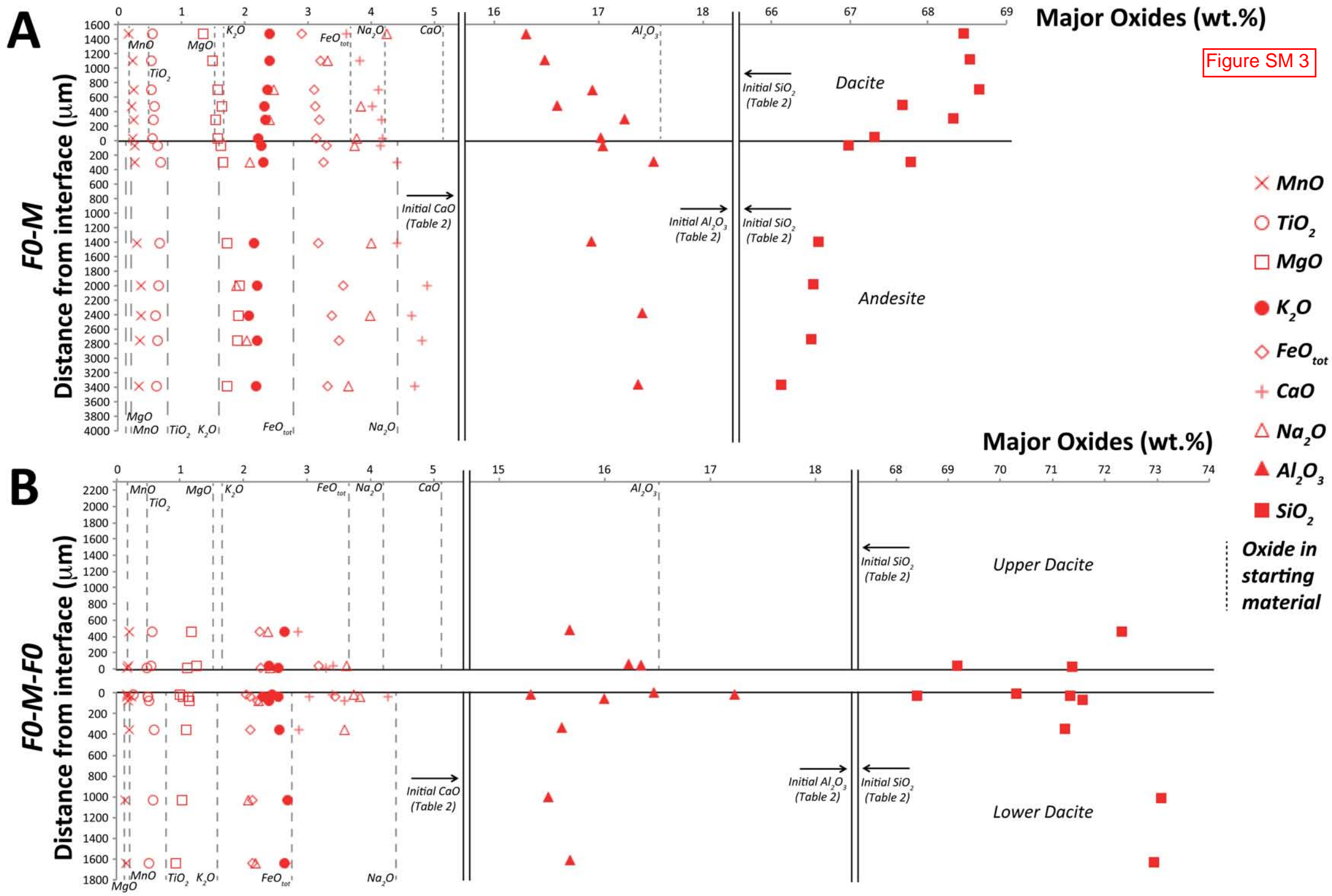
25.01kV

1mm



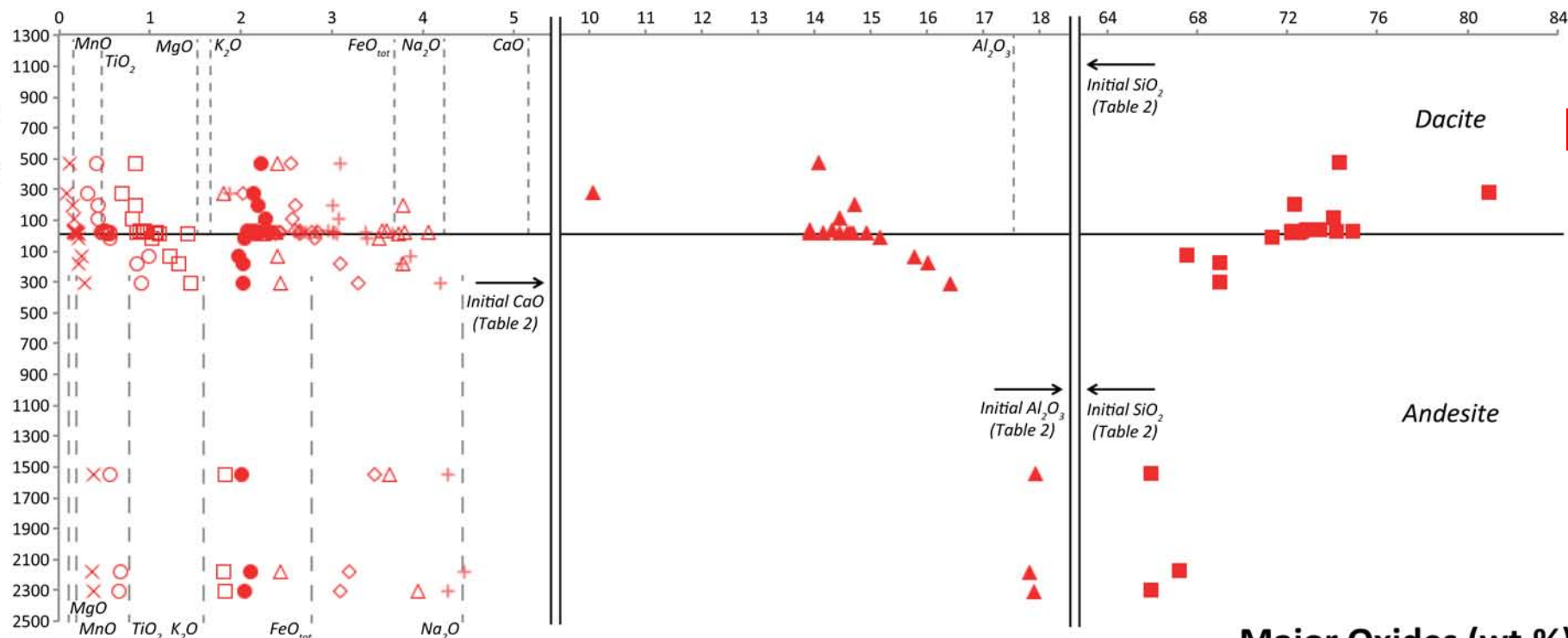
Figure SM 2





C

F50-M

Distance from interface ( $\mu\text{m}$ )

Major Oxides (wt.%)

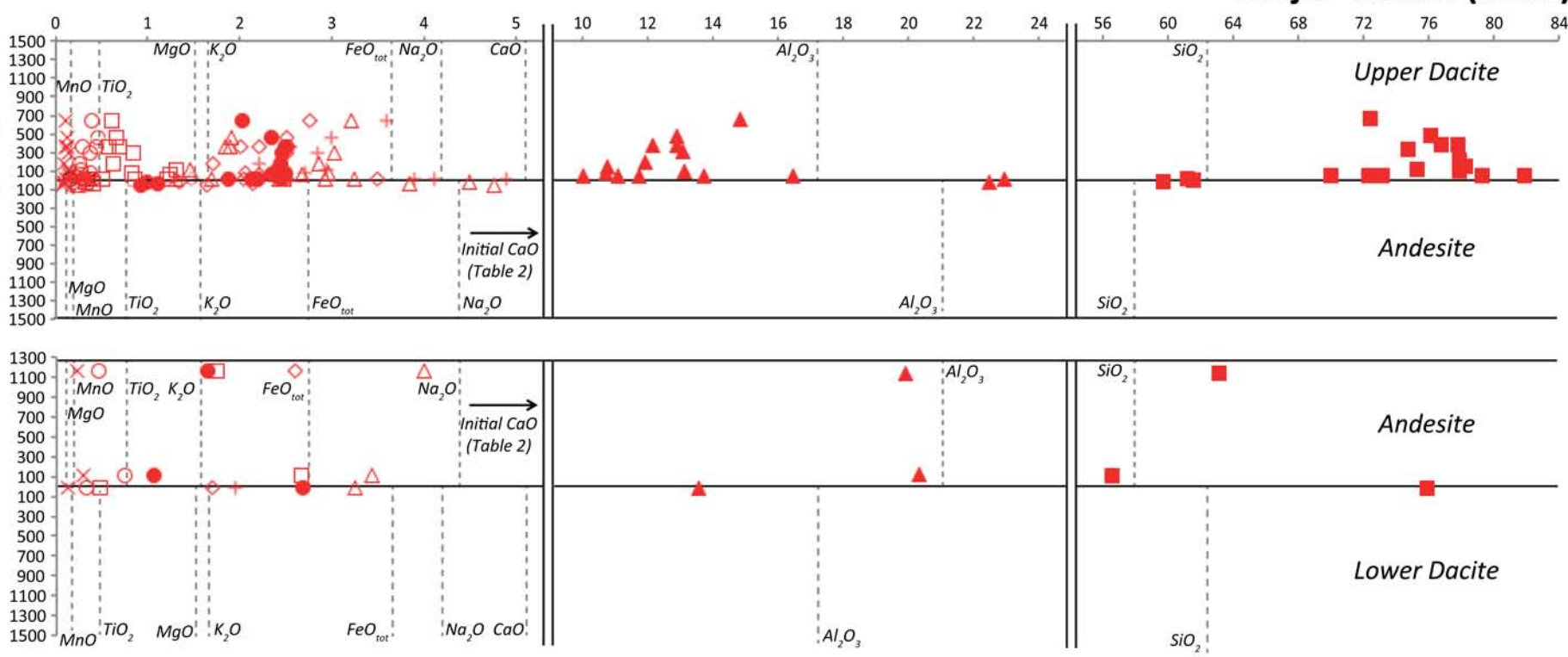
Figure SM 3 cont'

 $\times$  MnO $\circ$  TiO<sub>2</sub> $\square$  MgO $\bullet$  K<sub>2</sub>O $\diamond$  FeO<sub>tot</sub> $+$  CaO $\triangle$  Na<sub>2</sub>O $\blacktriangle$  Al<sub>2</sub>O<sub>3</sub> $\blacksquare$  SiO<sub>2</sub>

Oxide in starting material

D

F60-M-F60

Distance from interface ( $\mu\text{m}$ )

Major Oxides (wt.%)



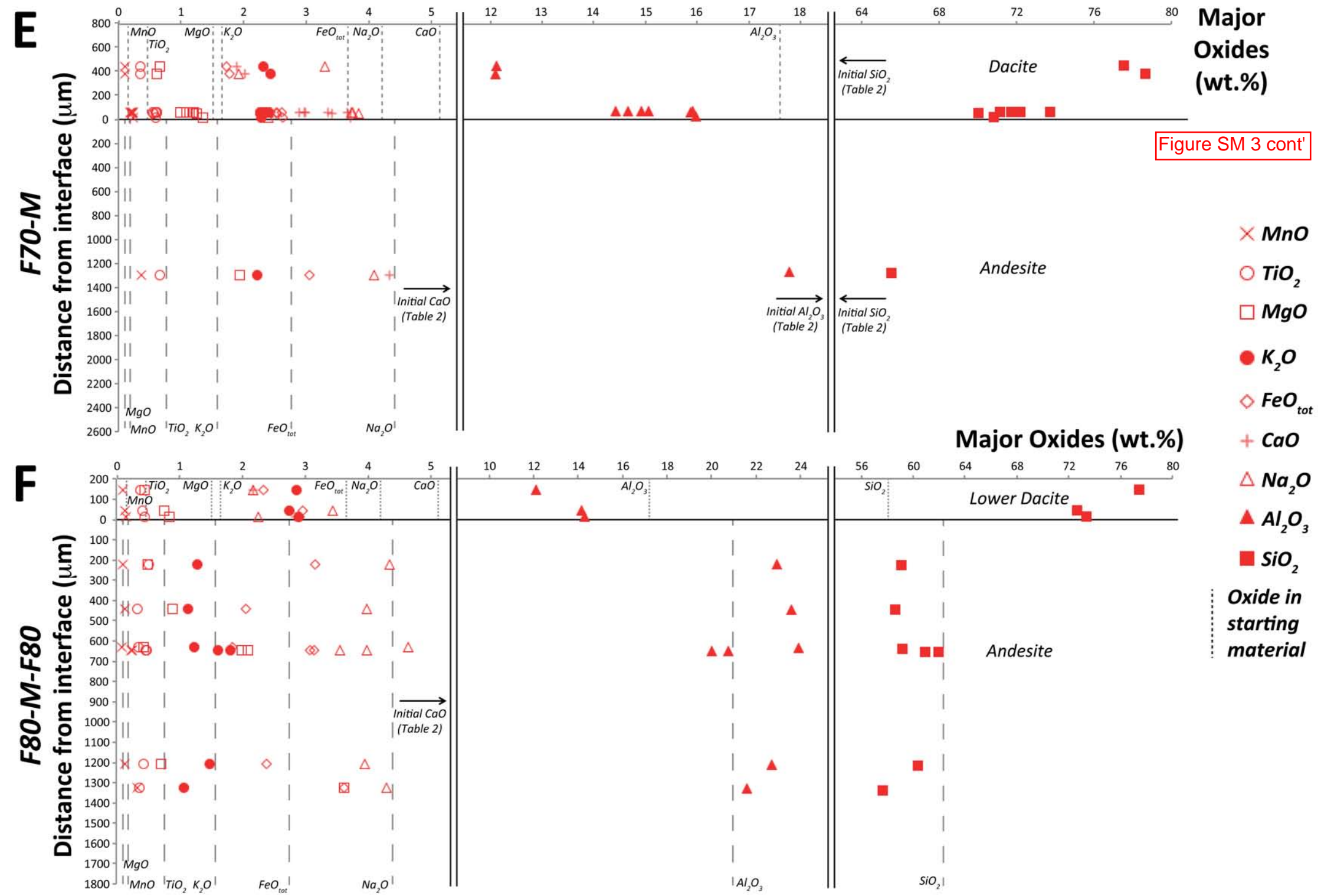


Figure SM 4

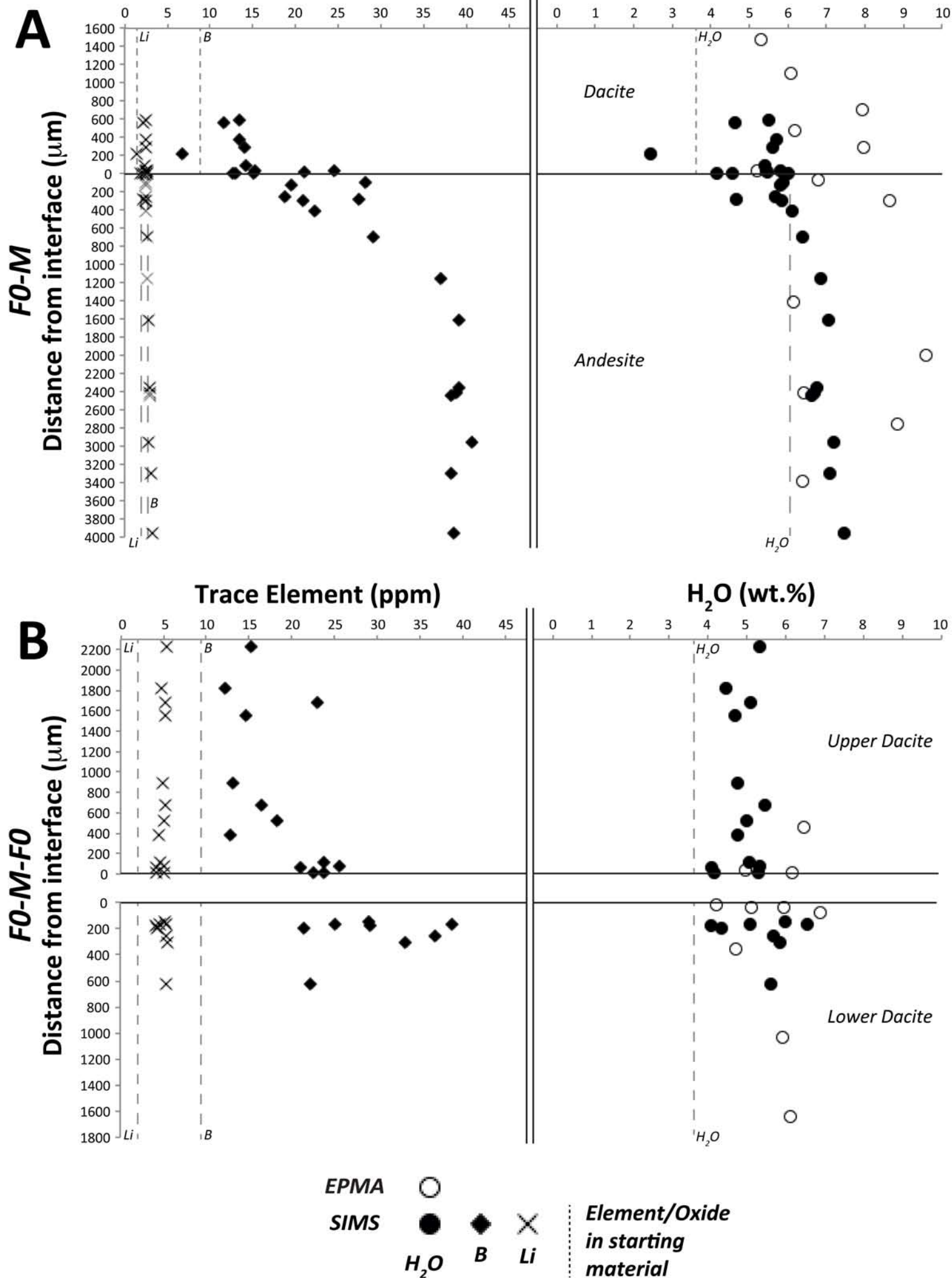
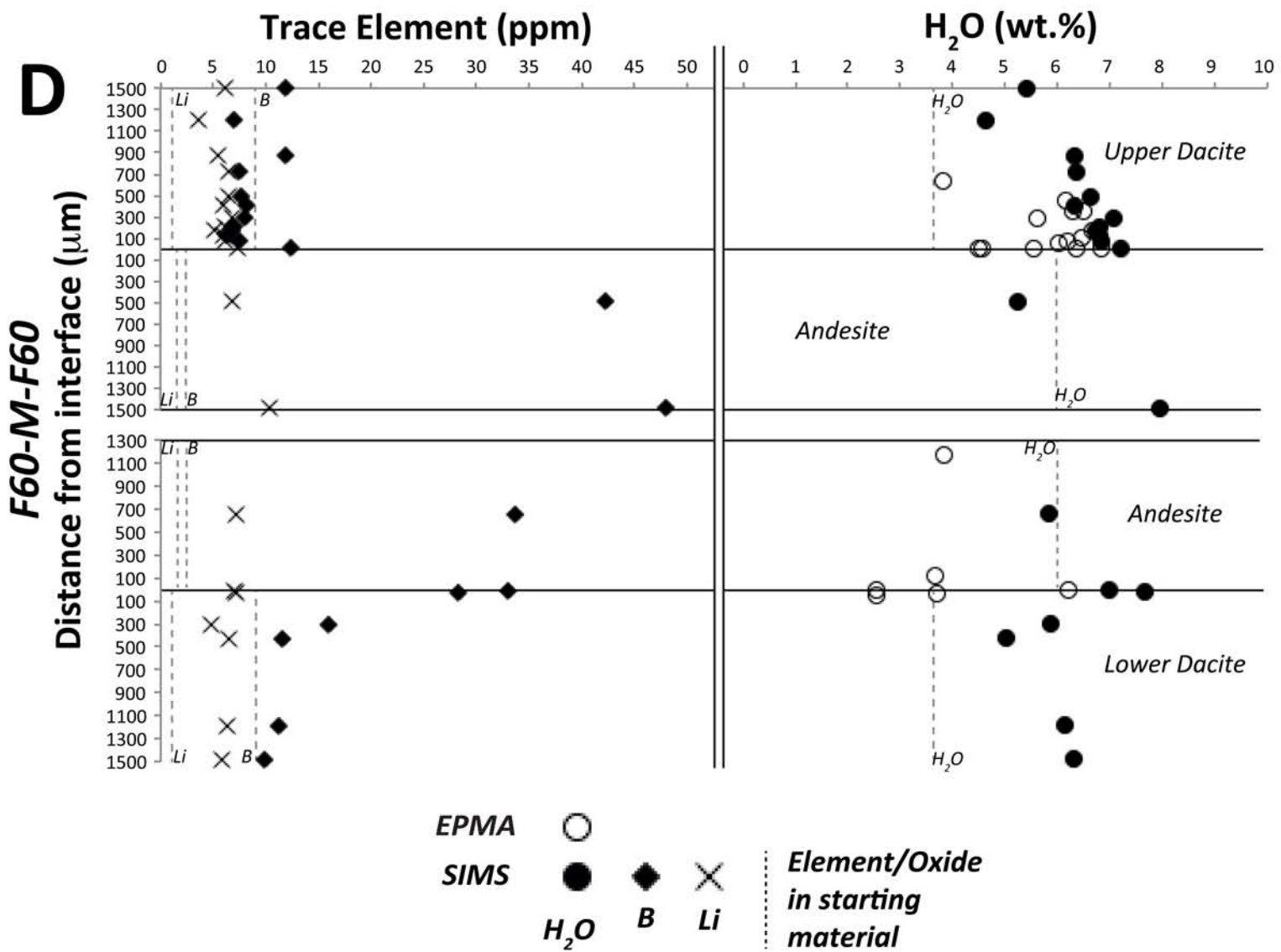
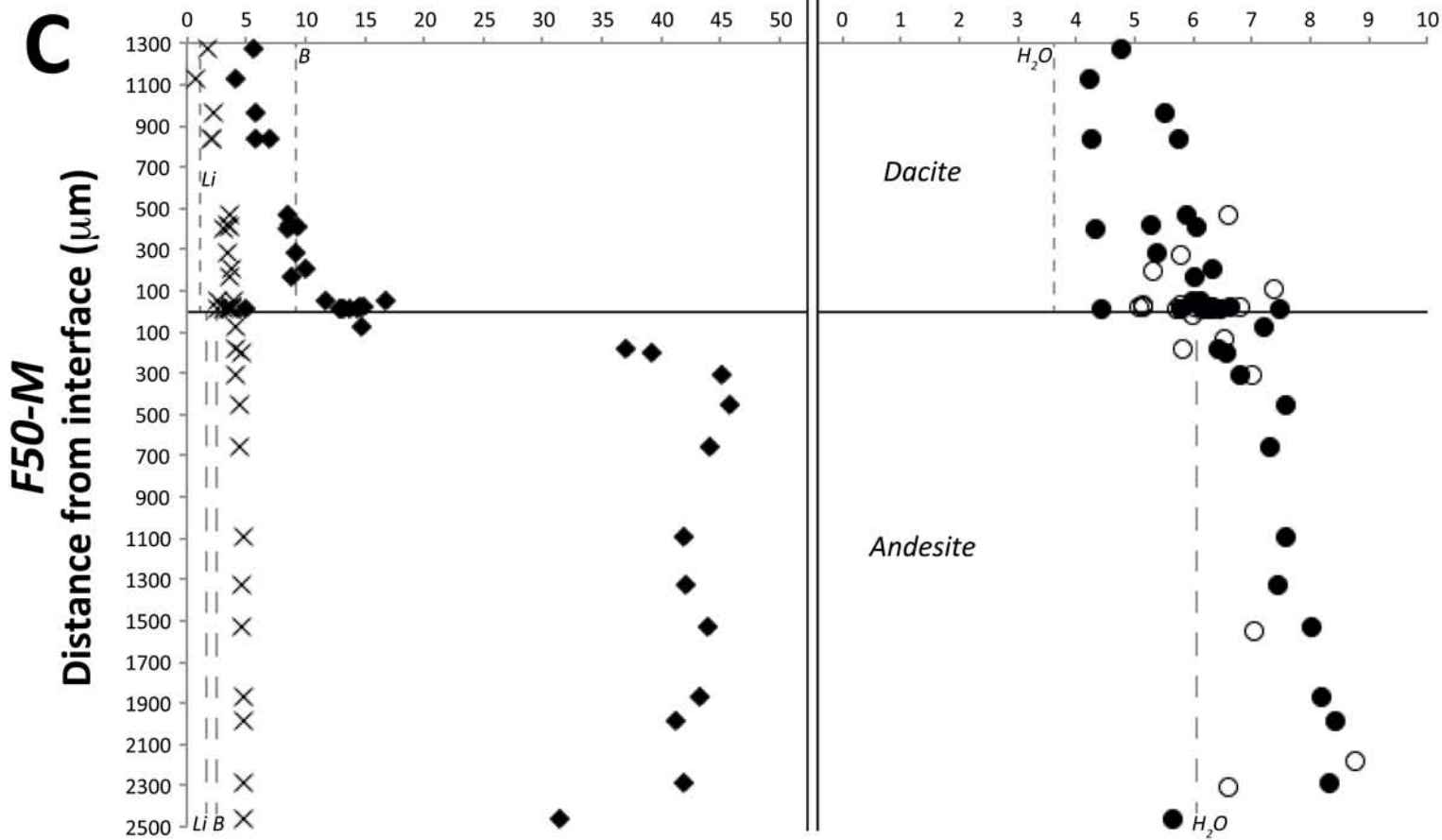
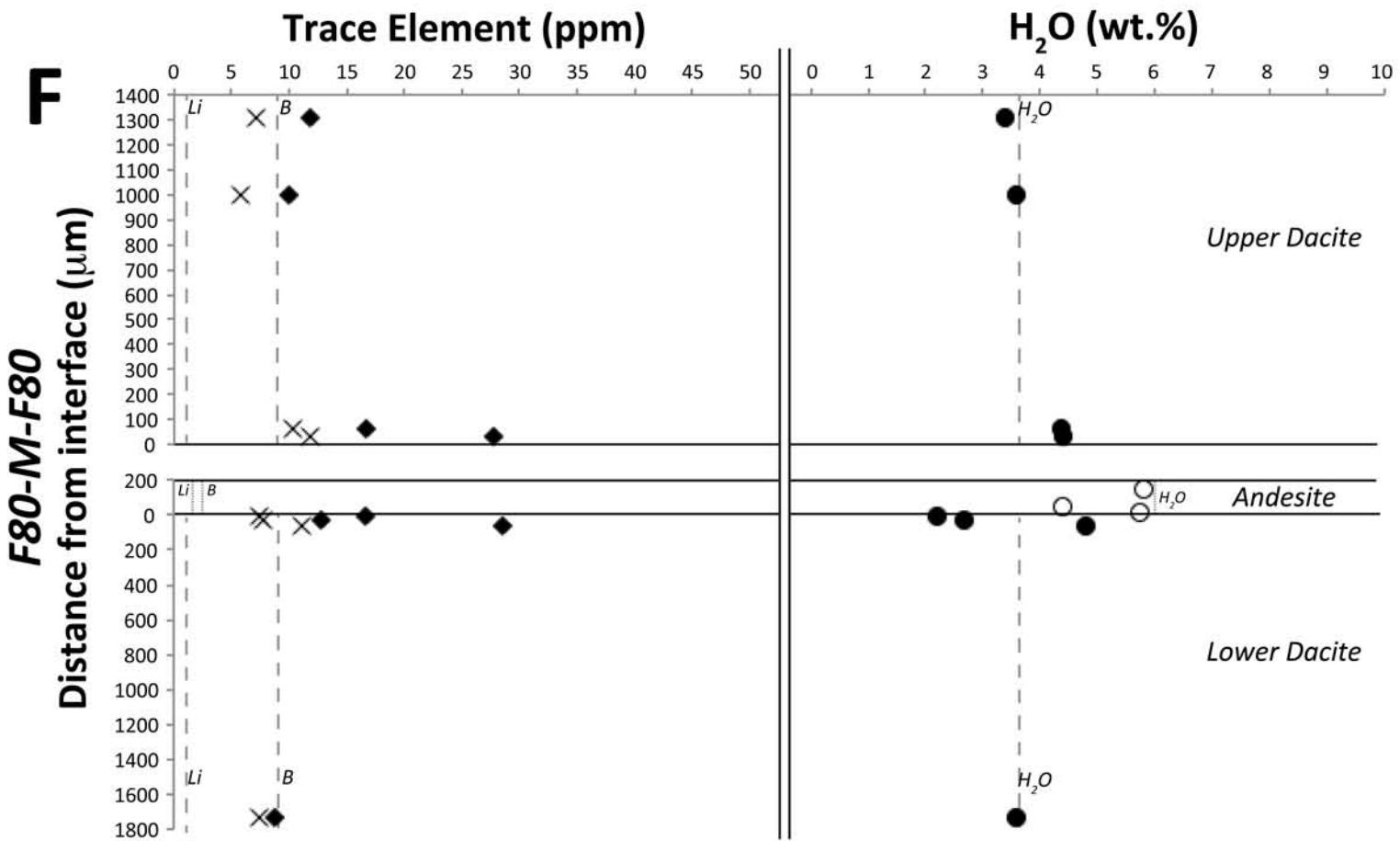
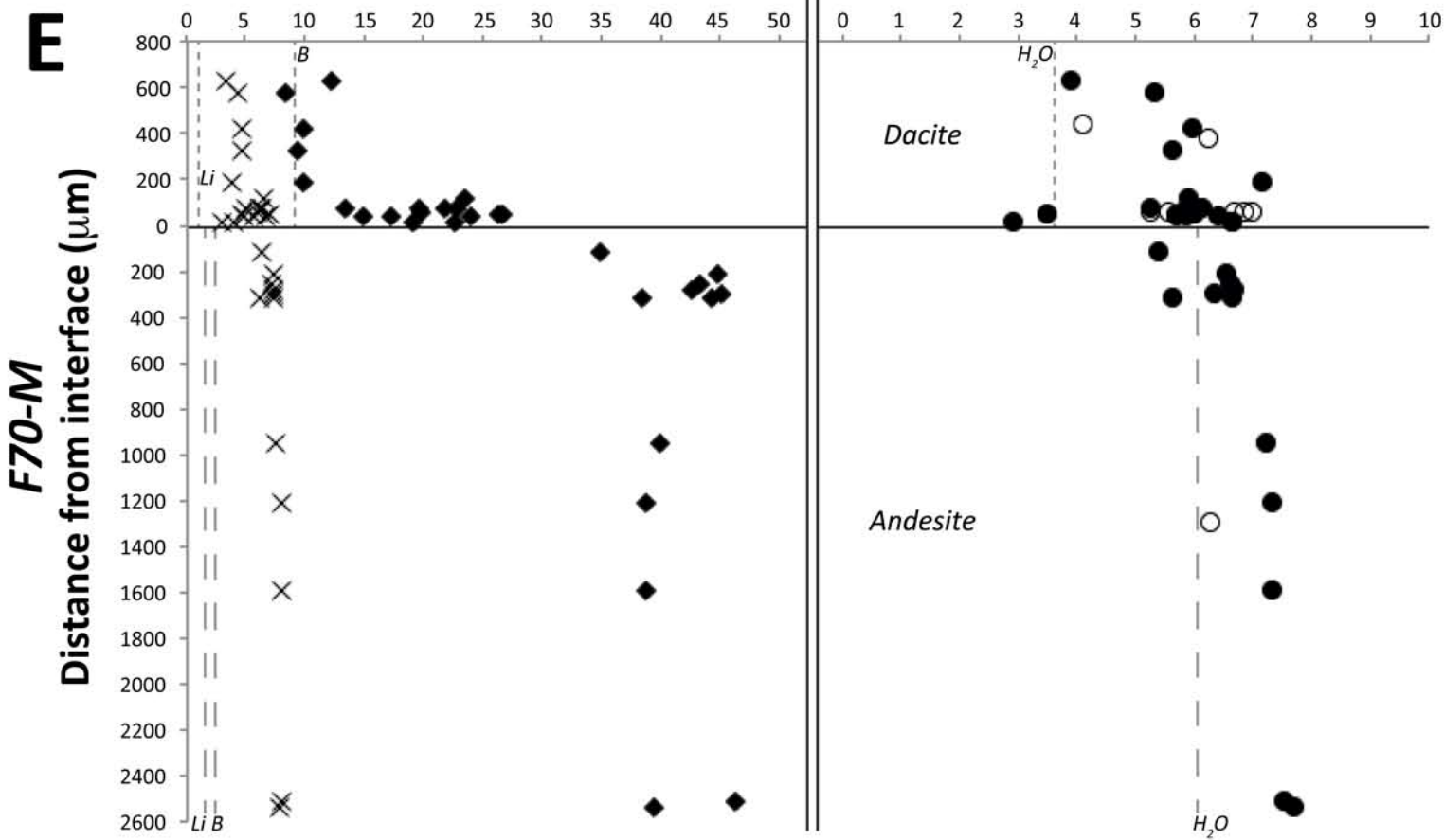


Figure SM 4 cont'





EPMA ○

SIMS ● ◆ ×

$\text{H}_2\text{O}$   $\text{B}$   $\text{Li}$

..... Element/Oxide in starting material



